

# **Kinematic Relationship between Multiphase Gas, Excitation, and Star-Forming Sites in Cool-Core Nebulae**

A THESIS

SUBMITTED TO THE DEPARTMENT OF PHYSICS

OF THE UNIVERSITY OF HONG KONG

IN PARTIAL FULFILMENT OF THE REQUIREMENTS

FOR THE DEGREE OF

MASTER OF PHILOSOPHY

By

JAMES M.G. NIANIAS

January 2022

(Temporary Binding for Examination Purposes)



**Abstract of thesis entitled**

**Kinematic Relationship between Multiphase  
Gas, Excitation, and Star-Forming Sites in  
Cool-Core Nebulae**

submitted by  
**JAMES M.G. NIANIAS**  
for the Degree of Master of Philosophy  
at The University of Hong Kong  
in January 2022

The giant elliptical galaxies at the centers of galaxy groups and clusters sometimes host luminous emission-line nebulae comprising ionized, atomic, and molecular gas. When well resolved, these nebulae exhibit filamentary structures that are immersed in the surrounding hot X-ray-emitting intracluster gas. Appearing when the entropy of the intracluster medium at the cores of groups or clusters is relatively low, these nebulae are linked to cooling of their surrounding hot gas. Despite decades of study, however, the nature of such cool-core nebulae remains poorly understood; even their basic physical properties such as density and temperature, along with the physical conditions that lead to their occasional star formation.



Identifying the mechanism(s) that energizes cool-core nebulae lies at the heart of a better understanding of these nebulae. To this end, I study the kinematic relationship between the atomic (perhaps partially ionized) and molecular phases of the cool-core nebula in NGC5044, the giant elliptical galaxy at the center of the NGC5044 group. This galaxy exhibits only a weak AGN and no recent star formation, leaving conduction of heat or penetration of energetic particles from the surrounding intracluster gas as the most likely mechanisms for energizing its nebula. I find that the gas components emitting in H $\alpha$ , H<sub>2</sub> 1-0 S(1) at 2.12 $\mu$ m, and CO share essentially identical kinematics. If confined to spatially distinct volumes, the different gas components should quickly decouple upon infall owing to ram pressure with the intracluster medium. Instead, the different gas components likely co-exist within the same volume, not possible if energized purely through thermal collisions but possible if powered by energetic particles.

I find the ratios in H $\alpha$ , H<sub>2</sub>, and CO lines to be quite uniform throughout NGC5044, with an H<sub>2</sub> to H $\alpha$  ratio remarkably similar to that in NGC1275, the giant elliptical galaxy at the center of the Perseus cluster. In addition, I measure the [OI] and [OIII] line intensity throughout NGC5044, and demonstrate that the line ratios rule out thermally-energized gas but provide further support for gas powered by energetic particles. These results, together with the need for the different gas components in NGC5044 to be kinematically coupled, promise stronger constraints on theoretical models based on energetic particles for powering cool-core nebulae once predictions for the emission-line spectrum of NGC5044, like that published for NGC1275, become available.

Finally, I present an [OIII] image of the nebula in NGC1275. I confirm the discovery of a second giant HII region in its inner nebula, and demonstrate



the ability to detect giant HII regions at the outskirts of the nebula where the vast majority of star clusters in NGC1275 have recently formed. I also show that some of the young star clusters host bright HII regions, in contradiction with the expectation that their natal gas should be quickly dispersed during the formation of very massive star clusters. Finally, I demonstrate that, like NGC5044, the entire nebula of NGC1275 likely glows weakly in [OIII], further emphasizing the need for energetic particles to explain its peculiar line ratios.

(Number of words: 502)

---

Author: JAMES M.G. NIANIAS

January 2022

---

Supervisor: Dr. J. J. L. Lim

January 2022



**Kinematic Relationship between Multiphase  
Gas, Excitation, and Star-Forming Sites in  
Cool-Core Nebulae**

by

JAMES M.G. NIANIAS

B.Sc., *H.K.U.*

A thesis submitted in partial fulfilment of the requirements for  
the Degree of Master of Philosophy  
at The University of Hong Kong.

January 2022



# Acknowledgements

First and foremost I thank Dr Jeremy Lim for his unwavering attentiveness as a supervisor, teacher, and mentor; there are exceedingly few supervisors who put such time and effort into supporting their students, both personally and academically. I also want to thank my unofficial secondary supervisor, Dr Youichi Ohyama, for his patience in teaching me so many technical concepts over the years I have worked with him, and willingness to answer my questions (whether good or not) at any time of day. I also thank my fellow current/former astrophysics postgraduates Amruth Alfred, Juno Li, Jacky Chan, and Michael Yeung for consulting on conceptual and technical issues countless times throughout the past two years (and prior). I thank Emily Wong for providing me with the catalog of young star clusters in NGC 1275 as well as an H $\alpha$  image of the nebula, and Arsen Levitskiy for providing spectra from NGC 1275 as well as SSP models used Chapter 2. Finally, I thank my mother, my father, and my girlfriend Natasha for their unyielding support throughout the course of this MPhil as well as during my years as an undergraduate.

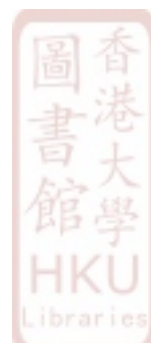


# Contents

<b>Acknowledgements</b>	i
<b>Table of Contents</b>	ii
<b>List of Figures</b>	iv
<b>List of Tables</b>	xii
<b>1 Introduction</b>	1
1.1 Origin of Cool Filaments . . . . .	3
1.2 Physical Properties . . . . .	4
1.3 Excitation . . . . .	5
1.4 Fate . . . . .	8
1.5 Objectives and Overview . . . . .	9
<b>2 Kinematical Relationship between Multiphase Gas in the Cool- Core Nebula of the NGC 5044 Group</b>	11
2.1 Paper I: Observations and Data Reduction . . . . .	12
2.1.1 Canada-France-Hawaii Telescope . . . . .	12
2.1.2 Spectroscopy . . . . .	21
2.2 Results . . . . .	26



2.2.1	Imaging of the 2.12 micron H <sub>2</sub> 1-0 S(1) line . . . . .	26
2.2.2	Full spectroscopy results . . . . .	28
2.3	Discussion . . . . .	34
2.3.1	Imaging . . . . .	34
2.3.2	Spectroscopy . . . . .	42
2.4	Full Text of Paper . . . . .	46
2.4.1	INTRODUCTION . . . . .	46
2.4.2	OBSERVATIONS AND ARCHIVAL DATA . . . . .	51
2.4.3	IMAGING RESULTS . . . . .	58
2.4.4	SPECTROSCOPY RESULTS . . . . .	61
2.4.5	INTERPRETATION AND DISCUSSION . . . . .	75
2.4.6	SUMMARY AND CONCLUSIONS . . . . .	85
<b>3</b>	<b>Excitation of the Cool-Core Nebula in NGC 5044</b>	<b>88</b>
3.1	Observations and Data Reduction . . . . .	92
3.2	Results . . . . .	96
3.3	Interpretation and Discussion . . . . .	104
<b>4</b>	<b>Sites of Star Formation in the Central Galaxy of the Perseus Cluster</b>	<b>108</b>
4.1	Observations and Data Reduction . . . . .	111
4.2	Results and Discussion . . . . .	117
<b>5</b>	<b>Summary and Conclusions</b>	<b>127</b>
	<b>Bibliography</b>	<b>131</b>



# List of Figures

1.1	H $\alpha$ +[NII] images of NGC 1275 (left) from Lim et al. (2020) and NGC 5044 (right) from David et al. (2011). . . . .	3
1.2	Optical spectrum from NGC 1275. The weak [OIII] $\lambda\lambda$ 4959/5007 and H $\beta$ lines, among others, differentiate this spectrum from galactic HII regions such as the Orion Nebula. . . . .	6
1.3	Fractional abundance of molecular (H <sub>2</sub> ), atomic (H <sup>0</sup> ), and ionized (H <sup>+</sup> ) hydrogen under pure heating (left) and cosmic ray excitation (right); the cosmic ray case allows all three states to coexist in the same gas volume under the right conditions. . . . .	8
2.1	WIRCam K <sub>s</sub> and H <sub>2</sub> filter bandpasses with redshifted H <sub>2</sub> line from NGC 5044 shown. . . . .	13
2.2	Representation of WIRCam nodding and dithering pattern (note that number and pattern of dithering positions in the figure is not the same as in the observations). . . . .	14
2.3	My original continuum-subtracted H <sub>2</sub> narrowband image, showing multiple problems owing to the automatic background subtraction performed at CFHT. The position of NGC 5044 is indicated by the red ellipse. . . . .	16



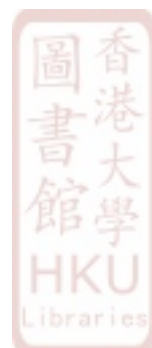
2.4	Procedure for generating a radially-dependent scale factor for subtraction of the stellar continuum from the narrowband image in the presence of a color gradient . . . . .	17
2.5	Sky construction procedure showing stills from DS9 at each stage	19
2.6	A representation of the plots of azimuthally-averaged narrowband/K <sub>s</sub> ratio vs radius that I used to fine-tune the DC offset and thus perform an accurate continuum subtraction. . . . .	20
2.7	H $\alpha$ + [NII], H <sub>2</sub> , and CO spectra. . . . .	29
2.8	H $\alpha$ + [NII], H <sub>2</sub> , and CO spectra. . . . .	30
2.9	H $\alpha$ + [NII], H <sub>2</sub> , and CO spectra. . . . .	31
2.10	H $\alpha$ + [NII], H <sub>2</sub> , and CO spectra. . . . .	32
2.11	H $\alpha$ + [NII], H <sub>2</sub> , and CO spectra. . . . .	33
2.12	WIRCam K <sub>s</sub> and H <sub>2</sub> filter bandpasses with redshifted H <sub>2</sub> line from NGC 5044 shown. Also shown in green is the wavelength range of the ISAAC NIR spectroscopy. . . . .	35
2.13	HST dust map contours overlaid on a zoom-up of the central region of the continuum-subtracted H <sub>2</sub> image of NGC 5044 (smoothed for clarity). . . . .	36
2.14	Spitzer 3.6 $\mu$ m/4.5 $\mu$ m ratio image showing increase towards the central region of NGC 5044 due to CO absorption. . . . .	37
2.15	Spitzer 3.6/4.5 ratio vs radius along vertical and horizontal cuts through NGC 5044. . . . .	38
2.16	Estimates of the H <sub>2</sub> /K <sub>s</sub> ratio along the ISAAC slit based on the linear baselines fitted to the continua in the NIR spectra. . . .	40



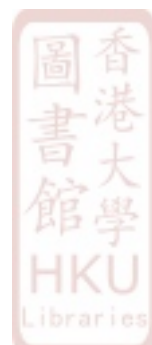
2.17 Estimates of the H <sub>2</sub> /Ks ratio along the ISAAC slit based on the linear baselines fitted to the continua in the NIR spectra (inner 20''). . . . . .	41
2.18 Effective ISAAC slit position after sky subtraction. . . . .	53
2.19 Typical calibrated NIR spectrum showing H <sub>2</sub> line, absorption feature adjacent to H <sub>2</sub> , and traces or residual OH lines. The red dashed line shows wavelengths masked when fitting the H <sub>2</sub> line and/or continuum. . . . .	55
2.20 Optical spectrum extracted from MUSE data cube showing (photospheric) absorption and (nebular) emission in H $\alpha$ , taken from a slit position 12'' south-east of the nucleus. . . . .	57
2.21 Continuum-subtracted H <sub>2</sub> narrowband image using our custom sky-subtraction strategy. Units are erg s <sup>-1</sup> cm <sup>-2</sup> arcsec <sup>-1</sup> . . . . .	59
2.22 Extracted H $\alpha$ , H <sub>2</sub> , and CO spectra arranged according to position along the slit. . . . .	62
2.23 Central velocities (top panel) and velocity dispersions (bottom panel) of the line profiles fitted to the H $\alpha$ , H <sub>2</sub> , and CO spectra plotted against position along the slit. The triangular markers in the bottom panel indicate the fitted lines where the velocity dispersion was below that of the observations. In these cases, the values have not been corrected for instrumental dispersion. We attribute this issue to fluctuations in the spectral baselines distorting the lines. . . . .	64
2.24 Histogram of central velocity differences between matched CO and H $\alpha$ lines . . . . .	65



2.25 H $\alpha$ and H $_2$ emission from the NW knot at the far end of the slit. The aperture size for these spectra was increased from 0.8'' to 3.0'' to increase signal-to-noise. . . . .	72
2.26 Line ratios vs slit position. Triangular grey markers indicate where the S/N of H $_2$ or CO falls below S/N = 3 and are upper bounds only based on the 3 sigma RMS noise level in the data. . . . .	73
2.27 Trajectories of gas clouds of varying temperature/density falling through the ICM towards the cluster core from initial height of 5 kpc. . . . .	79
2.28 Trajectories of gas clouds of varying temperature/density falling through the ICM towards the cluster core from initial height of 1 kpc. . . . .	80
3.1 Plot from Ferland et al. (2009) illustrating how [OI] and [OIII] emissivity can be used to constrain excitation and gas properties. . . . .	90
3.2 Typical spectrum from the bright central part of the nebula in NGC 5044, with selected nebular emission lines indicated. . . . .	91
3.3 Top: H $\alpha$ surface brightness map used to determine on- vs off- nebula spaxels. Pixels with H $\alpha$ emission below 3 sigma are blank. Bottom: H $\alpha$ +[NII] lines with fitted model before baseline sub- traction. . . . .	94
3.4 Spectral baselines for the H $\alpha$ +[NII] (top), [OI] (middle), and [OIII] (bottom) lines. Some (limited) [NII] emission can be seen in the top panel which will have to be corrected in refinements to the data reduction procedure. . . . .	95



3.5	Example spaxels from each of the three slices: H $\alpha$ (top), [OI] (middle), and [OIII] (bottom) showing the emission lines before (left column) and after (right column) baseline subtraction. . . . .	97
3.6	Left: Example of a spaxel from the bright inner region of the nebula where line profiles are frequently double-peaked, with fitted double-Gaussian profile shown. Right: Example of a spaxel where a single-Gaussian profile has been fitted. . . . . . . . .	98
3.7	Maps of H $\alpha$ , [OI], and [OIII] flux density based on the results of fitting single- or double-peaked line profiles. In cases where double peaks were fitted, the left column shows the lower-velocity component. Spaxels where emission is below 3 sigma are left blank.	100
3.8	Maps of H $\alpha$ central velocity and velocity dispersion (FWHM) for single- or double-peaked line profiles. In cases where double peaks were fitted, the left column shows the lower-velocity component.	101
3.9	From top to bottom: [OI]/H $\alpha$ , [OIII]/H $\alpha$ , and [OI]/[OIII] line ratio maps for single-Gaussian fitted line profiles. . . . .	103
3.10	The left shows an example spaxel covering the H $\alpha$ , [OI], and [OIII] lines from the regions of the nebula where the [OIII]/H $\alpha$ ratio is relatively low and [OI]/[OIII] is relatively high; the right shows an example from where the [OIII]/H $\alpha$ ratio is relatively high and [OI]/[OIII] is relatively low. . . . . . . . .	105
3.11	Plot from Ferland et al. (2009) illustrating how [OI] and [OIII] emissivity can be used to constrain excitation and gas properties.	106
4.1	Map of the young star clusters cataloged by Lim et al. (2020) overlaid on a H $\alpha$ +[NII] image of NGC 1275. The green contour highlights the extent of the HVS. . . . . . . . .	110



4.2	MegaPrime [OIII]-on and [OIII]-off filters showing the wavelengths of the redshifted [OIII] $\lambda$ 5007 and $\lambda$ 4959 lines from NGC 1275. . .	112
4.3	HST/ACS F550M filter bandpass in pink overlaid on an example spectrum from NGC 1275. The filter bandpass in red is the F625W R band filter used to image the H $\alpha$ +[NII]+[SII]+[OI] lines.113	
4.4	Left: HST/ACS F550M continuum image. Right: the same image with exaggerated scaling revealing the background structure which became imprinted onto the continuum-subtracted [OIII] image. . . . .	115
4.5	Entire field imaged by MegaPrime in the [OIII]-off filter showing many members of the Perseus cluster, with zoom-in on NGC 1275 at the core of the Perseus cluster showing gaseous filaments and/or young star clusters (log scaling). . . . .	118
4.6	HST H $\alpha$ + image (upper left), CFHT [OIII] image (upper right), overlay of young clusters from Lim et al. (2020) (lower left), and cutout regions used to mitigate the uneven background (lower right). . . . .	119
4.7	Cutout of the central region of NGC 1275 in H $\alpha$ + (upper left) and [OIII] (upper right). Shown below is the H <sub>2</sub> /H $\alpha$ ratio from Lim et al. (2012), indicating the HII region first described in Shields & Filippenko (1990) as well as another candidate HII region to the west of the AGN. The regions are labeled HIIa and HIIb on the [OIII] map. . . . .	121



4.8 Cutout of the south-eastern region of NGC 1275 in H $\alpha$ + (upper left) and [OIII] (upper right). Shown below are overlays of the young star clusters cataloged by Lim et al. (2020), with only the youngest clusters (of ages $\lesssim 100$ Myr) being shown in the lower right panel. . . . .	122
4.9 Cutout of the northern region of NGC 1275 in H $\alpha$ + (upper left) and [OIII] (upper right). Shown below is an overlay of the young star clusters cataloged by Lim et al. (2020). . . . .	124
4.10 Cutout of the south-western region of NGC 1275 in H $\alpha$ + (upper left) and [OIII] (upper right). Shown in the lower left is an overlay of the young star clusters cataloged by Lim et al. (2020) and in the lower right is the [OIII]/H $\alpha$ + ratio, showing the circular aperture from which the [OIII]/H $\alpha$ + ratio was extracted. . . . .	125



# List of Tables

2.1	De-projected temperature profiles for the X-ray ICM in NGC 5044 (David et al. 2017) and NGC 1275 (Churazov et al. 2003)	45
2.2	De-projected density profiles for the X-ray ICM in NGC 5044 (David et al. 2017) and NGC 1275 (Churazov et al. 2003)	45
2.3	Parameters for iteration 1	78
2.4	Parameters for iteration 2	78
2.5	Typical ICM parameters for NGC 5044 and NGC 1275	84



# Chapter 1

## Introduction



empty

The intracluster medium (ICM) of galaxy clusters and groups comprises hot gas emitting thermal bremsstrahlung X-ray radiation. In some clusters and groups (henceforth referred to as clusters unless otherwise stated), the surface brightness (and hence density) of the X-ray emission is sharply peaked towards the cluster center. The increased density in the cluster core is accompanied by a systematic drop in temperature of the X-ray gas and hence a low central entropy. Such cool-core clusters are often found to harbor large quantities of cool, multi-phase gas that exhibit strong atomic and molecular line emission, always hosted by the giant elliptical galaxy at the center of the cluster. This galaxy is usually the brightest in the cluster, and hence is referred to as the brightest cluster galaxy (BCG). Imaging of spectral lines such as H $\alpha$  (e.g. Conselice et al. 2001), H<sub>2</sub> 1-0  $S(1)$  (e.g. Lim et al. 2012), and CO (1–0) (e.g. Olivares et al. 2019) reveal that the cool, multi-phase gas is spread out in filaments extending tens of kpc from the center of the BCG and immersed in the hot X-ray ICM. Figure 1.1 shows NGC 1275, the central elliptical galaxy of the Perseus cluster (the X-ray brightest cluster in the sky), which is the most famous and well-studied example of a filamentary emission nebula in a cool-core cluster. Another example which has also received considerable attention is NGC 5044, the central elliptical galaxy of the NGC 5044 group (the X-ray brightest group in the sky), shown also in Figure 1.1. The origin, physical properties, excitation, and fate of these nebular filaments remain, for the most part, poorly understood. I now give a brief review of these issues.



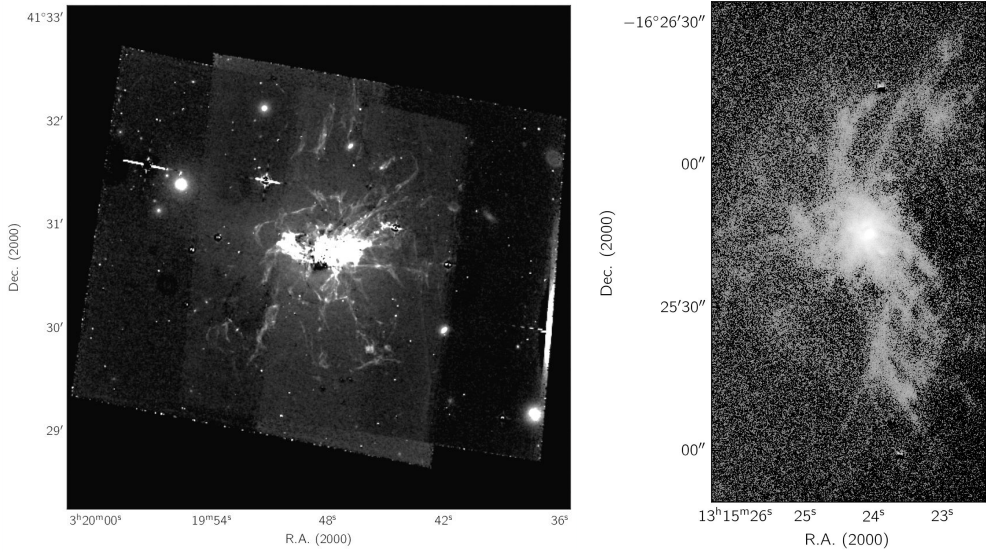


Figure 1.1 H $\alpha$ +[NII] images of NGC 1275 (left) from Lim et al. (2020) and NGC 5044 (right) from David et al. (2011).

## 1.1 Origin of Cool Filaments

Circumstantial evidence had led to the widespread contention cool-core nebulae are produced from cooling of the surrounding ICM. The intense radiative losses in the form of X-ray emission in the cluster cores was initially thought to lead to a “cooling flow” of hot X-ray gas into the cluster center. Such cooling flows provides a natural explanation for the origins of the cool gas filaments; however, subsequent work by Molendi & Pizzolato (2001) showed that the mass deposition rates were much lower than had been anticipated. It is now understood that reheating of the ICM by active galactic nuclei (AGNs) is responsible for the lack of cooling flows in cool-core clusters (Fabian 2012). Nevertheless, there is a close link between the thermal state of the ICM and the presence of cool gas filaments: nebulae such as those seen in NGC 1275 and NGC 5044 are almost exclusively found in clusters where the entropy of the ICM falls below a threshold of  $\sim 30\text{keV cm}^2$  within the central  $\sim 200\text{kpc}$  (Cavagnolo et al.

2008). This dependence constitutes indirect evidence for the existence of residual cooling flows, though with a mass-deposition rate that has not yet been measured.

## 1.2 Physical Properties

The physical characteristics of the gas constituting cool-core nebulae (temperature, density, and mass) are poorly constrained. This is chiefly because the excitation mechanism powering the line emission from the filaments has not yet been firmly identified, making it difficult to infer anything about physical properties from the observed emission line spectra. Observations of CO emission have been used to estimate the mass of the molecular phase of the filaments (i.e. H<sub>2</sub>) at up to  $\sim 10^{11} M_{\odot}$  (Edge 2001; Salomé & Combes 2003). If correct, these estimates mean that cool-core nebulae are likely dominated by molecular gas traced by CO. These estimates, however, rely on an empirical conversion between CO luminosity and H<sub>2</sub> mass derived from observations of molecular clouds in our own Galaxy. Lim et al. (2017) argue that this relation is unlikely to hold under the vastly different physical conditions in cool-core nebular clouds compared to Galactic molecular clouds. In our Galaxy, H $\alpha$  is most commonly produced by almost completed ionized gas that is photoionized or shocked. It is not clear whether H $\alpha$  from cool-core nebulae originates from predominantly neutral or ionized gas due to uncertainty about the excitation mechanism, as explained next.

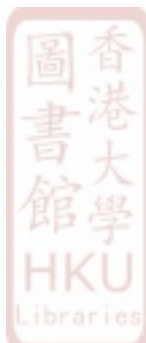


### 1.3 Excitation

Cool-core nebulae generally exhibit low-ionization lines as well as a mix of high-ionization lines unlike anything we see in our own galaxy. For instance, NGC 1275 has filaments with little or no detectable [OIII] emission, but are relatively bright in lines with higher ionization potential such as [NeIII]. NGC 5044 shows dim [OIII] along with faint (but just detectable) HeI as discussed in 3.2. In collisionally ionized and excited gas, HeI lines require significantly higher temperatures to be excited than [OIII], so the detection of HeI should be accompanied by bright [OIII] lines.

Figure 1.2 shows a typical optical spectrum from the cool-core nebula in NGC 1275. This spectrum was extracted by another student in our group for his MPhil thesis (see Acknowledgments). The observed emission line spectrum stands in stark contrast with those of photodissociation regions (PDRs) or HII regions, in which  $[\text{OIII}]\lambda 4959/5007$  and  $\text{H}\beta$  are typically comparable in luminosity to  $\text{H}\alpha$ . This argues against photoexcitation of the filaments by young stars. As I will show (chapter 3), the nebula in NGC 5044 exhibits a qualitatively similar spectrum. Moreover, NGC 5044 does not exhibit any recent star formation, firmly ruling out photoionization or other stellar processes (e.g., supernova shocks) for exciting its nebula.

A pervasive source that could power cool-core nebulae is the X-rays from the surrounding ICM. This source can be ruled out in the case of NGC 1275 on purely energetic grounds: the surface brightness of the X-ray emitting ICM is lower than that of the total combined line emission from the cool filaments by a factor of up to two orders of magnitude (Lim et al. 2012). Photoionization by the AGN has long been ruled out owing to the relatively uniform surface brightness of the filaments, by contrast with the radial gradient expected for a



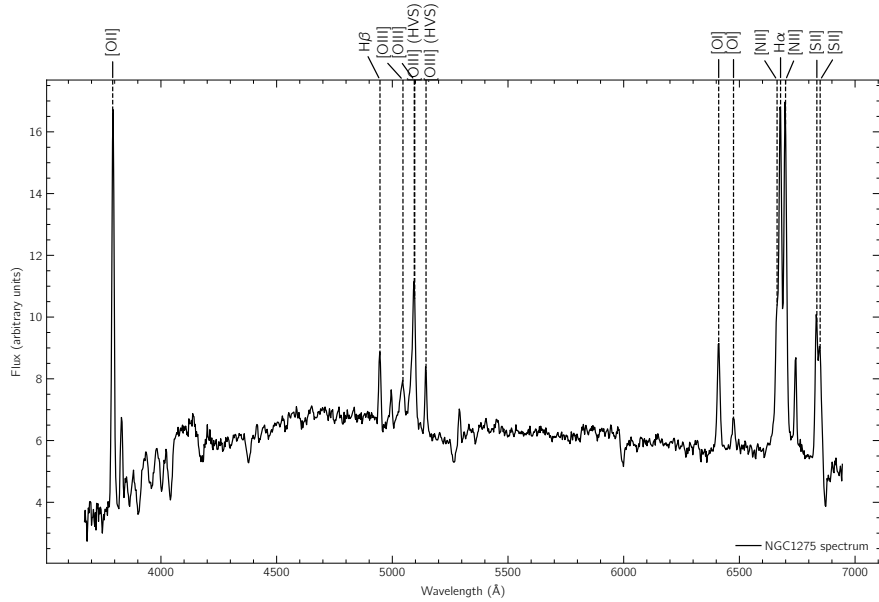


Figure 1.2 Optical spectrum from NGC 1275. The weak  $[OIII]\lambda 4959/5007$  and  $H\beta$  lines, among others, differentiate this spectrum from galactic HII regions such as the Orion Nebula.

central power source. Photoexcitation by the AGN can also be ruled out by the lack of any strong radial gradients in the ratios between high and low-ionization emission lines, suggesting in-situ excitation (Lim et al. 2012).

Yet another possible power source is simple heating of the nebular gas. This thermal energy could be provided by conduction from the surrounding hot X-ray gas or Alfvén waves propagating along the magnetic fields thought to thread the nebular filaments, to name but two examples. Ferland et al. (2009) have examined whether a source that purely heats the gas can give rise to the combination of emission lines seen in cool-core nebulae. Their models suggest that pure heating (as a dominant excitation mechanism) is not consistent with the relative strength of emission lines seen in cool-core nebulae.

As an alternative to pure heating, Ferland et al. (2008); Ferland et al. (2009) argue for excitation by energetic particles penetrating into the filaments. In this

picture, high-energy particles penetrate into the gas in the filaments, partially ionizing it and giving rise to a secondary population of electrons which in turn go on to excite the rest of the gas. Modeling using CLOUDY (Ferland et al. 2017) shows that penetrating energetic particles are able to produce a similar spectrum to what we see in the filaments of NGC 1275. In Figure 1.3, Ferland et al. (2009) compare the fractional abundance of molecular, atomic, and ionized hydrogen under energetic particle excitation to that under pure heating. As can be seen from this plot, atomic and molecular hydrogen can exist in comparable quantities under the a fairly broad range of energetic particle flux density (they refer to the energetic particles as “cosmic rays” in the figure), unlike in the case of pure heating where only one phase can exist at a given temperature. This can explain why the same parcel of gas can emit both bright H<sub>2</sub> and H $\alpha$  lines: in this situation, H $\alpha$  can arise from gas that is partially if not predominantly neutral. One of the objectives of my thesis is to test whether molecular and atomic emission lines indeed originate from common volumes of gas in the cool-core nebula in NGC 5044 by examining their kinematics (chapter 2). Another objective is to measure line ratios in NGC 5044 so as to provide a more stringent test (chapter 3). NGC 5044 is a particularly useful cool-core nebula to study, since it exhibits no star formation, and thus provides a clean case free from excitation associated with star formation (i.e. photoexcitation/ionization, shocks).

Fabian et al. (2011) propose that the energetic particles penetrating into the filaments may be electrons from the surrounding X-ray ICM, noting that the total outward flux in line emission from the filaments of NGC 1275 is close to the estimated energy flux of electrons impacting into them from the surrounding hot gas.



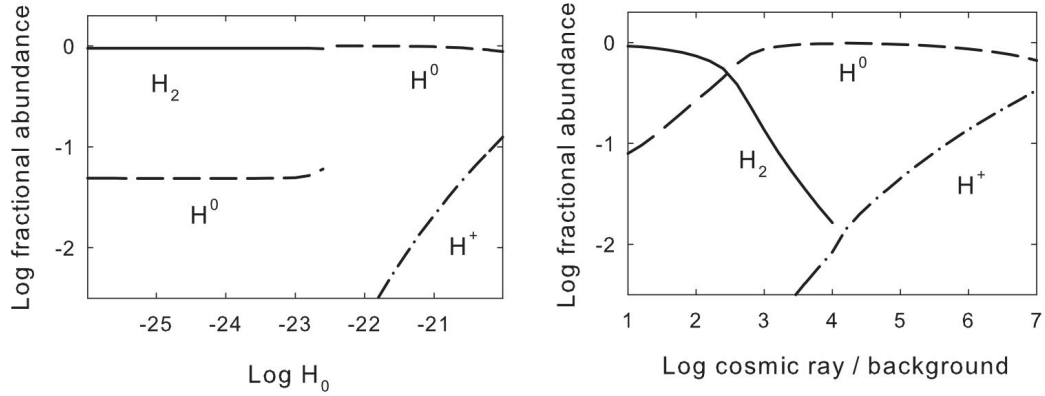


Figure 1.3 Fractional abundance of molecular ( $H_2$ ), atomic ( $H^0$ ), and ionized ( $H^+$ ) hydrogen under pure heating (left) and cosmic ray excitation (right); the cosmic ray case allows all three states to coexist in the same gas volume under the right conditions.

## 1.4 Fate

There are two possible fates for the cool gas filaments: (i) star formation, (ii) fueling the AGN (a third possibility is simply cyclical cooling and reheating). In at least one case, NGC 1275, star formation is taking place that appears to be linked to the cool gas filaments. Maps of the young stellar population such as those produced by Canning et al. (2010) and Lim et al. (2020) show that the young stars are also arrayed along filaments, some of which overlap with H $\alpha$  filaments in projection, while the majority are offset from nearby H $\alpha$  filaments. This morphological resemblance suggests that the stars are forming directly from the gas in the filaments. Yet very few sites of active star formation have been identified in this nebula. One of the objectives of my thesis is to identify giant HII regions such as the one discovered by Shields & Filippenko (1990),

with the aim of determining the conditions under which star formation occurs in the nebula (chapter 4).

## 1.5 Objectives and Overview

In chapters 2 and 3 of this thesis, I look at the example of NGC 5044 to test predictions of leading theoretical models of excitation of the gas in the filaments. I consider two excitation mechanisms: penetration of energetic particles into the nebula versus pure heating (as described above). In Chapter 2, I compare the kinematics of the molecular and atomic/ionized phases of the filaments in NGC 5044 using optical, near-IR, and radio spectroscopy of the H $\alpha$ , 2.12 $\mu$ m H $_2$ , and 1.3mm CO lines, respectively. As I demonstrate, if the energetic particle excitation model advocated in Ferland et al. (2009) is correct, then all these gas phases should share the same kinematics. I also extract H $_2$ /H $\alpha$ , CO/H $\alpha$ , and CO/H $_2$  line ratios. This part of the thesis has already been written up as a draft paper, with the manuscript included in Section 2.4. To give the reader more context about the observations and data reduction, results, and discussion of the paper, I give further details in Sections 2.1, 2.2, and 2.3, respectively.

In chapter 3, I present maps of the [OIII] $\lambda$ 5007, [OI] $\lambda$ 6300, and H $\alpha$  lines from the filaments in NGC 5044 using archival integral field unit (IFU) observations. I show that these results favor excitation by energetic particles over pure heating of the gas in the filaments. This chapter, along with chapter 2, constitute the first time that this excitation model has been tested outside of a single isolated region in NGC 1275.

In chapter 4, I address which part of the nebula in NGC 1275 is involved in star formation. This constitutes the first step towards follow up observations in



lines such as CO to study the physical conditions under which the nebula forms stars. To this end, I present imaging of the [OIII] $\lambda 5007$  line from NGC 1275, with the goal of identifying HII regions in the filaments. An additonal goal is to identify young star clusters emitting in [OIII], thus helping to establish how long the clusters are able to hold on to the gas from which they form before it is ejected due to radiation pressure/shocks. My results, shown in Section 4.2, also reveal, for the first time, that many of the H $\alpha$  filaments in NGC 1275 are also emitting faint [OIII].



## **Chapter 2**

# **Kinematical Relationship between Multiphase Gas in the Cool-Core Nebula of the NGC 5044 Group**



empty

## 2.1 Paper I: Observations and Data Reduction

In this Section, I provide details about the observations and data reduction carried out in a paper which I present in Section 2.4. The salient points of the observations and data reduction are reported in the paper itself (in Section 2.4.2). However, here I provide additional details that are not included in the paper in order to give the reader a more complete picture of the complexities in the data reduction and an insight into the process by which I reached my final results. To make this chapter readable I repeat all the key details mentioned in the full text of Paper I.

### 2.1.1 Canada-France-Hawaii Telescope

Our group carried out imaging to map the spatial distribution of the  $2.12\text{ }\mu\text{m}$   $\text{H}_2$  1-0  $S(1)$  line emission from NGC 5044 on 2013 April 21, April 30, and May 1 with the Wide-Field Infrared Camera (WIRCam) on the 3.6 m Canada-France-Hawaii Telescope (CFHT). Two filters were used: the  $2.122/0.032\text{ }\mu\text{m}$  (central wavelength/bandwidth in  $\mu\text{m}$ )  $\text{H}_2$  1-0  $S(1)$  (hereafter, simply  $\text{H}_2$ ) filter for the line, and the  $2.146/0.325\text{ }\mu\text{m}$   $\text{Ks}$  filter for the continuum (note that these bandpasses overlap; see Figure 2.1 for transmission curves). The goal of this observation strategy is to subtract the continuum image from the line image, thus revealing the  $\text{H}_2$  line emission from the target galaxy. We targeted a sensitivity of  $\sim 2 \times 10^{-17}\text{ erg s}^{-1}\text{ cm}^{-2}\text{ asec}^{-2}$  at the  $\sim 3$  sigma level, corresponding



to 9 hours of exposure time for the  $H_2$  filter and just 3 hours for the continuum owing to the wider bandpass of the latter. Based on the known circum-nuclear  $H\alpha + [\text{NII}]$  surface brightness of  $\sim 1 \times 10^{-15} \text{ erg s}^{-1} \text{ cm}^{-2} \text{ asec}^{-2}$  (David et al. 2009), and assuming an  $H_2$ -to- $H\alpha+[\text{NII}]$  ratio of 0.05 (equal to that observed in NGC 1275 by Lim et al. (2012)), our proposal estimated the  $H_2$  surface brightness to be  $\sim 5 \times 10^{-17} \text{ erg s}^{-1} \text{ cm}^{-2} \text{ asec}^{-2}$ , and thus the targeted detection threshold would make it possible to detect the  $H_2$  line at a signal-to-noise of  $\sim 5$  per pixel. Due to poor weather, the final total integration times reached were 253 minutes (47% of requested time) and 70.7 minutes (39% of requested time) for the  $H_2$  and continuum filters respectively.

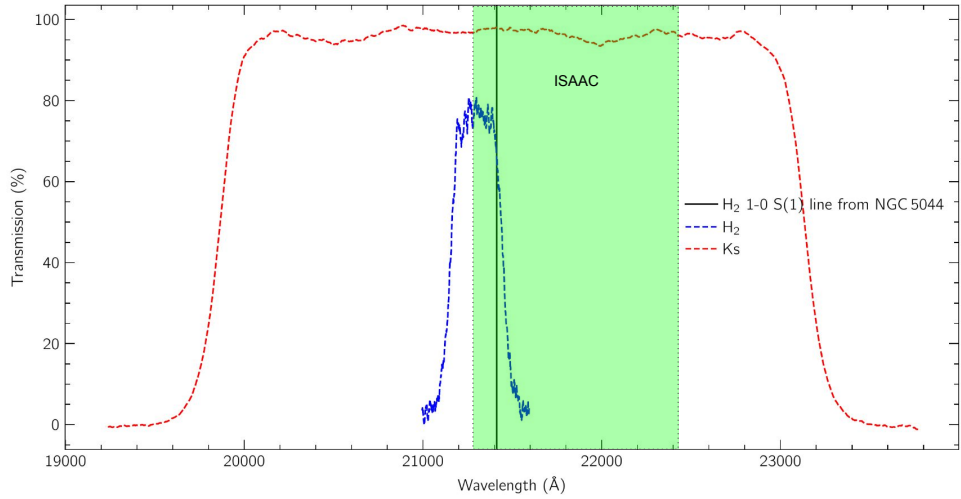


Figure 2.1 WIRCam Ks and  $H_2$  filter bandpasses with redshifted  $H_2$  line from NGC 5044 shown.

The observing strategy used a combination of nodding and dithering to optimize the construction of the sky (which is crucial in NIR imaging). WIRCam is composed of a  $2 \times 2$  array of four  $2048 \times 2048$  detectors. The nodding pattern switched the target between detectors 1 and 4 as shown in figure 2.2, and within



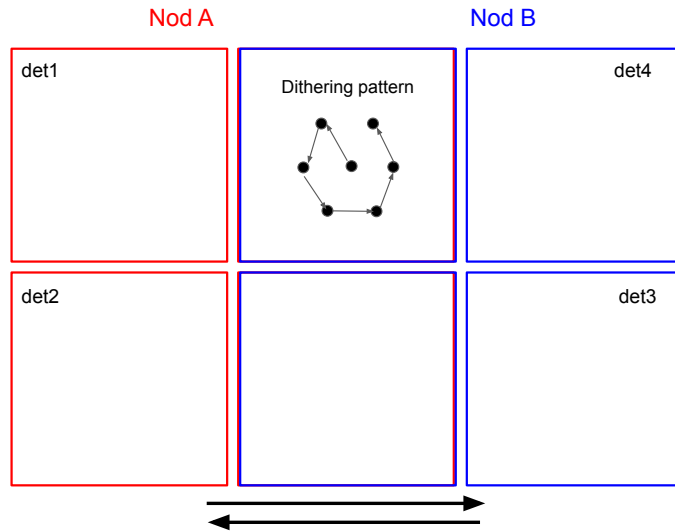


Figure 2.2 Representation of WIRCam nodding and dithering pattern (note that number and pattern of dithering positions in the figure is not the same as in the observations).

each nod a dithering pattern with a scale of  $1.0'$  was used (10 dithers per nod for the H<sub>2</sub> filter and 15 for the Ks filter).

The pre-processing of the WIRCam images was performed at CFHT using the ‘I‘iwi pipeline<sup>1</sup>. The ‘I‘iwi pipeline produces two sets of images for the observer: detrended-only frames (s-frames) in addition to frames that have been both detrended and sky subtracted (p-frames) according to a standard sky subtraction technique used for all WIRCam images. Detrending involves flagging saturated pixels, non-linearity correction, bias subtraction, dark current subtraction, flat fielding, and masking of bad pixels and the guide window<sup>2</sup>; sky subtraction involves constructing the sky for each frame by taking the median of a sequence of dithered images. As I explain below, the standard sky subtraction

<sup>1</sup><https://www.cfht.hawaii.edu/Instruments/Imaging/WIRCam/IiwiVersion2Doc.html>

<sup>2</sup>The guide window appears as a cross on each of the detectors in each frame; it appears due to the use of an image stabilizer unit (ISU) on each chip which continuously monitors a  $14 \times 14$  region centered on a bright star

method employed by CFHT later proved to be poorly suited for our purposes.

Initially, I stacked the p-frames in each filter following the Canadian Astronomy Data Center’s (CADC’s) WIRwolf<sup>3</sup> image stacking pipeline as an outline. The first step in this procedure involves source identification using SExtractor (Bertin & Arnouts 1996), which employs a neural network to detect and generate catalogs of stars and extended sources in each frame. These catalogs are then read by another program, SCAMP (Bertin 2006), which compares them with a reference catalog (in this case the 2MASS catalog (Skrutskie et al. 2006)) and derives a solution for focal plane distortion. Finally, a third program, SWARP (Bertin et al. 2002), applies the distortion solutions to the images, resamples each image to a common grid, and then performs co-addition of the frames yielding a final stacked image. This left me with two stacked images: one of the stellar continuum in Ks band and one of the H<sub>2</sub> line plus underlying continuum. I then used SWARP again to resample these stacked images onto a common grid so that the continuum could be subtracted from the narrowband image, followed by PSF matching using ASTROIMAGEJ to measure the sizes of the PSFs, and finally a manual sub-pixel alignment using ASTROPY (Astropy Collaboration et al. 2013, 2018). Finally, I subtracted the two images. Proper continuum subtraction requires fine-tuning of a scaling factor that must be applied to the continuum image in order to account for differing bandwidth and filter throughput. After careful adjustment of this parameter to minimize the residual stellar continuum, the results, shown in 2.3, showed no H<sub>2</sub> emission from the nebula, the distribution of which is expected to follow the H $\alpha$  emission as is true in the case of NGC 1275 (Lim et al. 2012). Artifacts can also be seen imprinted on the final image in the form of faintly over-subtracted vertical

---

<sup>3</sup><https://www.cadc-ccda.hia-iha.nrc-cnrc.gc.ca/en/wirwolf/>



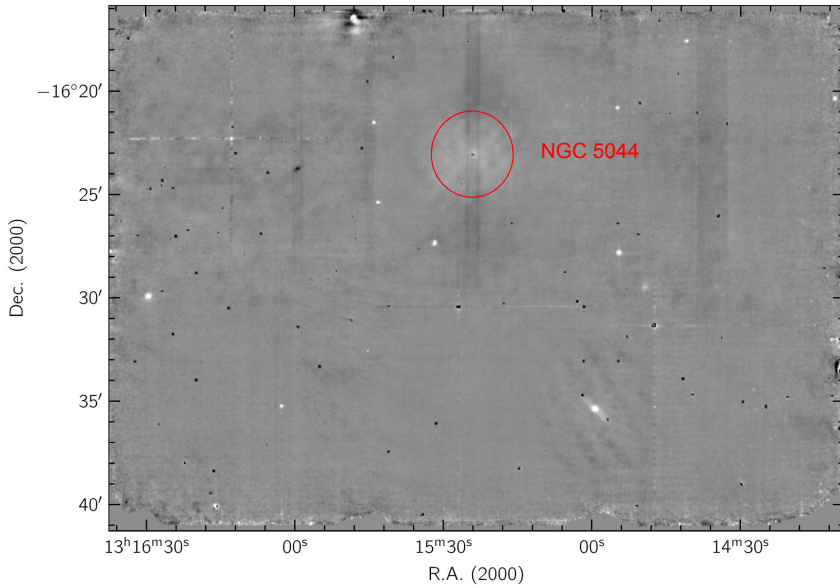


Figure 2.3 My original continuum-subtracted H<sub>2</sub> narrowband image, showing multiple problems owing to the automatic background subtraction performed at CFHT. The position of NGC 5044 is indicated by the red ellipse.

stripes around the bright extended sources. In addition, the central region of the galaxy showed a significant negative residual after subtraction, increasing in depth towards the center, thus revealing an *apparent* smooth, monotonic color gradient in the stellar continuum of the galaxy extending from the center all the way out to beyond 30'' (i.e. the scaling factor between the H<sub>2</sub> and Ks filters appeared to be radially-dependent).

My initial approach when confronted with this apparent color gradient was to attempt to construct and apply a radially-dependent scaling factor to multiply by the Ks image before subtraction from the H<sub>2</sub> image. I constructed the radially-dependent scaling factor by generating a set of elliptical continuum isophotes and then calculating the optimum scaling factor by finding the average Ks-to-H<sub>2</sub> ratio in the annular region between each pair of adjacent isophotes. Since I was trying to scale the Ks image to the *continuum* in the H<sub>2</sub> narrowband image, this procedure only works if pixels containing H<sub>2</sub> emission are excluded.



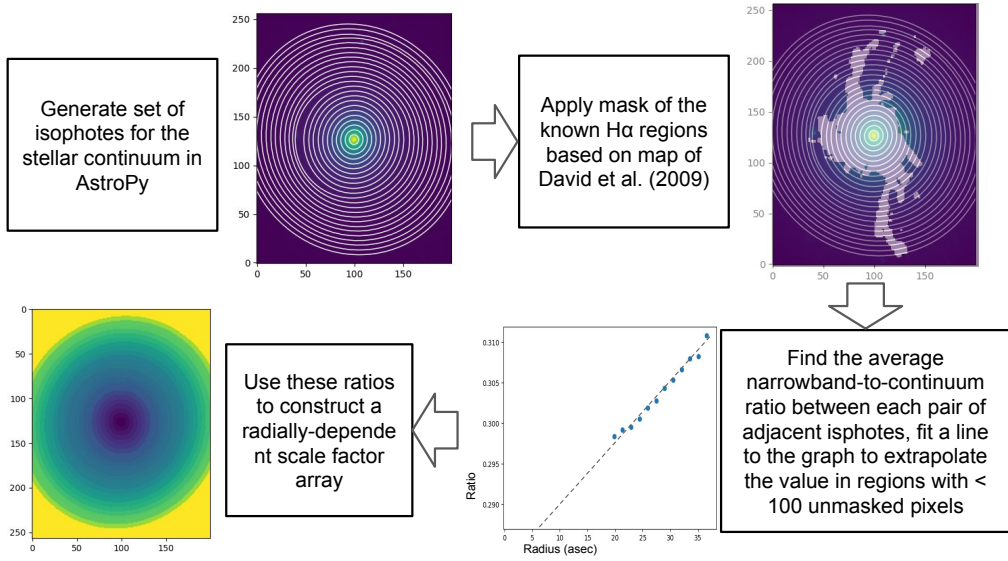


Figure 2.4 Procedure for generating a radially-dependent scale factor for subtraction of the stellar continuum from the narrowband image in the presence of a color gradient

I excluded pixels potentially containing H<sub>2</sub> emission by blanking out all regions with H $\alpha$  emission above 3 sigma based on the H $\alpha$  map in David et al. (2009). The steps of the procedure are outlined in figure 2.4. However, this procedure was limited in that it could not derive an appropriate off-nebula continuum scaling factor at small radii ( $\lesssim 10''$ ) because the inner part of the nebula entirely overlaps the annular regions. Therefore, I had to extrapolate the scale factor in the inner nebula from the line of best fit to the scale factor vs radius scatter plot.

Although applying a radially-dependent scale factor helped to an extent, it still left an over-subtracted residual image in the inner part of the nebula after continuum subtraction. Moreover, there was still the issue of the faint vertical stripe artifacts. Therefore, I suspected that the radially-dependent scaling factor was in fact an artifact of the data reduction process. By examining the raw frames I used to create the stacked images closely, I determined that the

artifacts present in the subtracted image were caused by issues arising from the ‘I’wii sky subtraction method. Specifically, the sky-subtracted images exhibited over-subtracted patches around bright extended sources resembling the dithering pattern, indicating that the afterimages had become imprinted on the sky frames. To correct this problem, I developed my own sky construction and subtraction strategies to apply to the detrended frames. The steps of the sky construction are outlined in figure 2.5. As shown in figure 2.2, the target appeared on detector 4 and 1 during A and B nods respectively. During A nods, the target appeared on detector 4, so I used the B nod frames from detector 4 to construct the sky for the A nod frames. Similarly, the A nod frames from detector 1 were used to construct the sky, which was subtracted from the B nod frames from detector 1. I assigned an observation time (MJD, Modified Julian Date) to each of the sky frames by taking the average of the MJDs of the frames used to construct them. I then used this to determine which sky frame to subtract from a given frame when performing the sky subtraction, with the sky frame with MJD closest to that of the target frame being used in each case.

Although the quality of the sky subtraction improved after applying this strategy, some artifacts still remained: afterimages of a bright source in the field of detector 4 during B nods were imprinted on the sky, and for some frames the sky subtraction left a faint residual due to time variation of the brightness of the NIR sky signal as well as the telescope.

After constructing and subtracting the sky as detailed above, I ran the sky-subtracted frames through the stacking pipeline again. The results, while free from the vertical stripes and circular artifacts seen in the automatically sky-subtracted stacked frames, exhibited asymmetry in the background subtraction around the target. After excluding 153 out of 253 narrowband H<sub>2</sub> and 122



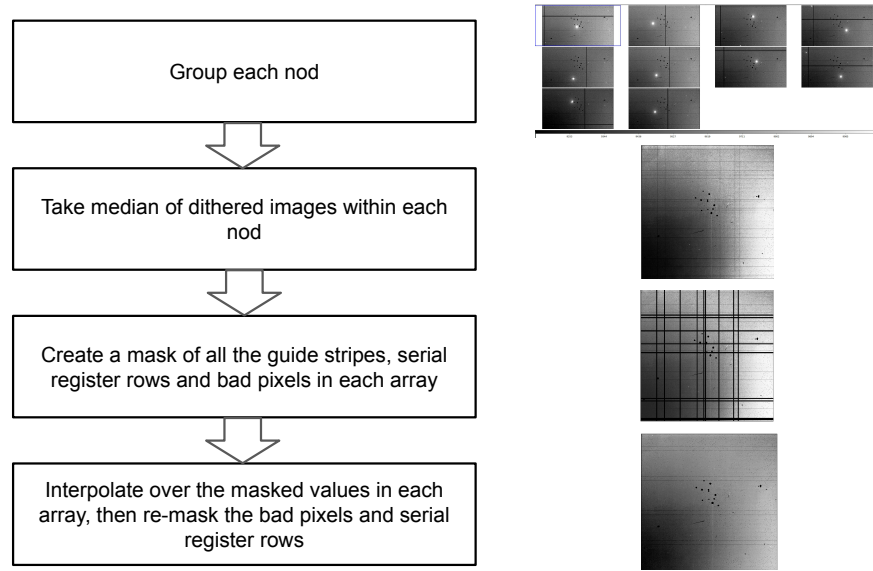


Figure 2.5 Sky construction procedure showing stills from DS9 at each stage

out of 212 Ks continuum frames (where the sky subtraction was found to be of insufficient quality), I stacked the frames again and subtracted the Ks continuum from the H<sub>2</sub> narrowband image. The resulting image was free from artifacts, but the radial color gradient remained. In order to understand the nature of this gradient better, I plotted the azimuthally-averaged ratio of the narrowband to continuum filter against distance from NGC 5044's center, an example of which is shown in Figure 2.6. I then tried adding small artificial DC offsets to the continuum image to see what effect it had on the radial dependence of the ratio. I manually added a variety of test values and noted the effect on the graph of azimuthally-averaged ratio vs radius. I discovered that adding a small positive DC offset to the continuum filter removed the radial gradient (i.e. flattened the graph) except within the central  $\sim 3''$  of the galaxy, where a persistent dip in the narrowband to continuum ratio remained (this dip can be seen as a negative residual in the subtracted image as seen in Figure 2.21). By analyzing the background level surrounding NGC 5044 before and after adding the artificial

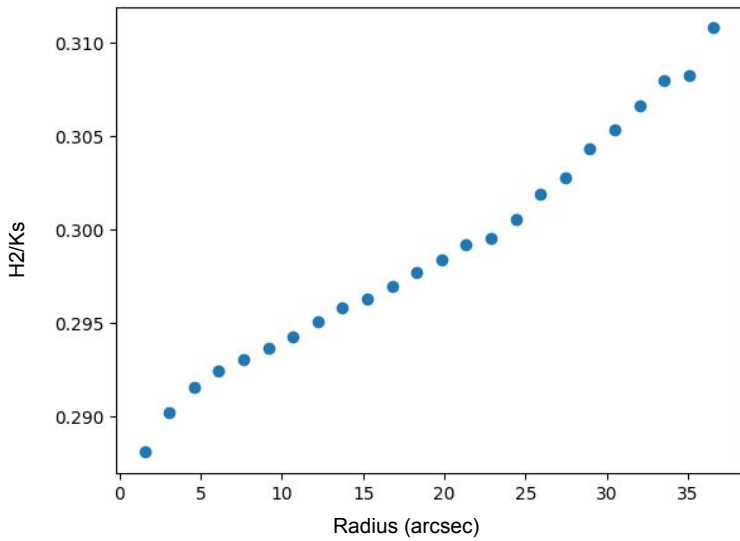


Figure 2.6 A representation of the plots of azimuthally-averaged narrowband/Ks ratio vs radius that I used to fine-tune the DC offset and thus perform an accurate continuum subtraction.

DC offset, I confirmed that the former was slightly below zero, while the latter value was consistent with zero background level. This confirmed that most of the apparent color gradient in the stellar continuum of the NGC 5044 was in fact caused by tiny imperfections in the sky subtraction, rather than being of astrophysical origin. Nevertheless, there remained a residual dip – i.e. an over-subtracted region – within the central  $\sim 3''$  of the galaxy, suggesting that the color change at the center was not an artifact of the data reduction procedure.

In order to investigate the color change in the center of NGC 5044, I decided to compare its morphology and depth with a known IR color change between the Spitzer  $3.6\mu\text{m}$  and  $4.5\mu\text{m}$  filters. To this end, I obtained infrared (IR) imaging of NGC 5044 from the Spitzer Heritage Archive (Fazio et al. 2004). I obtained three mosaics in the  $3.6\mu\text{m}$  filter and three in the  $4.5\mu\text{m}$  filter from the IRAC instrument (pre-processed “level 2” data). I performed a rudimentary background subtraction with ASTROPY by subtracting the sigma-clipped median

from each of the mosaics with 10 iterations of clipping at the 3-sigma level. I then stacked each set of three mosaics in the respective filters. After stacking, I performed a cross-convolution of the two resulting images as follows. The PSF of each image was taken to be Gaussian with the FWHM measured by manually inspecing a selection of bright stars using AstroImageJ (Collins et al. 2017). Each image was then convolved with a Gaussian kernel of the same FWHM as the other image, thus resulting in PSFs of equal width in each image. I then resampled the cross-convolved images onto the same grid using SWARP (Bertin et al. 2002) and performed a subpixel alignment using SciPy’s NDIMAGE package, before finally generating a ratio image of the  $3.6\text{ }\mu\text{m}$  and  $4.5\text{ }\mu\text{m}$  filters, shown in Figure 2.14. I consider the relationship this color change may have with the CFHT circum-nuclear color change, if any, in 2.2.

### 2.1.2 Spectroscopy

#### 2.12 micron $\text{H}_2$ 1-0 S(1) line

Rather than settling for an upper bound for the  $\text{H}_2$  line surface brightness from NGC 5044 as inferred from my imaging results, I decided to search telescope archives for spectroscopic observations of  $\text{H}_2$  emission from NGC 5044. This would allow me to study the kinematic relationship between  $\text{H}_2$  and other nebular components in different phases and/or temperatures, thus opening new avenues of investigation into the excitation of the nebular gas. I found near-infrared spectroscopic data spanning the  $2.12\text{ }\mu\text{m}$   $\text{H}_2$  line in the ESO archive, which was taken using the Infrared Spectrometer And Array Camera (ISAAC) instrument (Moorwood et al. 1998) on the Very Large Telescope (VLT) on 2010 May 3 for a total integration time of 220 minutes. The observation was made using the long slit spectrograph with a slit of length  $120''$  and width  $1''$ . The 1.8900



- 2.5000  $\mu\text{m}$  SK filter was used, with total wavelength coverage on the detector of 2.126081 - 2.241041  $\mu\text{m}$  and spectral resolution (FWHM) of  $\sim 0.00078 \mu\text{m}$  (or  $109 \text{ km s}^{-1}$ ) at the wavelength of the redshifted H<sub>2</sub> ( $\sim 2.1400 \mu\text{m}$ ). A nodding pattern with a throw of  $60''$  parallel to the slit length was used in the observations to allow A-B-B-A sky subtraction – explained in more detail below – without overlap of the nebula between the A and B nod positions (the nebula as imaged in H $\alpha$  extends less than  $60''$  along the slit as shown in Figure 2.18). The detector pixel scale was  $0.148''/\text{pix}$  and seeing on the night of observations was approximately  $1.6''$ .

When observing the target, the slit was centered on the peak brightness of the continuum (i.e. coinciding with the AGN) and oriented at a position angle of  $30.4^\circ$  as shown in Figure 2.18. The slit therefore covers the nucleus and cuts through the roughly circular bright inner part of the nebula, as well as cutting through a knot in the outer nebula on the north-western side which shows up in the H $\alpha$  image. Apart from NGC 5044, observations were also made of a photometric standard star, HIP 68970, on the same night.

I performed bias correction, dark subtraction, flat fielding, distortion corrections, wavelength calibration, and A-B-B-A sky subtraction using the ESO ISAAC pipeline. The result of this pipeline for both the galaxy and the standard star observations is a 2-dimensional FITS image of the long slit spectrum, with the spatial dimension on the y axis and the wavelength along the x axis. I then photometrically calibrated the standard star spectrum using a model spectrum of the same spectral type (B9V) along with it's known 2MASS K band magnitude. I then derived a 1D wavelength-dependent conversion factor from counts to flux by dividing the calibrated standard star spectrum by the uncalibrated spectrum and slightly smoothed it to remove pixel-to-pixel noise.



Next, I extracted 1D spectra from the 2D slit spectrum of NGC 5044, summing over apertures of width  $0.8''$  along the spatial (y) axis (i.e. Nyquist sampling given the FWHM of  $1.6''$ ). Since the native pixel scale of ISAAC is  $0.148''$ , I had to resample the data along the spatial axis before extracting the spectra. I then used the conversion factor derived from the standard star to flux-calibrate each extracted spectrum.

While most telluric features were removed by the A-B-B-A sky subtraction and flux calibration, some residual features due to OH line emission can be seen in the resulting flux-calibrated spectra, of which the closest to the H<sub>2</sub> line are at  $2.1505044\text{ }\mu\text{m}$  and  $2.1537522\text{ }\mu\text{m}$ . Furthermore, an apparent detector defect is visible to the south-east of the nucleus between  $\sim 2.1347\text{ }\mu\text{m}$  and  $\sim 2.1366\text{ }\mu\text{m}$  and absorption features can be seen between  $\sim 2.1347\text{ }\mu\text{m}$  and  $\sim 2.1387\text{ }\mu\text{m}$  that I attribute to AlI absorption in stellar atmospheres. I masked these regions when fitting the H<sub>2</sub> line profiles and continuum (as detailed in 2.2).

Upon analyzing the initial fitting results, I noticed that the spectral baseline in the calibrated NIR spectra exhibited a dependence on the position, with positions towards the nucleus having steeper downward-sloping baselines (i.e. smaller slopes). Initially, I believed this to be related to the aforementioned putative color gradient seen in my imaging results. However, once the color gradient in the imaging data was determined to be due to imperfect background subtraction, I searched for another possible origin for the radially-dependent slope in the NIR baselines. By measuring the PSF of the standard star spectrum along the spatial axis at each wavelength, I determined that the size of the PSF had a strong dependence on the wavelength. To account for this, I convolved the standard star with gaussian kernels along the spatial axis at each



wavelength to  $1.92''$ , and used the same Gaussian kernels to convolve the spectrum of NGC 5044 to the same FWHM at each wavelength. This eliminated the radial dependence of the baseline slope, and brought the final (spatial) FWHM of the H<sub>2</sub> observations to  $1.9''$ .

### H $\alpha$ + [NII] line

Since the focus of my study had now shifted to spectroscopy of the NIR H<sub>2</sub> line, I looked for spectroscopy of the H $\alpha$  line, which would allow me to find line ratios as well as use the line profiles to test the idea that the H<sub>2</sub> and H $\alpha$  emission originate in the same gas volume. I found optical spectroscopy spanning the H $\alpha$  line and the adjacent [NII] lines in the ESO archive. This data was obtained using the MUSE integral field unit (IFU) on the VLT on 2015 February 10 with a total integration time of 69 minutes. The observation spanned wavelengths from  $4750\text{ \AA}$  to  $9350\text{ \AA}$  with a spectral resolution of  $\sim 2.6\text{\AA}$  ( $117\text{km s}^{-1}$ ) at the central wavelength, thus clearly separating the H $\alpha$  and [NII] lines in all positions except for NGC 5044's nucleus. The instrumental scale was  $0.2''/\text{spaxel}$  and the seeing on the night of observation was approximately  $0.6''$ , with a field size of  $60\times 60''$ . Pre-processing including bias subtraction, dark subtraction, flat fielding, and wavelength calibration, as well as photometric calibration, was carried out automatically at ESO using the MUSE 1.6.1 ESO pipeline (Weilbacher et al. 2020).

Since MUSE is an IFU, the data is in the form of a data cube, where each spaxel (the IFU equivalent of a pixel) contains a spectrum. Therefore, in order to make a one-to-one comparison between the H $\alpha$  spectra taken with MUSE and the H<sub>2</sub> 1-0 S(1) spectra taken with ISAAC, I generated a simulated long-slit spectrum from the MUSE data cube using the QFITSVIEW software



package (Ott 2012). The slit position and orientation were chosen to match that of the ISAAC data: the slit was centered on the brightest pixel in the image (presumably marking the location of the AGN) along a position angle of  $30.4^\circ$ . Prior to extracting the simulated longslit spectrum, I convolved the data cube along the spatial axes with a Gaussian kernel with FWHM  $= \sqrt{\text{FWHM}_{\text{ISAAC}}^2 - \text{FWHM}_{\text{MUSE}}^2} = \sqrt{1.9^2 - 0.6^2}$  to match the angular resolution of the ISAAC data ( $\sim 1.9''$ ). From the resulting 2D spectrum, I extracted spectra at positions along the slit matching as closely as possible the spatial locations of the extracted H<sub>2</sub> spectra by extracting spectra along the slit from apertures of width  $0.8''$ . I took care to place the central aperture over the brightness peak (as was done with the H<sub>2</sub> spectra) so that the H<sub>2</sub> and H $\alpha$  apertures would match as closely as possible. I performed an identical procedure on the MUSE variance data cube and then took the square root to obtain 1 sigma uncertainties for each of the spectra.

### 1.3 mm CO(2-1) line

After having conducted an analysis of the H<sub>2</sub> and H $\alpha$  lines from NGC 5044, I learned that some of our collaborators (see co-authors at the beginning of 2.4) had conducted and processed two separate ALMA + ACA observations of the CO(2-1) 1.3mm line from NGC 5044. By this time, I had already seen a very close resemblance between the spectral profiles of H<sub>2</sub> (which usually traces warm molecular gas) and H $\alpha$  (which usually traces hot atomic/ionized gas). I therefore wanted to see if the similarity in line profiles extended to cold molecular gas as traced by CO. The first observation used ALMA in cycle 0 with the full 12 m array (taken on 2012 January 13), while the second used



ACA during cycle 4 with the 7 m array (taken on 2017 July 13). The total on-source integration times for the ALMA and ACA observations were 29 minutes and 306 minutes respectively, while the primary beam sizes were  $27''$  and  $42''$  respectively. Thus the bright inner region of the nebula was covered but not the outermost filaments (see Figure 2.18). Further details of the ALMA and ACA observations can be found in David et al. (2014) and Schellenberger et al. (2020) respectively. The data were processed by our collaborators in CASA and combined to form image cubes with a spectral resolution of  $\sim 10 \text{ km s}^{-1}$  and a synthesized beam of  $\sim 2.3'' \times 1.5''$  at a position angle of  $\sim 30^\circ$ . Similarly to the H $\alpha$  data reduction outlined above, I then used QFITSVIEW to simulate long-slit spectroscopy from the data cube, with slit position and dimensions chosen to match the ISAAC observations of the H $_2$  2.12  $\mu\text{m}$  line as closely as possible: the simulated slit was centered on the AGN with a position angle of  $30.4^\circ$  and a width of  $1.2''$  (slightly wider than the  $1''$  of the ISAAC slit). I then extracted 57 spectra from apertures of width  $0.8''$  along the slit (there are fewer spectra as the primary beams do not cover the entire length of the ISAAC slit). Due to the limited velocity range of the spectra, I was unable to smooth to match the resolution of the H $\alpha$  and H $_2$ , as otherwise the convolution kernel would extend far beyond the bounds of the spectrum leading to significant edge effects over the entire frequency range. Instead, I simply smoothed the spectra along the frequency axis with a Gaussian kernel of width 3 channels to reduce noise.



## 2.2 Results

### 2.2.1 Imaging of the 2.12 micron H<sub>2</sub> 1-0 S(1) line

#### Obtained sensitivity

Even after having corrected for all the complications associated with the continuum subtraction of the H<sub>2</sub> narrowband imaging mentioned in Chapter 2.1, subtraction of the continuum from the H<sub>2</sub> 1-0 S(1) narrowband filter did not reveal any H<sub>2</sub> emission from NGC 5044. Nevertheless, the (flux calibrated) noise level in the resulting continuum-subtracted image could be used as an upper bound on the surface brightness of the H<sub>2</sub> line from the nebula. This also provided me with an opportunity to check if there were problems with my data reduction: if the noise level was far too high given the total exposure time (or far too low considering that no H<sub>2</sub> emission was detected) it could point to mistakes in my handling of the data. In order to find the rms noise level in units of flux, I first had to photometrically calibrate the H<sub>2</sub> image from which the continuum was subtracted. I did this by choosing a bright star in the H<sub>2</sub> narrowband stacked image that was also included in the 2MASS catalog. This allowed me to derive a conversion factor between counts and erg s<sup>-1</sup> cm<sup>-2</sup> asec<sup>-2</sup>. I then scaled the rms noise in counts in the continuum-subtracted image by this conversion factor to give a noise level of  $5 \times 10^{-16}$  erg s<sup>-1</sup> cm<sup>-2</sup> asec<sup>-2</sup>. Based on the results of the spectroscopy that I afterwards conducted, I found the maximum circum-nuclear H<sub>2</sub> surface brightness to be  $\sim 4 \times 10^{-16}$  erg s<sup>-1</sup> cm<sup>-2</sup> asec<sup>-2</sup>, which would give a signal-to-noise ratio (SNR) of  $\sim 0.8$  around the nucleus; however, the inner 4.5'' of NGC 5044 is, as noted before, affected by a color change of unknown origin leading to a negative residual, which thus precludes the possibility of seeing H<sub>2</sub> emission from the circum-nuclear region. The SNR falls to  $\lesssim 0.08$



in the outer filaments, where the H $\alpha$  flux is at least an order of magnitude smaller (and thus presumably H<sub>2</sub> is also, assuming an approximately constant line ratio). I also estimated what the SNR would have been if I had used the full 253 narrowband H<sub>2</sub> frames rather than just the 100 frames that my background subtraction had worked sufficiently well on: scaling the SNR by a factor of  $\sqrt{253/100}$  it becomes  $\sim 2$  in the bright circum-nuclear region and  $\sim 0.2$  in the dimmer outer filaments. Thus it is clear that the failure to detect H<sub>2</sub> emission arose from inadequate signal-to-noise.

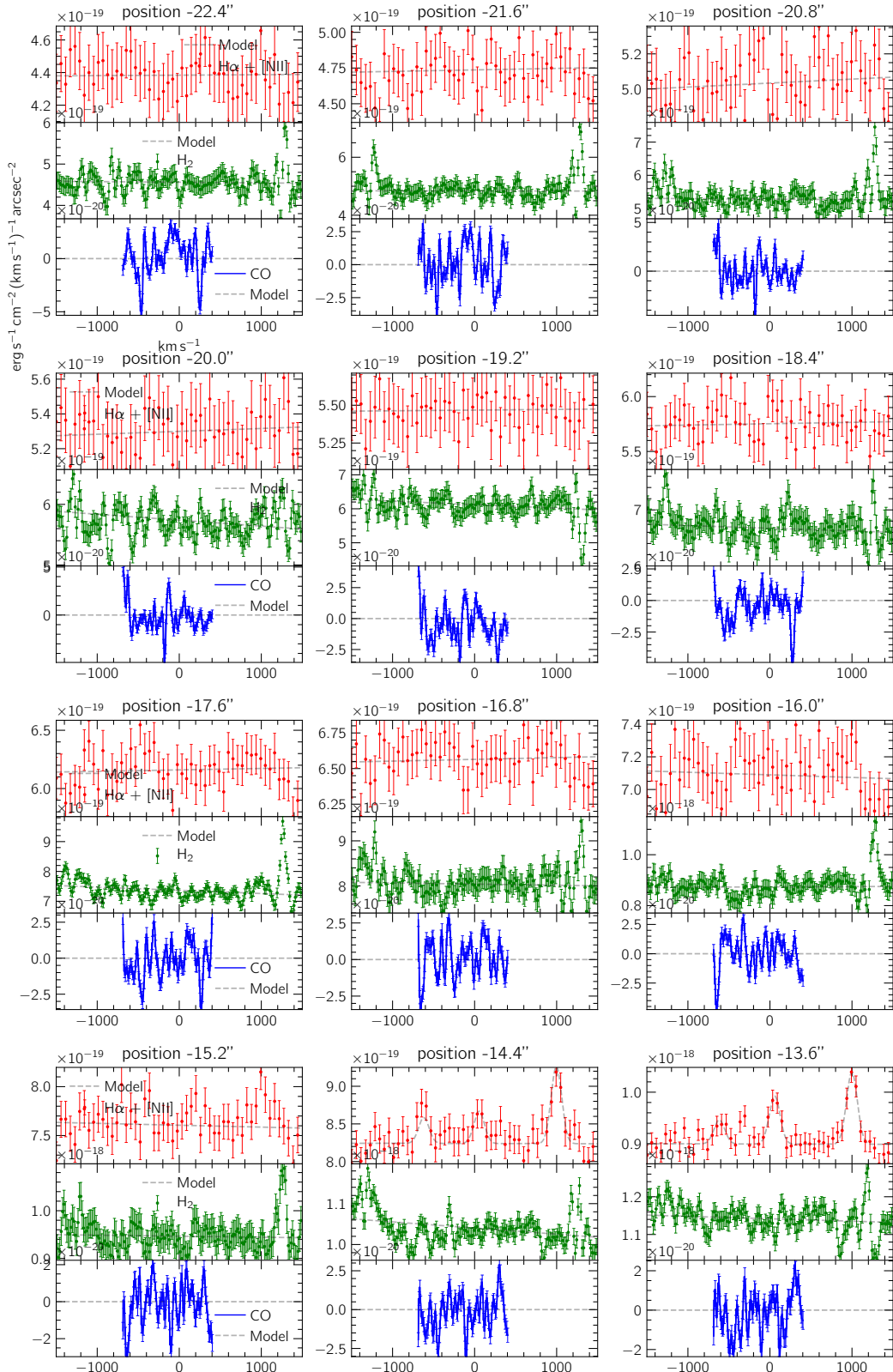
### 2.2.2 Full spectroscopy results

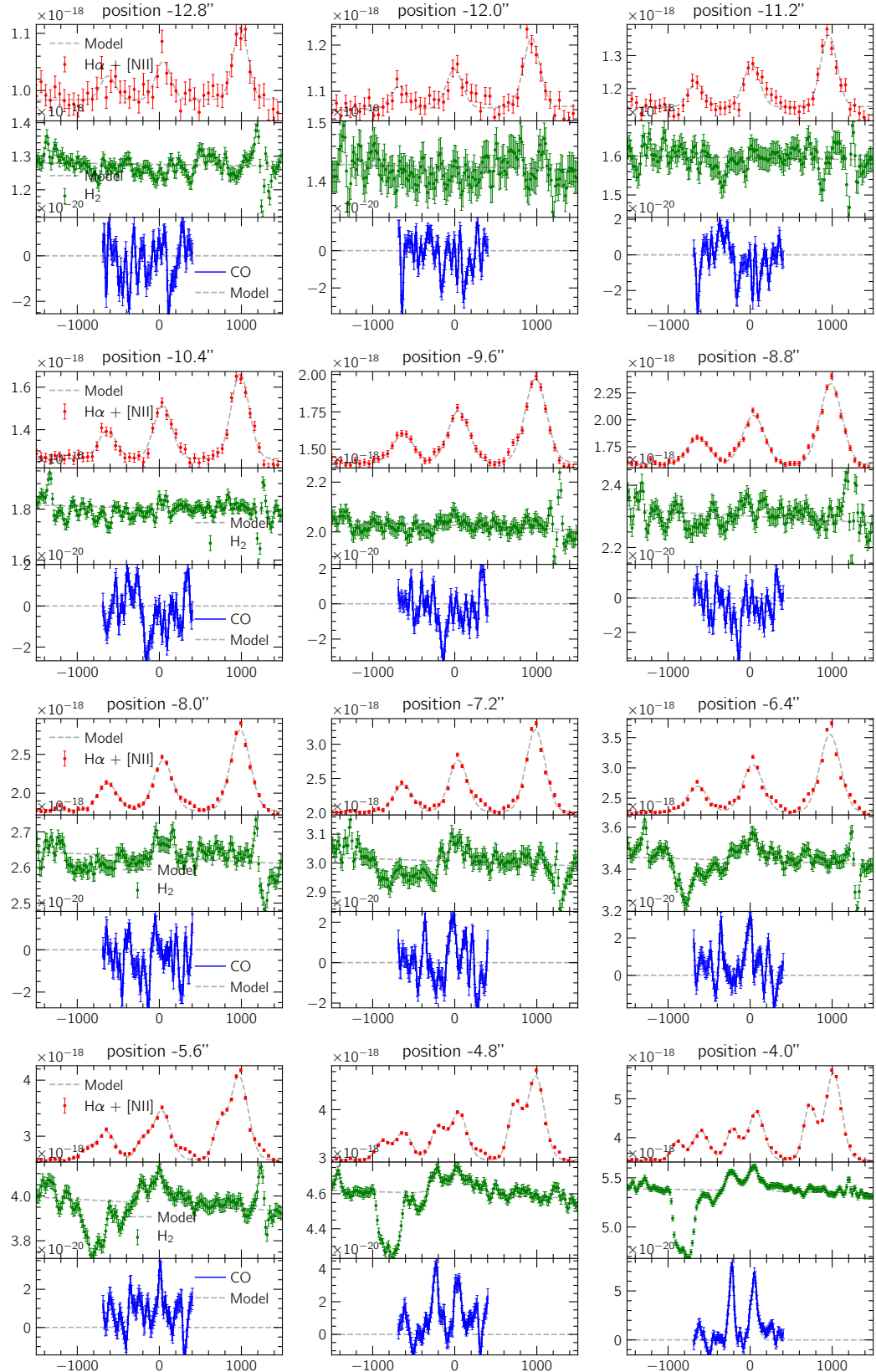
As described in the Paper (2.4.4), I fitted Gaussians to the H $\alpha$ +[NII], H<sub>2</sub>, and CO lines from each aperture (of width 0.8'') along the slit (physical slit in the case of the H<sub>2</sub> spectra, virtual in the H $\alpha$  and CO). I fitted either one or two Gaussians depending on whether the lines appeared to be single- or double-peaked based on visual inspection of the spectra. In addition, I fitted linear baselines to the H<sub>2</sub> and H $\alpha$ +[NII] spectra, though not to the CO spectra as these had already had baselines subtracted. In this Section, I include the full set of H $\alpha$ , H<sub>2</sub>, and CO spectra extracted along the slit, with fitted profiles included where fitting was possible. The results below demonstrate how closely the line profiles from the different gas components resemble each other, how they change in tandem from one position to the next, and how the number of Gaussian peaks tends to be the same for all three lines. These commonalities strongly suggests that the emission lines all originate from common gas volumes. The reader is reminded that, although I smoothed the H<sub>2</sub> spectra to the same spectral resolution as the H $\alpha$  spectra ( $117\text{km s}^{-1}$ ), I left the CO spectra at their original resolution due to their limited velocity range. Hence, the CO lines

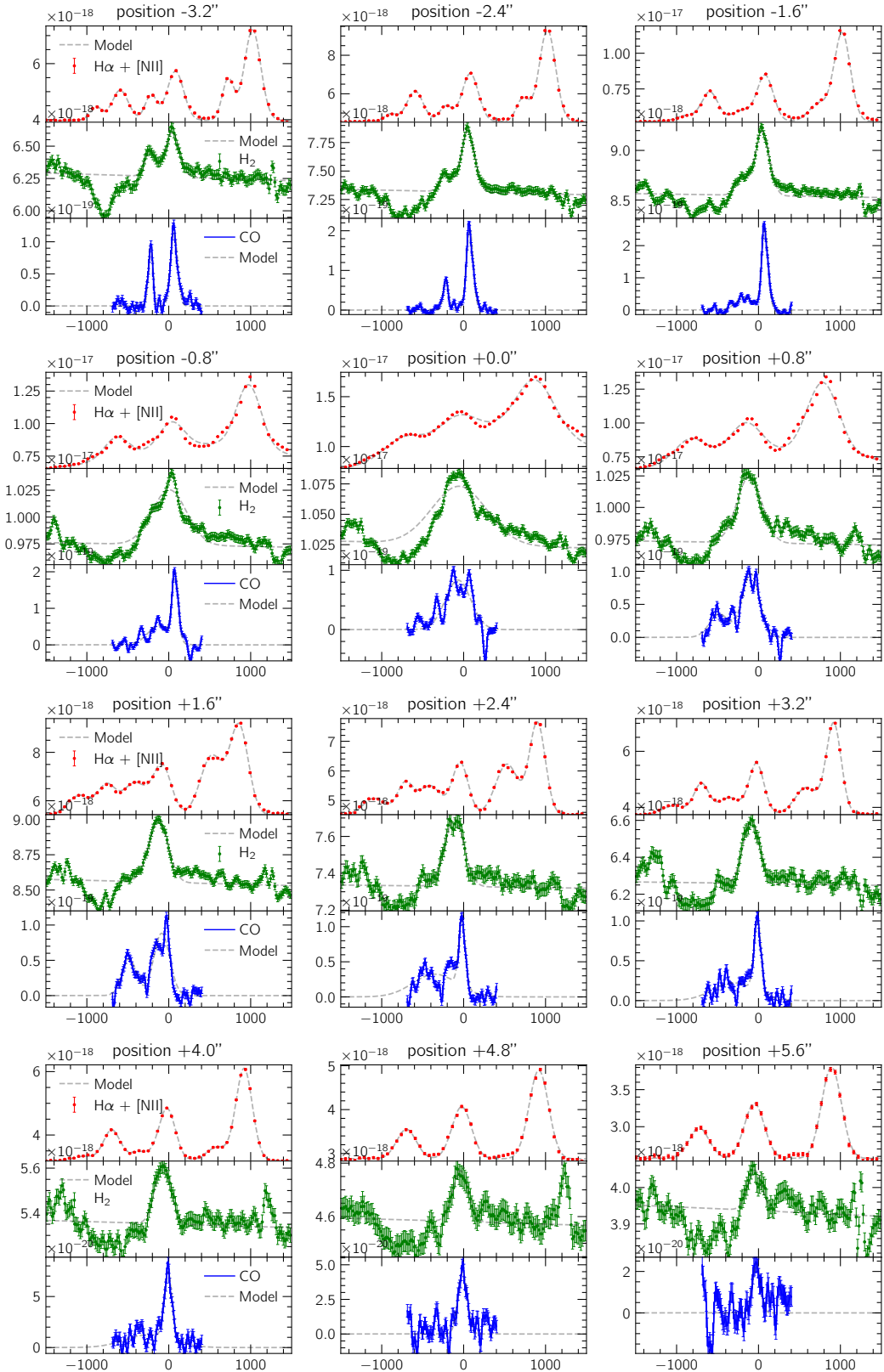


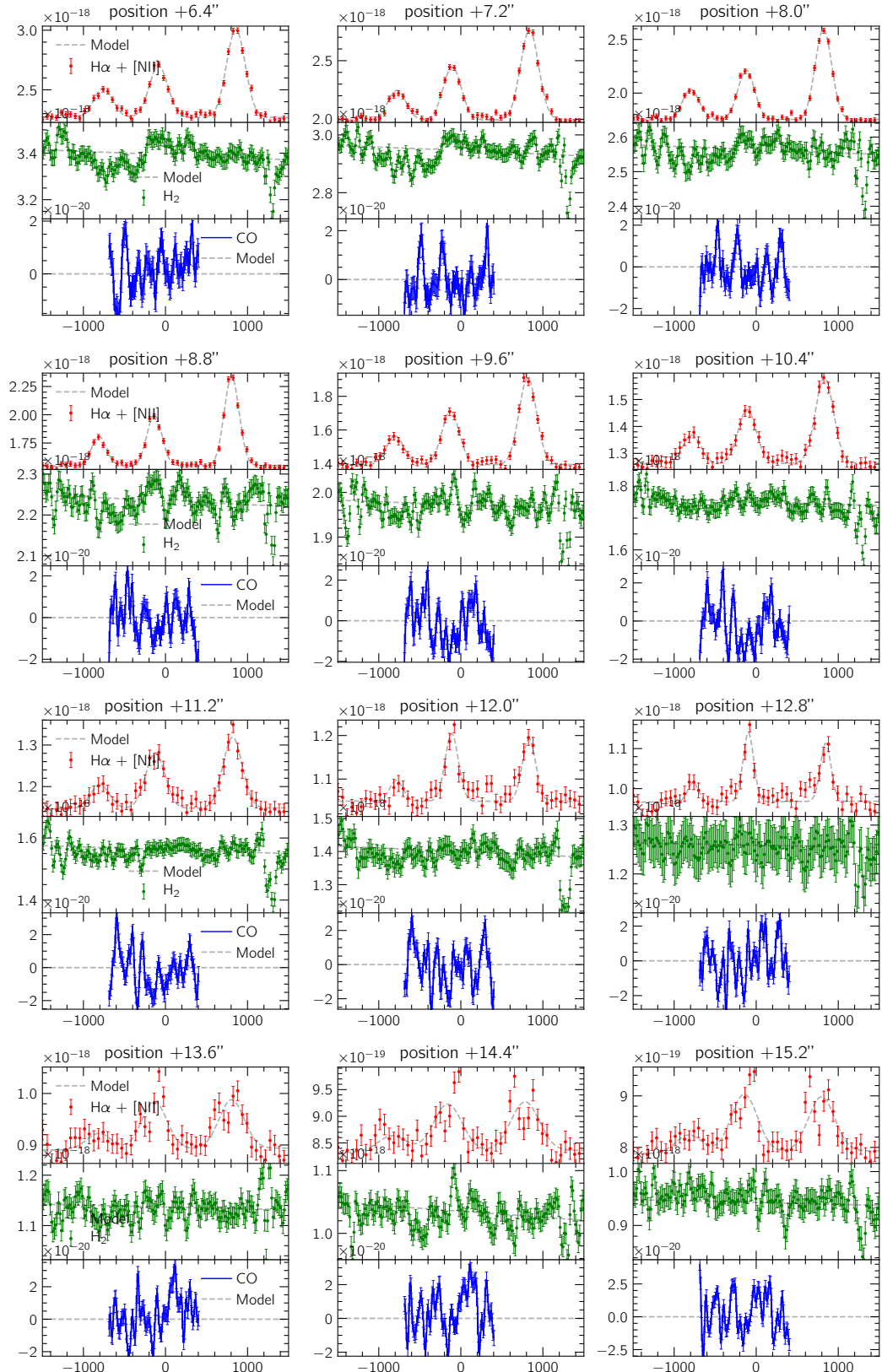
appear far less wide than their H<sub>2</sub> and H $\alpha$  counterparts.



Figure 2.7  $\text{H}\alpha + [\text{NII}]$ ,  $\text{H}_2$ , and CO spectra.

Figure 2.8  $\text{H}\alpha + [\text{NII}]$ ,  $\text{H}_2$ , and CO spectra.

Figure 2.9 H $\alpha$  + [NII], H<sub>2</sub>, and CO spectra.

Figure 2.10  $H\alpha + [\text{NII}]$ ,  $H_2$ , and CO spectra.

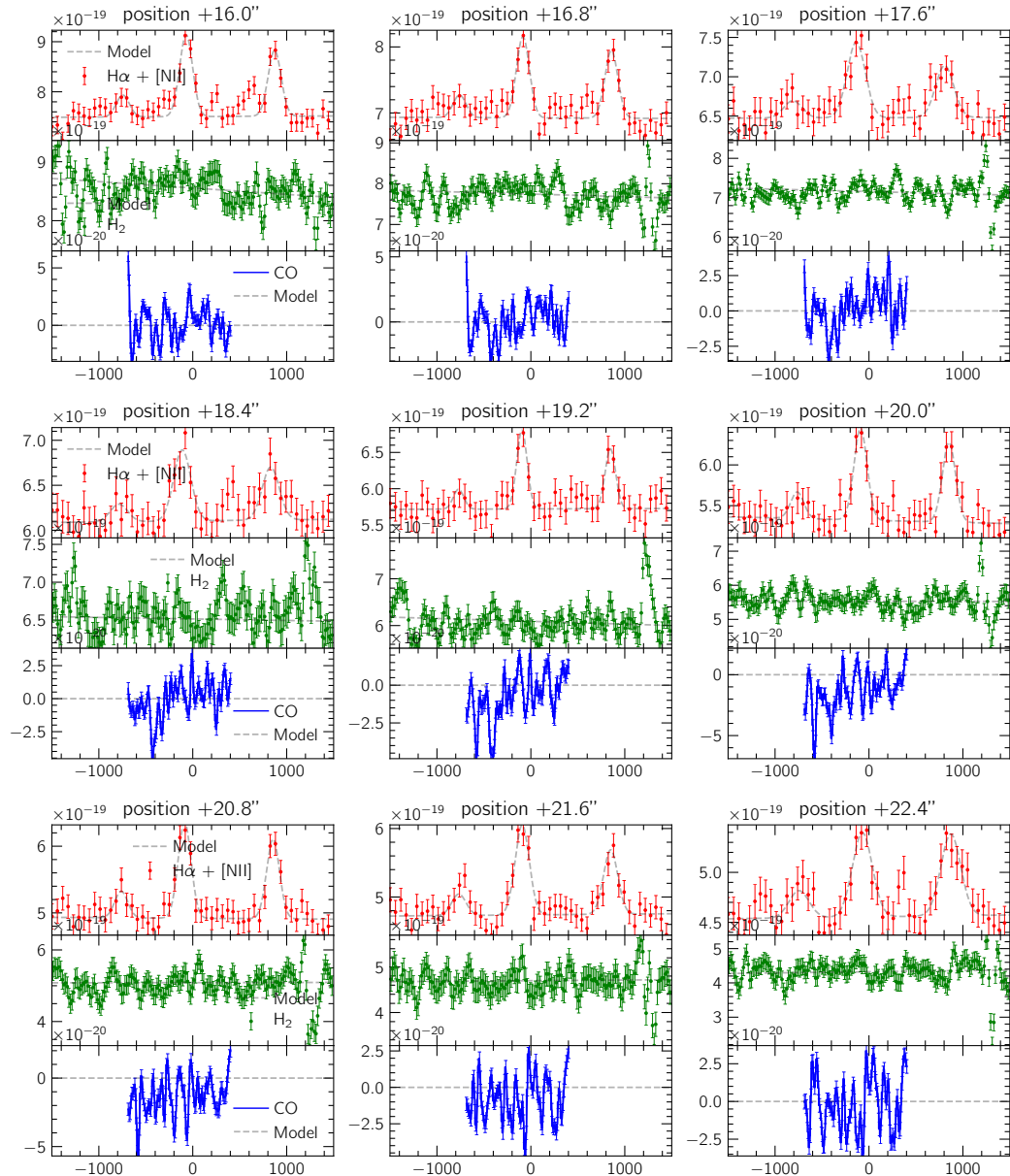


Figure 2.11 H $\alpha$  + [NII], H<sub>2</sub>, and CO spectra.

## 2.3 Discussion

### 2.3.1 Imaging

As I describe in the Paper (2.4.3), the subtraction of the K<sub>s</sub> continuum image from the H<sub>2</sub> narrowband image did not reveal any H<sub>2</sub> emission from the filaments of NGC 5044. Instead, the continuum-subtracted image showed an over-subtracted region at the center of NGC 5044, increasing in depth towards the nucleus. Such an over-subtraction indicates a color change in NGC 5044's stellar continuum.

I considered a number of possible physical origins of the circum-nuclear color change seen in the continuum-subtracted image in Figure 2.21. The central wavelengths/widths of the K<sub>s</sub> and H<sub>2</sub> filters are 2.146/0.325μm and 2.122/0.032μm respectively, meaning that the H<sub>2</sub> filter lies (just) in the blue half of the K<sub>s</sub> bandpass as shown in Figure 2.12. As such, a decrease in the H<sub>2</sub>/K<sub>s</sub> ratio is indicative of a redder color. Using the minimum value at the center of the negative residual feature caused by the color change, I calculated that the H<sub>2</sub>/K<sub>s</sub> ratio falls by about 2% in the inner region relative to the rest of the galaxy. I initially considered the possibility that the redder color was caused by dust in the central region, which is known to exist in NGC 5044 (Temi et al. 2007)). To this end, I obtained an HST dust map (generated by Dr. Ohyama) and overlaid the contours on the continuum-subtracted H<sub>2</sub> image as shown in Figure 2.13, to see if there was any spatial resemblance between them; however, as can be seen in Figure 2.13, no such resemblance is visible. Furthermore, while reddening due to dust is well documented at optical wavelengths, there is no precedent for dust causing reddening at NIR wavelengths.

I also considered the possibility that the color-change was caused either by



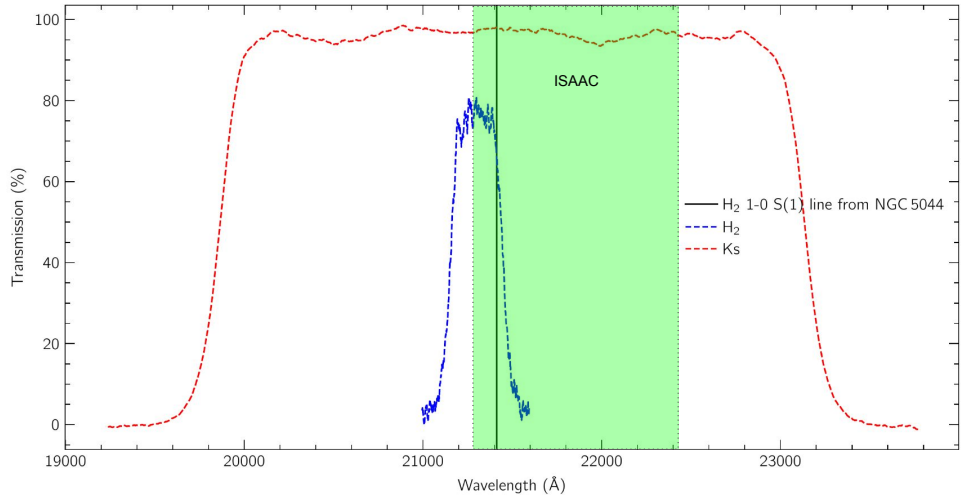


Figure 2.12 WIRCam  $K_s$  and  $H_2$  filter bandpasses with redshifted  $H_2$  line from NGC 5044 shown. Also shown in green is the wavelength range of the ISAAC NIR spectroscopy.

absorption in the  $H_2$  filter bandpass or emission in the  $K_s$  filter bandpass. An inspection of the ratio between the Spitzer  $3.6\mu\text{m}$  filter and  $4.5\mu\text{m}$  filter images revealed a color change towards the center of NGC 5044 as can be seen in Figures 2.14 and 2.15. Furthermore, this color change extends out to  $\sim 5''$  (greater than the FWHM  $\sim 3''$  resolution of the Spitzer images used to make this ratio map), comparable to the extent of the over-subtracted region in the continuum-subtracted CFHT image. However, despite this superficial similarity, a common physical origin for the color change in the Spitzer and CFHT data is unlikely. While the Spitzer  $3.6\mu\text{m}/4.5\mu\text{m}$  ratio is strongly affected by CO absorption in the atmospheres of M giants, CO absorption cannot possibly explain the CFHT color change since 1) the overlap between the CO absorption and the  $K_s$  bandpass is small, with the central velocity of the shortest wavelength CO line ( $^{12}\text{CO}(2-0)$ ) coming in at  $< 50\%$  transmission near the upper bound of the bandpass, and 2) even if a significant amount of CO absorption is present in the

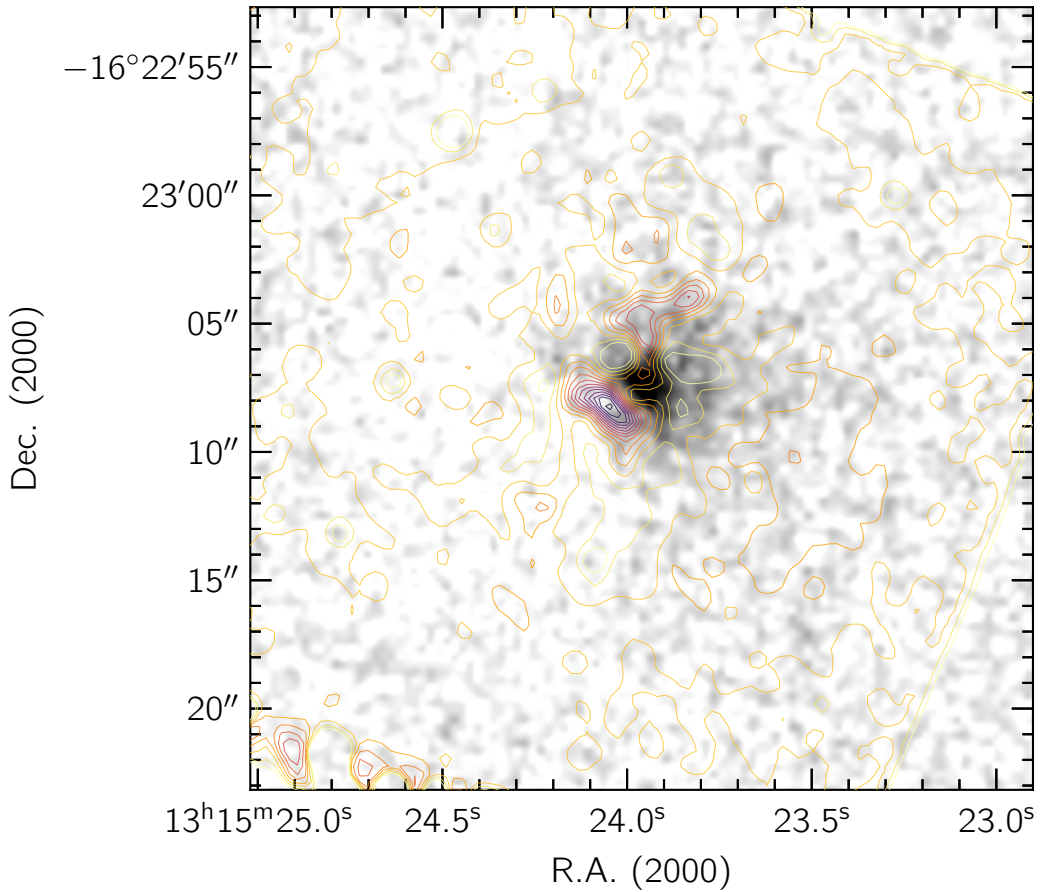


Figure 2.13 HST dust map contours overlaid on a zoom-up of the central region of the continuum-subtracted H<sub>2</sub> image of NGC 5044 (smoothed for clarity).

Ks bandpass, this should have the opposite effect on the H<sub>2</sub>/Ks ratio to what the continuum-subtracted image shows (since no CO absorption can be present in the H<sub>2</sub> bandpass, the H<sub>2</sub>/Ks ratio should increase, leading to a positive residual rather than a negative one). In the absence of any bright emission lines in the Ks bandpass that might cause the H<sub>2</sub>/Ks ratio to drop, I considered the possibility of absorption in the H<sub>2</sub> bandpass. Indeed, our NIR spectroscopic results show an absorption feature just short of the H<sub>2</sub> emission line identified as AlI in Mannucci et al. (2001). However, the depth of this absorption feature alone is not sufficient to explain the pronounced negative residual seen in our

imaging: if the H<sub>2</sub> emission is below the noise level, then the AlI absorption must be as well.

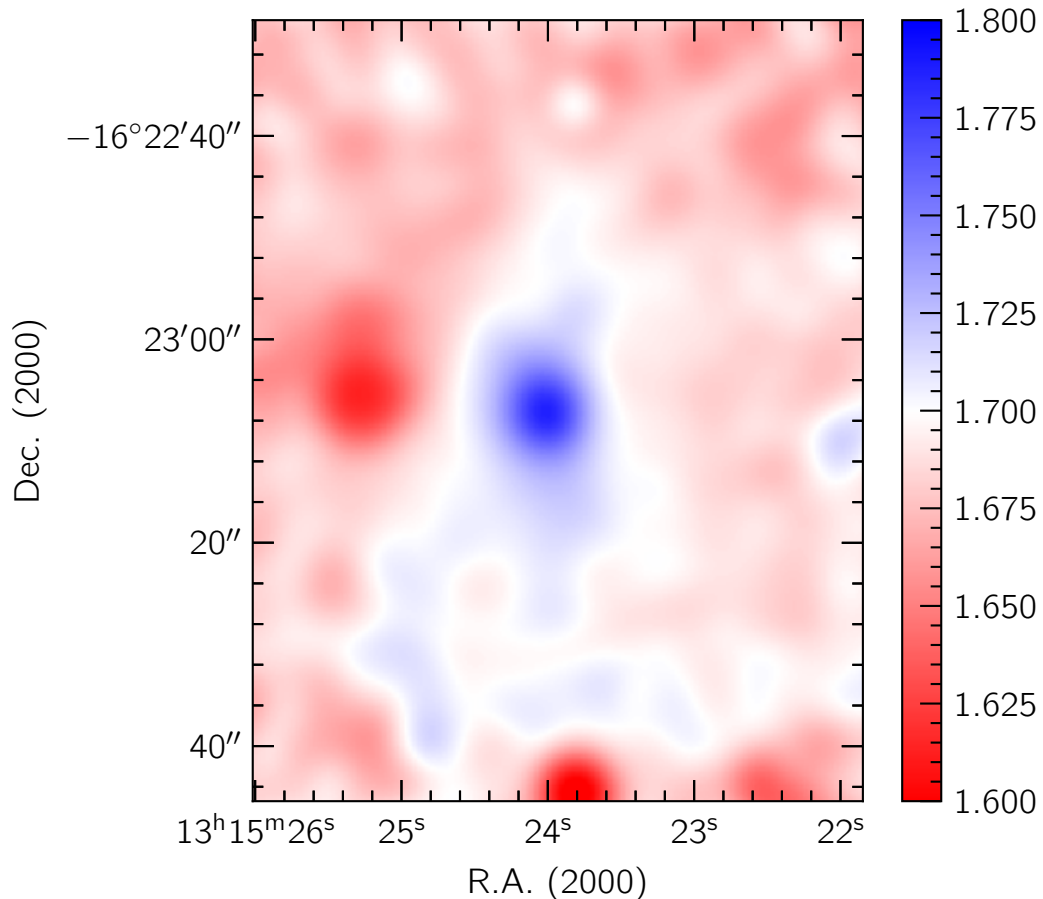


Figure 2.14 Spitzer 3.6 $\mu$ m/4.5 $\mu$ m ratio image showing increase towards the central region of NGC 5044 due to CO absorption.

Finally, I considered whether the color change could be caused by a change in the age of the stellar population in the central region of NGC 5044. I performed a straightforward test of this by calculating the H<sub>2</sub>/Ks ratios of single stellar population (SSP) models. Firstly, I tried using SSPs of varying age with fixed metallicity. I fixed the metallicity at a fiducial value of  $Z = 1.5Z_{\odot}$ , and generated SSPs with ages 0.1, 1, 3, 5, 7, and 10 Gyr. I then used the H<sub>2</sub> and Ks filter curves to generate H<sub>2</sub>/Ks ratios for each of these models. Looking at these results



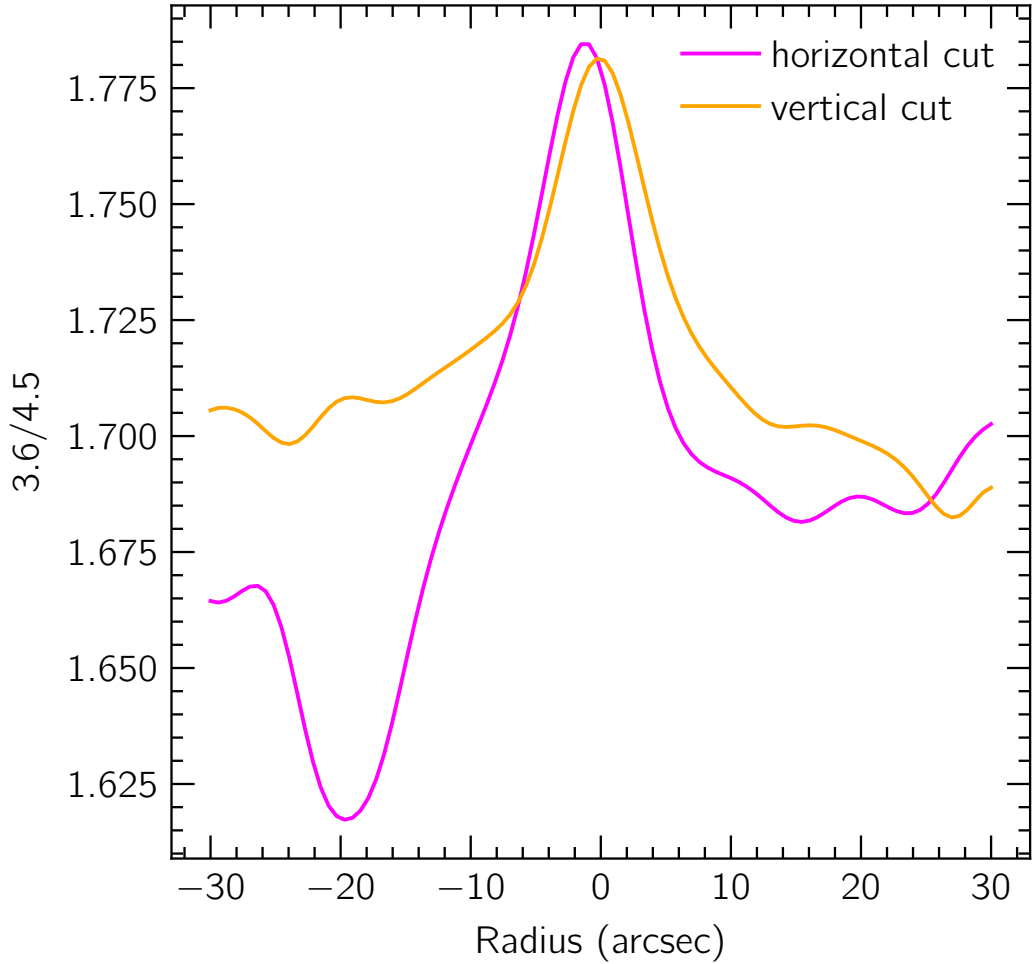


Figure 2.15 Spitzer 3.6/4.5 ratio vs radius along vertical and horizontal cuts through NGC 5044.

showed that the H<sub>2</sub>/Ks ratio falls by  $\sim 2\%$  between 1 Gyr and 5 Gyr, which is similar to the drop in the H<sub>2</sub>/Ks ratio that I calculate from the continuum-subtracted H<sub>2</sub> image. Next, I tried varying the metallicity of the SSPs from  $0.002Z_{\odot}$  to  $2.5Z_{\odot}$  and fixed the age at 10Gyr. By calculating the H<sub>2</sub>/Ks ratios from these SSPs, I found that an increase in metallicity towards the center could account for a decrease in the H<sub>2</sub>/Ks ratio of just  $\sim 0.4\%$ , significantly below the  $\sim 2\%$  seen in the continuum-subtracted image. While these SSP results are clearly very limited, they at least hint that changes in the stellar population

towards the center of NGC 5044 may be able to account for at least some of the change in the H<sub>2</sub>/Ks ratio.

Having established that a changing stellar population could conceivably be behind the color change in the central region, I looked at my NIR spectroscopy results (detailed in 2.1) to see whether they were consistent with this possibility. I therefore fitted linear functions to each of the spectra that I had previously extracted along the long slit used in the NIR spectroscopic observations; as can be seen in Figure 2.19, the stellar continuum is approximately linear across the range of wavelengths covered by the observations. I used these functions along with the H<sub>2</sub> and Ks filter curves to estimate the H<sub>2</sub>/Ks ratio for each of the spectra (again, I refer the reader to 2.1 for more info about the spectroscopy observations and data reduction). At this point, the reader may question why I did not simply use the actual extracted spectra to generate H<sub>2</sub>/Ks ratios rather than the fitted linear baselines. The reason is that the wavelength range of the NIR spectra is only a fraction of the width of the Ks filter, as shown in Figure 2.12, so I had to extrapolate across most of the Ks bandpass. The approximated H<sub>2</sub>/Ks ratios I obtained this way are shown plotted against the position along the slit (i.e. radius) in Figures 2.16 and 2.17. The results suggest that a radial color gradient may indeed exist in the NIR continuum. Moreover, within the central 10'', where signal-to-noise is relatively high, the change in the approximates H<sub>2</sub>/Ks ratio is  $\sim 2\%$ , in line with the change I estimate from the continuum-subtracted image, though the minimum H<sub>2</sub>/Ks ratio appears to be offset from the galactic center by  $\sim +2.5''$ . Thus the spectroscopy results support the possibility of a color change towards the center of NGC 5044. Nevertheless, I caution that 1) the NIR spectra only cover .1150 $\mu$ m out of a total Ks bandpass .3250 $\mu$ m wide, meaning that  $\sim 2/3$  of the data are extrapolated, and



2) the  $\text{H}_2/\text{Ks}$  ratio changes more gradually with radius than the continuum-subtracted image suggests; while the imaging shows a change for radii  $\lesssim 5''$  only, Figure 2.16 shows the trend extending all the way out to  $\sim 20''$ .

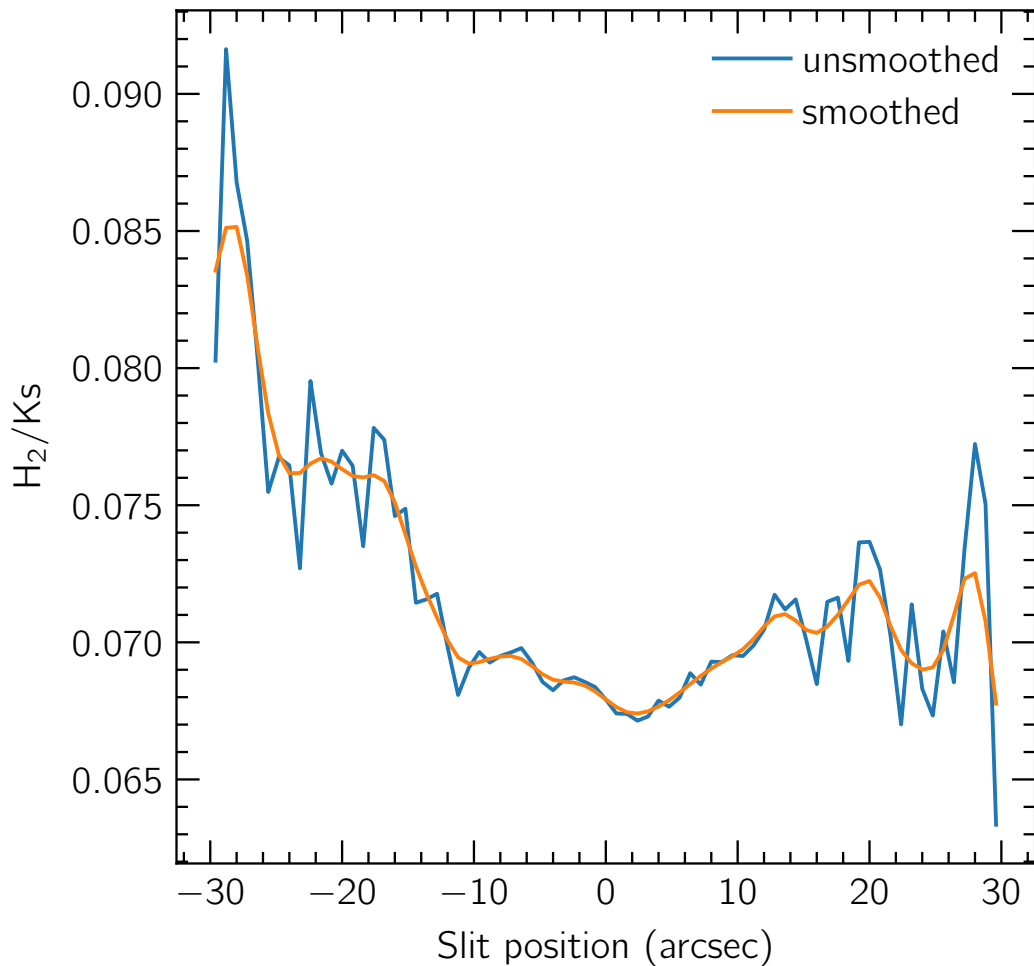


Figure 2.16 Estimates of the  $\text{H}_2/\text{Ks}$  ratio along the ISAAC slit based on the linear baselines fitted to the continua in the NIR spectra.



Taken together, these results hint at the possibility that the circum-nuclear color change in NGC 5044 is caused by an older stellar population with higher metallicity towards the center; however, it is unusual (though not unheard of) for the age of stars in elliptical galaxies to increase towards the center. Comparison of the results shown here with the color change in NGC 5044 at optical

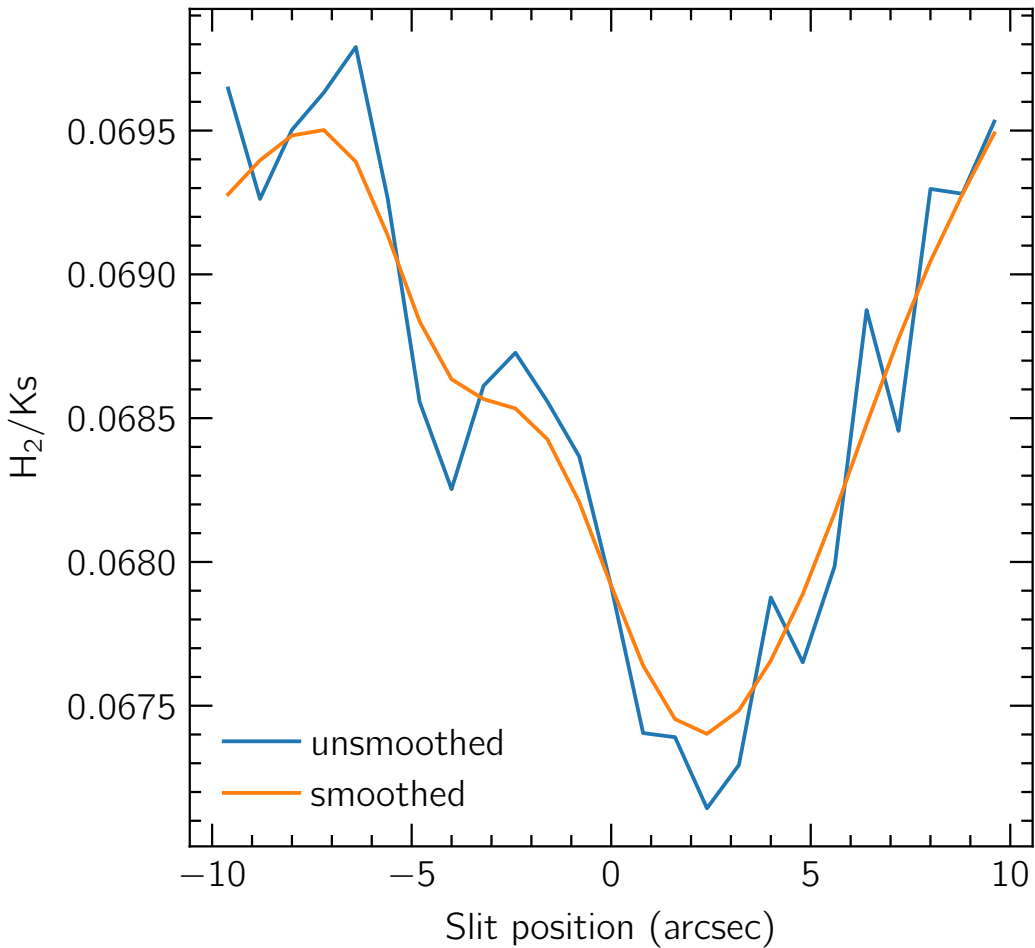


Figure 2.17 Estimates of the  $H_2/K_s$  ratio along the ISAAC slit based on the linear baselines fitted to the continua in the NIR spectra (inner 20'').

wavelengths may help to confirm – or rule out – the possibility of an increasingly old stellar population towards the galaxy's center. However, more thorough investigation of this effect is beyond the scope of this thesis.

### 2.3.2 Spectroscopy

#### Modeling the effects of ICM ram pressure on gas kinematics

Here, I present the full calculations of gas cloud trajectories through the ICM discussed in Section 2.3 in the paper. I start with the net force  $F$  on a gas cloud of mass  $m$  falling towards the center of a galaxy of mass  $M$  while experiencing ram pressure  $p_{ram}$  from the surrounding ICM of density  $\rho_{icm}$ .

$$F = F_g + F_{ram} \quad (2.1)$$

$$= -\frac{GMm}{(r+a)^2} + Ap_{ram} \quad (2.2)$$

$$= -\frac{GMm}{(r+a)^2} + \pi R^2 \rho_{icm} v^2 \quad (2.3)$$

Where  $A$  is the cross-sectional area of the cloud and  $a$  is related to the effective radius of the galaxy by  $R_e \approx 1.8153a$  (see Section 2.3 for more details about where this comes from). Hence, by  $\ddot{r} = F/m$  we have

$$\ddot{r} = -\frac{GM}{(r+a)^2} + \frac{\pi R^2 \rho_{icm}}{m} \dot{r}^2 \quad (2.4)$$

This can also be written in a more intuitively insightful way by making  $A$  and  $m$  into explicit parameters:

$$\ddot{r} = -\frac{GM}{(r+a)^2} + \frac{\rho_{icm} A}{m} \dot{r}^2$$

The coefficient of the  $\dot{r}^2$  term in 2.4 can be rewritten in terms of the mass  $m$  and density  $\rho$  of the cloud:



$$\frac{\pi R^2 \rho_{icm}}{m} = \frac{\pi \rho_{icm}}{m} \left( \frac{V}{4\pi/3} \right)^{2/3} \quad (2.5)$$

$$= \frac{\pi^{1/3} \rho_{icm}}{m} \left( \frac{3}{4} \right)^{2/3} \left( \frac{m}{\rho} \right)^{2/3} \quad (2.6)$$

$$= \left( \frac{3}{4} \right)^{2/3} \frac{\pi^{1/3} \rho_{icm}}{m^{1/3}} \rho^{-2/3} \quad (2.7)$$

We can now use the Ideal Gas Law to write this coefficient in terms of the temperature  $T$  of the gas cloud:

$$\rho = n m_H \quad (2.8)$$

$$= m_H \frac{p}{kT} \quad (2.9)$$

$$= m_H \frac{p_{icm}}{kT} \quad (2.10)$$

Substituting (2.10) and  $\rho_{icm} = n_{icm} m_H$ , where  $n_{icm}$  is the density of the surrounding ICM, into (2.7) we arrive at

$$\ddot{r} = -\frac{GM}{(r+a)^2} + \left( \frac{3kT}{4p} \right)^{2/3} \left( \frac{\pi m_H}{m} \right)^{1/3} n_{icm} \dot{r}^2 \quad (2.11)$$

$$\equiv -\frac{GM}{(r+a)^2} + \kappa \dot{r}^2 \quad (2.12)$$

Thus we see that  $\kappa \propto T^{2/3}/m^{1/3}$ .

Next we move on to solving the differential equation to obtain the trajectories of the clouds.

Let  $\dot{r} \equiv v$ . Next, define  $w(r) \equiv v(t(r))$  (note that  $r(t)$  must be an invertible function over the range of  $r$  considered as the clouds are simply falling inward so never cross the same  $r$  twice). Then by the chain rule we have



$$\frac{dw}{dr} = \frac{dw}{dt} \frac{dt}{dr} = \ddot{r}/\dot{r} \quad (2.13)$$

$$\Rightarrow w \frac{dw}{dr} = \dot{r} \frac{dw}{dr} = \ddot{r} \quad (2.14)$$

$$\Rightarrow w \frac{dw}{dr} = -\frac{GM}{(r+a)^2} + \kappa w^2 \quad (2.15)$$

This differential equation is now in form that can be solved using an integrating factor:

$$w \frac{dw}{dr} - \kappa w^2 = -\frac{GM}{(r+a)^2} \quad (2.16)$$

$$\Rightarrow \frac{d}{dr} (w^2 e^{-2\kappa r}) = -e^{-2\kappa r} \frac{2GM}{(a+r)^2} \quad (2.17)$$

$$\Rightarrow w^2 e^{-2\kappa r} = -2GM \int_{r_0}^r \frac{e^{-2\kappa r'}}{(a+r')^2} dr' \quad (2.18)$$

$$\Rightarrow \dot{r} = w = \left( 2GMe^{2\kappa r'} \int_r^{r_0} \frac{e^{-2\kappa r'}}{(a+r')^2} dr' \right)^{1/2} \quad (2.19)$$

Thus we obtain velocity ( $\dot{r}$ ) as a function of radius  $r$ . Note that I exchanged the limits of integration to get rid of the minus sign. The only thing left is to obtain  $r$  as a function of  $t$  by the standard method for separable differential equations:

$$\dot{r} = \frac{dr}{dt} = \left( 2GMe^{2\kappa r'} \int_r^{r_0} \frac{e^{-2\kappa r'}}{(a+r')^2} dr' \right)^{1/2} \quad (2.20)$$

$$\Rightarrow dt = \left( 2GMe^{2\kappa r'} \int_r^{r_0} \frac{e^{-2\kappa r'}}{(a+r')^2} dr' \right)^{-1/2} dr \quad (2.21)$$

$$\Rightarrow t = \int_{r_0}^r \left( 2GMe^{2\kappa r'} \int_{r''}^{r_0} \frac{e^{-2\kappa r'}}{(a+r')^2} dr' \right)^{-1/2} dr'' \quad (2.22)$$

$$(2.23)$$

Solving this integral (analytically or numerically) gives us the final trajectory of the gas cloud.



BCG	Temperature profile / keV
NGC 5044	$T(r) = 0.166 \left(\frac{r}{10}\right)^{-0.846} + 0.782$
NGC 1275	$T(r) = 7 \left( \frac{1+(r/100)^3}{2.3+(r/100)^3} \right)$

Table 2.1 De-projected temperature profiles for the X-ray ICM in NGC 5044 (David et al. 2017) and NGC 1275 (Churazov et al. 2003)

BCG	Density profile / cm <sup>-3</sup>
NGC 5044	$n_e(r) = 0.0314 r^{-1.80} + 0.0113 \left(\frac{r}{21.1}\right)^{-0.394} \left[1 + \left(\frac{r}{21.1}\right)^2\right]^{-0.998}$
NGC 1275	$n_e(r) = \frac{3.9 \times 10^{-2}}{(1+(r/80)^2)^{1.8}} + \frac{4.05 \times 10^{-3}}{(1+(r/280)^2)^{0.87}}$

Table 2.2 De-projected density profiles for the X-ray ICM in NGC 5044 (David et al. 2017) and NGC 1275 (Churazov et al. 2003)

### De-projected temperature, density, and pressure profiles

In the preceding calculations of gas cloud trajectories through the ICM I obtain values for the density and temperature (and hence pressure) of the ICM in NGC 5044 as functions of radius based on de-projected profiles presented in David et al. (2017). In the discussion section of the paper (2.4.5), I perform basic calculations to establish the energetic feasibility of excitation of the nebula by penetrating particles from the ICM and compare the conditions in NGC 5044 with those in NGC 1275; in order to do this, I obtained de-projected temperature and density profiles for NGC 1275 from Churazov et al. (2003). The models are reproduced in Tables 2.1 and 2.2.

I then obtain pressure profiles by simply taking the product of the temperature and density profiles.



## 2.4 Full Text of Paper

Authors: James Nianias (1), Jeremy Lim (1), and Youichi Ohyama (2)

Co-authors: Lawrence David (3), Gerrit Schellenberger (3), Jan Vritlek (3), and William Forman (3)

(1) Department of Physics, University of Hong Kong, Pokfulam Road, Hong Kong

(2) Institute of Astronomy and Astrophysics, Academia Sinica, Taipei 10617, Taiwan

(3) Center for Astrophysics, Harvard & Smithsonian, 60 Garden St., Cambridge, MA 02138, USA

### 2.4.1 INTRODUCTION

The giant elliptical galaxies at the centers of galaxy groups and clusters sometimes host luminous optical emission-line nebulae, which, when well-resolved, exhibit complex filamentary structures such as the relatively nearby examples in the NGC 5044 group (David et al. 2011, see Fig. 2.18 of this manuscript), the Centaurus cluster (Fabian et al. 2016), and the Perseus cluster (Lynds 1970; Conselice et al. 2001). In galaxy clusters, the presence of such nebulae in their central galaxies is quite exquisitely tuned to the thermal state of their intracluster X-ray emitting gas, appearing almost exclusively when the gas entropy<sup>4</sup> at the cluster core (at radii  $\lesssim 200$  kpc) lies below  $\sim 30$  keV cm<sup>2</sup> (Cavagnolo et al. 2008). This same entropy threshold governs the presence of star formation (Voit et al. 2008) and relatively luminous radio emission from active galactic nuclei (AGNs) in cluster central galaxies (Cavagnolo et al. 2008). These dependencies

---

<sup>4</sup>Gas entropy  $K$ , is computed as  $K = kT/n_e^{2/3}$ , where  $T$  is the gas temperature,  $n_e$  is the electron density, and  $k$  the Boltzmann constant.



implicate accretion of relatively cool intracluster gas for producing the luminous nebulae and fuelling both the star formation and AGNs in cluster central galaxies.

Consistent with this expectation, galaxy groups and clusters that have low gas entropies at their cores exhibit an X-ray surface brightness that is strongly centrally peaked (owing to high central gas densities, as the X-ray luminosity  $L_X \propto n_e^2 T^{1/2}$ ), indicating prodigious radiative loss at their cores. Accordingly, the same galaxy groups and clusters exhibit relatively low X-ray temperatures at their cores, and are therefore referred to as cool-core groups and clusters. Cowie & Binney (1977) and Fabian & Nulsen (1977) independently predicted that the resulting loss of pressure support in the cores of such clusters would result in an inflow of cooling intracluster gas, referred to as an X-ray cooling flow. Molendi & Pizzolato (2001) found, however, that the mass-deposition rates from any such flows are much lower than were predicted, as was demonstrated more robustly by David et al. (2001) and Peterson et al. (2003). Today, it is widely recognized that X-ray cooling flows are strongly quenched by the actions of AGNs in group or cluster central galaxies (e.g., review by Fabian 2012). Nonetheless, the presence of luminous nebulae in the central galaxies of cool-core groups and clusters (henceforth, cool-core nebulae) implies that catastrophic cooling of the intragroup or intracluster gas is not always entirely halted – thus leaving a residual cooling flow, albeit with a mass-deposition rate that has yet to be directly measured.

The complex structure and, where measured, kinematics of cool-core nebulae argue against a simple inflow of quiescent gas cooling from the intergroup or intracluster medium as the only process for producing or shaping these nebulae. Rather, the cooling and/or shaping processes likely involve a complex interplay



between mechanical actions associated with the AGN in the central galaxy and its surrounding intragroup or intracluster medium (e.g., Qiu et al. 2020), albeit in ways that remain to be fully understood. There are other hurdles that hinder our understanding of cool-core nebulae, chief amongst which is the manner by which these nebulae are energized and hence their emission lines produced. Although cool-core nebulae have been found to comprise ionized, atomic, as well as molecular gas, our poor understanding of what powers these nebulae also means that the physical properties of their different gas constituents are poorly determined – and hence also the individual constituent masses, which could otherwise provide an indirect probe of the mass-deposition rate from a residual cooling flow. Present estimates imply that the molecular component traced by the rotational lines of CO at radio wavelengths, yielding masses of up to  $\sim 10^{11} M_{\odot}$  in the central galaxies of cool-core clusters (important for assessing the amount of fuel immediately available for star formation), dominates by far the nebular mass (Edge 2001; Salomé & Combes 2003). The inferred masses are based on the conversion between CO luminosity and H<sub>2</sub> gas mass established for molecular clouds in our Galaxy, and have been questioned as physical conditions in the molecular gas of cluster central galaxies are expected to be very different than those in Galactic molecular clouds (see discussion in Lim et al. 2017).

Here, we test the different predictions of leading theoretical models proposed for energizing cool-core nebulae: specifically, those in which the energy is deposited either as heat or as energetic particles, both of which have been considered in detail by Ferland et al. (e.g., 2009). They found that the injection of pure heat into the nebular gas (e.g., heat conduction from the surrounding X-ray gas, heating by Alfvén waves propagating along magnetic fields that thread the nebular filaments) cannot explain the peculiar emission-line ratios of



ions, atoms, and H<sub>2</sub> molecules observed in optical and infrared spectra. In this model whereby thermal energy is the only source of ionization and excitation (resulting from collisions), only a single gas phase can (predominantly) exist in a given volume as temperature thresholds are crossed whereby molecular gas is dissociated into atomic gas, or atomic gas is ionized into plasma (see Ferland et al. 2009). Such a model has difficulty explaining the detection of HeI, [NeII], and [NeIII] lines yet not [OIII] lines – [NeIII] having a higher ionization potential than [OIII] – in NGC 1275, the giant elliptical galaxy at the center of the Perseus cluster. On the other hand, Ferland et al. (e.g., 2009) was able to reproduce the observed emission-line ratios in this galaxy if its nebular gas contains energetic particles (e.g., from the surrounding X-ray gas that penetrates into the nebula, as advocated by Fabian et al. 2011); such energetic particles produce, through collisional ionization, a secondary population of electrons that quickly thermalize and both heat and excite the nebular gas. In this model, by contrast with the previous model, both the molecular and atomic phases can co-exist and produce emission lines within the same volume of gas. In such gas, charge-transfer recombination (i.e.,  $X^{+n} + H^0 \rightarrow X^{+n-1} + H^+$ , where X = Ne or O) – which requires atomic hydrogen gas – is much faster for O than for Ne, thus suppressing the [OIII] line relative to the Ne[II] and Ne[III] lines. Ionic and atomic lines in the optical spectra of cool-core nebulae can therefore be produced by partially if not almost fully atomic hydrogen gas, very different to the same emission lines observed in our Galaxy that is usually produced by almost fully ionized hydrogen gas.

In this manuscript, we subject the aforementioned model predictions to the nebula in the central galaxy of the NGC 5044 group, named after its dominant central giant elliptical galaxy. No recent (over the past  $\sim$ 1 Gyr) star formation



is evident in NGC 5044, ruling out photoionization from newly-formed massive stars (or other mechanisms related to star formation, such as the injection of mechanical energy from supernova explosions) for powering its multi-phase nebula<sup>5</sup>. Irradiation from the AGN in cluster central galaxies has long been ruled out for many cool-core nebulae owing to their relatively uniform surface brightness, in contradiction with the strong radial dependence anticipated for a central energizing source. The AGN in NGC 5044 is one of the brightest sub-mm continuum sources in any BCG and has been shown to be unusual in it's strong CO(2-1) absorption features (Schellenberger et al. 2020); however, it is not a bright if detectable source at optical, UV, or X-ray wavelengths. This rules out other processes for energizing its nebula, so NGC 5044 provides a clean test of whether pure heat or energetic particles energize its nebula. In Section 2.4.2 we present details of our imaging and spectroscopic observations. In Sections 2.4.3 and 2.4.4 we present our imaging and spectroscopy results, respectively. We discuss implications of our results with respect to excitation of the nebula in 2.4.5. Like in our previous work on NGC 5044, we adopt for this galaxy a systemic velocity of  $2758 \text{ km s}^{-1}$  and a luminosity distance of 31.2 Mpc (Tonry et al. 2001), which gives a physical scale in the rest frame of NGC 5044 of  $1'' = 150\text{pc}$ .

---

<sup>5</sup>We have used archival data from the Hubble Space Telescope to search for relatively blue and hence young star clusters in NGC 5044, in much the same manner as the method used to catalog relatively blue and hence young star clusters in NGC 1275 (Lim et al. 2020). Unlike the thousands cataloged in NGC 5044 having ages up to  $\sim 1 \text{ Gyr}$ , we could not find even a single such example in NGC 5044.



## 2.4.2 OBSERVATIONS AND ARCHIVAL DATA

### Canada-France-Hawaii Telescope

We carried out imaging to map the spatial distribution of the  $2.12\text{ }\mu\text{m}$   $\text{H}_2\text{ 1-0 }S(1)$  line emission from NGC 5044 on 2013 April 21, April 30, and May 1 with the Wide-Field Infrared Camera (WIRCam) on the 3.6 m Canada-France-Hawaii Telescope (CFHT). Two filters were used: the  $2.122/0.032\text{ }\mu\text{m}$  (central wavelength/bandwidth in  $\mu\text{m}$ )  $\text{H}_2\text{ 1-0 }S(1)$  (hereafter, simply  $\text{H}_2$ ) filter for the line, and the  $2.146/0.325\text{ }\mu\text{m}$  Ks filter for the continuum. We targeted a sensitivity of  $\sim 2 \times 10^{-17}\text{ erg s}^{-1}\text{ cm}^{-2}\text{ asec}^{-2}$  at the  $\sim 3$  sigma level, corresponding to 9 hours of exposure time for the  $\text{H}_2$  filter and 3 hours for the continuum. Given a typical circum-nuclear  $\text{H}\alpha$  surface brightness of  $\sim 1 \times 10^{-15}\text{ erg s}^{-1}\text{ cm}^{-2}\text{ asec}^{-2}$  (David et al. 2011), the targeted detection threshold would make it possible to detect the  $\text{H}_2$  line at a signal-to-noise of  $\sim 5$  per pixel if the  $\text{H}_2$ -to- $\text{H}\alpha$  line ratio is  $\sim 0.05$  (i.e., similar to that found in NGC 1275 by Lim et al. (2012)). Due to poor weather, the total integration times reached were 253 minutes (47% of requested time) and 70.7 minutes (39% of requested time) for the  $\text{H}_2$  and continuum filters respectively. Pre-processing of the data was performed by CFHT using the ‘I‘iwi pipeline<sup>6</sup>. For reasons explained below, we performed two rounds of data reduction. Our initial data reduction was performed using the detrended and sky-subtracted frames produced by ‘I‘iwi. We stacked the image frames from each filter following the Canadian Astronomy Data Center’s (CADC’s) WIRwolf image stacking pipeline as an outline, making use of SExtractor (Bertin & Arnouts 1996) for source detection and SCAMP (Bertin 2006) for astrometric distortion correction and photometry. We then aligned the  $\text{H}_2$  and continuum images using SWARP (Bertin et al. 2002), followed by

---

<sup>6</sup><https://www.cfht.hawaii.edu/Instruments/Imaging/WIRCam/IiwiVersion2Doc.html>



PSF matching and a manual sub-pixel alignment using ASTROPY (Astropy Collaboration et al. 2013, 2018).

The wider K<sub>s</sub> filter used to image the continuum encompasses the entire bandpass of the narrower H<sub>2</sub> filter used for measuring the H<sub>2</sub> 1-0 *S*(1) line. To subtract the smaller relative contribution from the continuum in the H<sub>2</sub> filter compared with the K<sub>s</sub> filter, an appropriate scaling factor must be applied to the image in the wider 2.146/0.325 μm K<sub>s</sub> filter before subtracting from the image in the narrower 2.122/0.032 μm H<sub>2</sub> filter. We performed the subtraction of the K<sub>s</sub> from the H<sub>2</sub> image with a variety of scale factors as tests, with all results showing significant residuals that vary isotropically with radius from the center of the galaxy. We determined that very small offsets caused by imperfect sky subtraction could account for this effect in all but the central region of the galaxy. To remedy this, we manually added a small offset across the entire K<sub>s</sub> image until the azimuthally-averaged ratio between the H<sub>2</sub> and K<sub>s</sub> filters no longer showed a radial dependence beyond a radius of ∼ 5''.

## Very Large Telescope

### H<sub>2</sub> 1-0 *S*(1) line

To study the kinematic relationship between H<sub>2</sub> and other nebular components in different phases and/or temperatures, we searched telescope archives for spectroscopic observations of H<sub>2</sub> emission from NGC 5044. We found near-infrared spectroscopic data spanning the 2.12 μm H<sub>2</sub> line in the ESO archive. This data was taken using the ISAAC instrument (Moorwood et al. 1998) on the Very Large Telescope (VLT) on 2010 May 3 for a total integration time of 220 minutes. The observations were made using the long slit spectrograph through a slit of length 120'' and width 1'' with the medium-resolution (MR)



dispersion grating. The 1.8900 - 2.5000  $\mu\text{m}$  SK filter was used, with total wavelength coverage on the detector of 2.1261 - 2.2410  $\mu\text{m}$  and spectral resolution (FWHM) of  $\sim 0.00078 \mu\text{m}$  (or  $109 \text{ km s}^{-1}$ ) at the wavelength of the redshifted H $\alpha$  ( $\sim 2.1400 \mu\text{m}$ ). A nodding pattern with a throw of  $60''$  parallel to the slit length was used in the observations to allow A-B-B-A sky subtraction, without overlap of the nebula between the A and B positions (the nebula as imaged in H $\alpha$  extends less than  $60''$  along the slit as shown in Figure 2.18). The detector pixel scale was  $0.148''/\text{pix}$  and seeing on the night of observations was approximately  $1.6''$ .

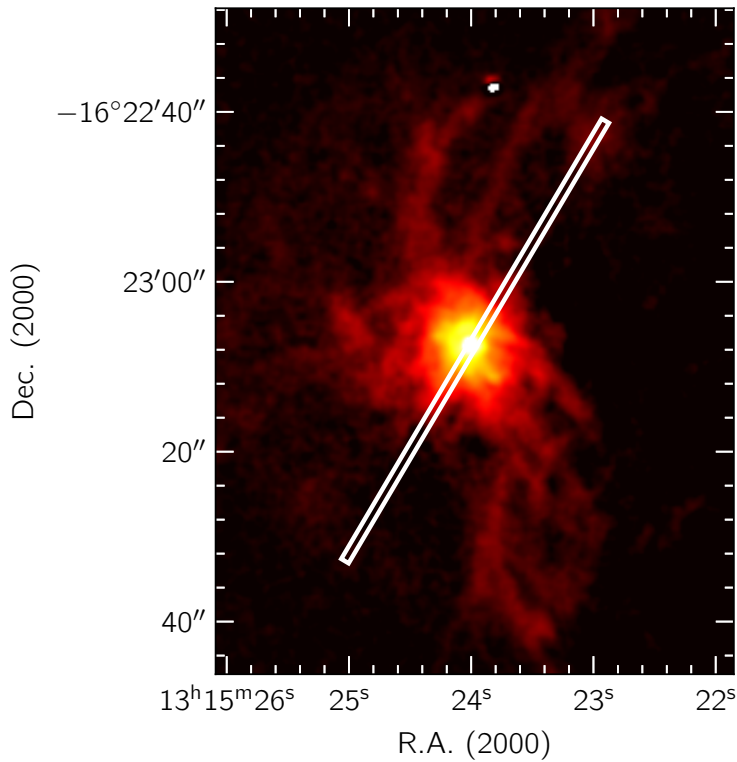


Figure 2.18 Effective ISAAC slit position after sky subtraction.

We performed bias correction, dark subtraction, flat fielding, distortion corrections, wavelength calibration, and A-B-B-A sky subtraction using the ESO ISAAC pipeline. On close inspection, we found that the point spread function

(PSF) of the ISAAC long slit spectra exhibited significant wavelength-dependent variation in full width at half maximum (FWHM), with the maximum value being  $\sim 1.92''$ . We corrected for this wavelength dependence by measuring the FWHM of the PSF at each wavelength along the dispersion axis in the spectrum of the photometric standard, and then convolving along the spatial axis with an appropriately sized Gaussian kernel to bring each FWHM to  $\sim 1.92''$ . We also smoothed the long-slit spectrum along the wavelength axis with a Gaussian kernel to bring the spectral resolution to  $117\text{ km s}^{-1}$ , so as to match the spectral resolution of the optical spectra (see below). We then resampled the data along the spatial axis and extracted spectra at 75 positions along the slit, each over an aperture of diameter  $0.8''$  ( $\sim 0.5 \times \text{FWHM}$ ). We then calibrated the extracted spectra in flux density using the spectrum of the photometric standard, which we slightly smoothed to reduce pixel-to-pixel noise while retaining telluric features. While most telluric features in the spectrum of NGC 5044 were removed by the A-B-B-A sky subtraction and flux-calibration, some residual features due to OH lines could be seen in the resulting flux-calibrated spectra, with the closest to the H<sub>2</sub> line at  $2.1505\mu\text{m}$  and  $2.1538\mu\text{m}$  as shown in Figure 2.19. Furthermore, an apparent detector defect is visible to the south-east of the nucleus between  $\sim 2.1347\mu\text{m}$  and  $\sim 2.1366\mu\text{m}$ , as well as an absorption feature adjacent to the H<sub>2</sub> line between  $\sim 2.1347\mu\text{m}$  and  $\sim 2.1387\mu\text{m}$  that we attribute to AlI absorption in stellar atmospheres (see 2.4.5). This absorption feature compromised our ability to fit accurate parameters to the H<sub>2</sub> lines in cases where the line is most strongly blueshifted. All of these spectral regions (defects, stellar absorption, and residual telluric features) were masked for the purposes of fitting the H<sub>2</sub> line profiles and continuum. A typical example of the calibrated spectra with masked wavelengths indicated is shown in 2.19.



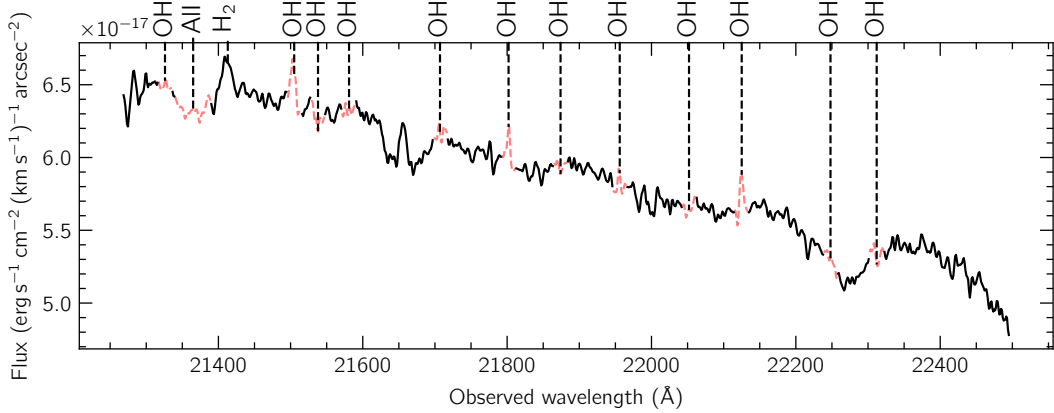


Figure 2.19 Typical calibrated NIR spectrum showing  $\text{H}_2$  line, absorption feature adjacent to  $\text{H}_2$ , and traces or residual OH lines. The red dashed line shows wavelengths masked when fitting the  $\text{H}_2$  line and/or continuum.

Measurement uncertainties in the flux-calibrated ISAAC spectra are not automatically handled by the ESO ISAAC pipeline. Instead, we estimated the uncertainty in flux density from random fluctuations in a line-free region between 2.1440 and 2.1580  $\mu\text{m}$  by fitting a second degree polynomial to this part of the spectrum and then subtracting this baseline from the data so as to remove systematic variations. Since residual fluctuations due to OH lines could still be found in the spectrum, we masked windows of 0.0021  $\mu\text{m}$  around each OH line when computing the noise.

### H $\alpha$ line

We retrieved integral field spectroscopy spanning the H $\alpha$  line as well as the adjacent [NII] lines from the ESO archive. The data was obtained using the MUSE IFU on the VLT on 2015 February 2 with a total integration time of 69 minutes. The observation spanned wavelengths from 4750  $\text{\AA}$  to 9350  $\text{\AA}$  with a spectral resolution of  $\sim 2.6 \text{\AA}$  ( $117 \text{ km s}^{-1}$ ) at the central wavelength, thus clearly separating the H $\alpha$  and [NII] lines at all positions except the nucleus, where

Doppler broadening is significantly stronger than elsewhere. The instrumental scale was  $0.2''/\text{spaxel}$  and the seeing was approximately  $0.6''$ , with a field size of  $60'' \times 60''$ , thus spanning the full length of the slit used in the NIR observations of the H<sub>2</sub> line (see Section 2.4.2). Pre-processing including bias subtraction, dark subtraction, flat fielding, and wavelength calibration, as well as photometric calibration, was carried out automatically at ESO using the MUSE 1.6.1 ESO pipeline (Weilbacher et al. 2020).

In order to make a one-to-one comparison between the H $\alpha$  spectra taken with MUSE and the H<sub>2</sub> 1-0  $S(1)$  spectra taken with ISAAC, we extracted a simulated long-slit spectrum from the MUSE data cube using the QFITSVIEW software package (Ott 2012). The slit position and orientation was chosen to match that of the ISAAC data: the slit was centered on the brightest pixel in the image (presumably marking the location of the AGN) along a position angle of  $30.4^\circ$ . Prior to extracting the simulated longslit spectrum, we convolved the data cube along the spatial axes with a Gaussian kernel to match the angular resolution of the ISAAC observations. From the resulting 2D spectrum, we extracted spectra at positions along the slit matching as closely as possible the spatial locations of the spectra extracted from the ISAAC data: 75 spectra were extracted from apertures of width  $0.8''$  along the length of the slit, with the central aperture centered on the peak continuum brightness of NGC 5044. 1-sigma errors in the optical spectra were extracted from the variance map produced by QFITSVIEW from the MUSE variance data cube.

The optical spectra from MUSE also revealed H $\alpha$  absorption, presumably of stellar origin, as shown in Figure 2.20. This absorption is most clearly visible in the spectra from parts of the nebula with weaker H $\alpha$  + [NII] emission as well as off-nebula spectra, but is presumed to extend throughout the inner nebula as



well. The absorption was corrected for by finding the average equivalent width, central velocity, and velocity dispersion of the absorption feature in spectra from positions along the slit showing no significant H $\alpha$  + [NII] emission. A Gaussian of appropriate amplitude, width, and central velocity was then added on to each emission spectrum to correct for the absorption. Although this method did not take into account kinematical variation in the stellar continuum (if any) along the slit. Visual inspection of the resulting spectra show a marked improvement in the baselines around the H $\alpha$  emission lines.

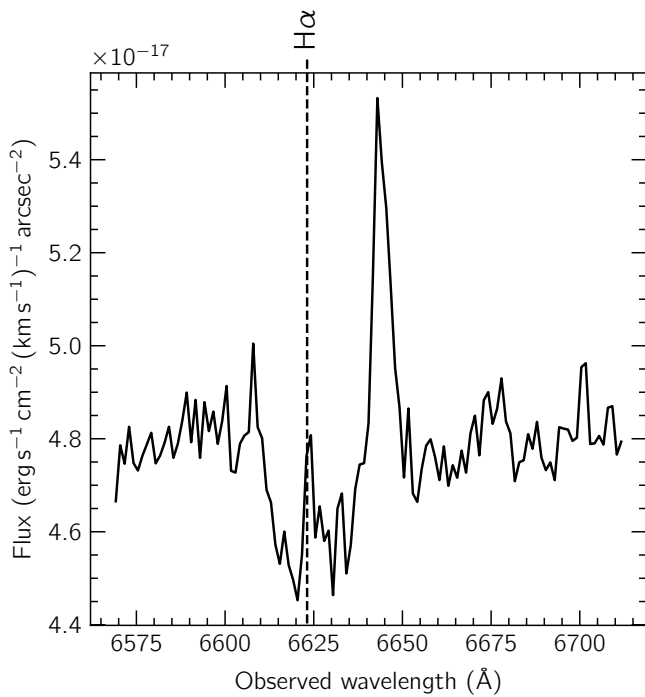


Figure 2.20 Optical spectrum extracted from MUSE data cube showing (photospheric) absorption and (nebular) emission in H $\alpha$ , taken from a slit position 12'' south-east of the nucleus.

### ALMA observations of CO(2–1) 1.3mm line

We conducted two separate ALMA + ACA observations of the CO(2–1) 1.3mm line from NGC 5044: the first used ALMA in cycle 0 with the full 12 m



array (taken on 2012 January 13), while the second used ACA during cycle 4 with the 7 m array (taken on 2017 July 13). The total on-source integration times for the ALMA and ACA observations were 29 minutes and 306 minutes respectively, while the primary beam sizes were  $27''$  and  $42''$  respectively. Thus the bright inner region of the nebula was covered but not the outermost filaments (see Figure 2.18). Further details of the ALMA and ACA observations can be found in David et al. (2014) and Schellenberger et al. (2020) respectively. The data were processed in CASA and combined to form image cubes with a spectral resolution of  $\sim 10 \text{ km s}^{-1}$  and a synthesized beam of  $\sim 2.3'' \times 1.5''$  at a position angle of  $\sim 30^\circ$ . Similarly to the H $\alpha$  data reduction outlined above, we then used QFITSVIEW to simulate long-slit spectroscopy from the data cube, with slit position and dimensions chosen to match the ISAAC observations of the H $_2$  2.12  $\mu\text{m}$  line as closely as possible: the simulated slit was centered on the AGN with a position angle of  $30.4^\circ$  and a width of  $1.2''$  (slightly wider than the  $1''$  of the ISAAC slit). We then extracted 57 spectra from apertures of width  $0.8''$  along the slit (there are fewer spectra as the primary beams do not cover the entire length of the ISAAC slit). Due to the limited velocity range of the spectra, we were unable to smooth to match the resolution of the H $\alpha$  and H $_2$ . Instead, we simply smoothed the spectra along the frequency axis with a Gaussian kernel of width 3 channels to reduce noise.

### 2.4.3 IMAGING RESULTS

#### H $_2$ 1-0 S(1) surface brightness

The H $_2$  narrow-band image, after removing the stellar continuum in the manner described in Section 2.4.2, showed no detectable line emission. At the same time, however, the continuum-subtracted image exhibited clear artifacts



in the form of two vertical lines to the east and west of the center of NGC 5044, along with other less bright but nonetheless troubling fluctuations in the background level. We determined that these artifacts were produced as a result of the automatic sky subtraction method used in the ‘I’iwi pipeline for WIRCam images. For each WIRCam observation, the ‘I’iwi pipeline produces two sets of images: the p-frames which are de-trended and automatically sky subtracted, and the s-frames which are de-trended but not sky subtracted. To address the issue of artifacts arising from the automatic sky subtraction in the p-frames, we developed our own sky subtraction method which we applied to the s-frames. This sky subtraction was found to work effectively on  $\sim 40\%$  of the images in the data set, yielding a residual continuum-subtracted image with a flat background. However, despite the improved quality of the resulting continuum-subtracted image as shown in Figure 2.21, still no H<sub>2</sub> emission is detectable.

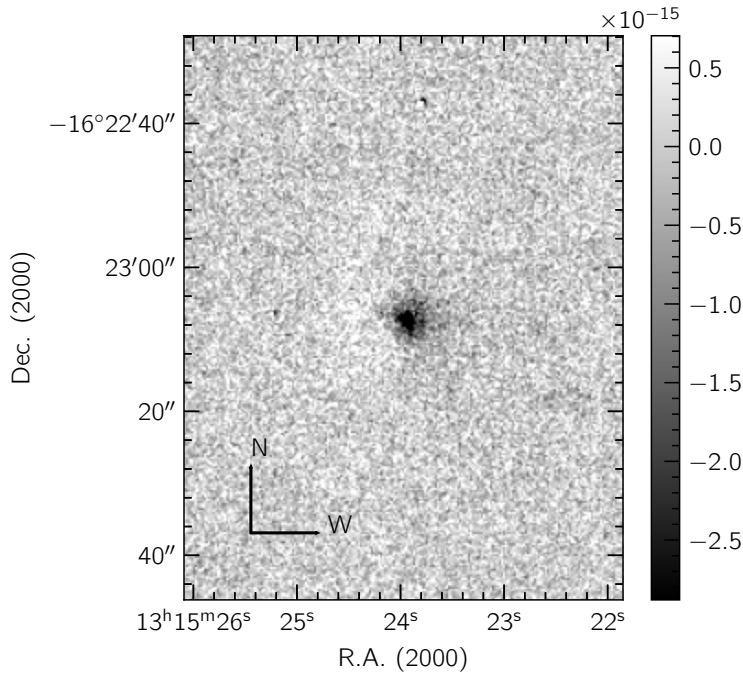


Figure 2.21 Continuum-subtracted H<sub>2</sub> narrowband image using our custom sky-subtraction strategy. Units are erg s<sup>-1</sup> cm<sup>-2</sup> arcsec<sup>-1</sup>.

Although failing to detect H<sub>2</sub>, the image constructed provides a useful upper bound of the line surface brightness at 2.122μm. We calculated the RMS noise per pixel across regions with known H $\alpha$  emission based on the narrowband H $\alpha$  image reported in David et al. (2011), excluding the innermost part of the nebula owing to the negative residual feature around the nucleus mentioned earlier in Section 2.4.2. In this way, we found the RMS noise per pixel to be  $\sim 7 \times 10^{-16}$  erg s $^{-1}$  cm $^{-2}$  asec $^{-2}$ . Given that the surface brightness of the H $\alpha$ +[NII] <  $1 \times 10^{-15}$  erg s $^{-1}$  cm $^{-2}$  asec $^{-2}$  in the outer filaments, this implies an upper bound for the H<sub>2</sub>/H $\alpha$ +[NII] ratio is  $\sim 1$ . As a sanity check on these results, we compared them with our spectroscopy results as outlined in Section 2.4.4, which reveal a maximum H<sub>2</sub> surface brightness of  $\sim 4 \times 10^{-16}$  erg s $^{-1}$  cm $^{-2}$  asec $^{-2}$  within the central 2'' of the nebula, which, as noted discussed below, is affected by an apparent color change leading to a negative residual in this region. Regardless of the presence of the negative residual around the nucleus, this puts the maximum possible signal-to-noise per pixel at just  $\sim 0.6$ . Moving away from the nucleus towards the outer filaments, the H<sub>2</sub> surface brightness drops by over an order of magnitude to just  $\sim 1 \times 10^{-17}$  erg s $^{-1}$  cm $^{-2}$  asec $^{-2}$ , suggesting a signal-to-noise per pixel in the outer filaments of just  $\sim 0.01$ .

### Circum-nuclear Color Change

Despite refining our data reduction to remove artifacts in the background and radial dependence in the Ks-to-H2 ratio (H2 referring to the narrowband filter, not actual H<sub>2</sub> line emission), our results reveal a persistent negative residual at the center of NGC 5044 as shown in Figure 2.21. The over-subtraction created in the narrowband H<sub>2</sub> image in the innermost region of NGC 5044 after optimizing

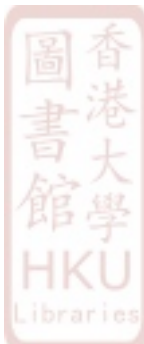


the stellar continuum subtraction for the regions beyond suggest a real change in the Ks-to-H<sub>2</sub> ratio. We confirmed such a change by making a ratio of the H<sub>2</sub> narrow-band and Ks continuum images, which showed a higher Ks-to-H<sub>2</sub> ratio around the nucleus compared with the rest of NGC 5044. We discuss possible origins of this feature in Section 2.4.5.

#### 2.4.4 SPECTROSCOPY RESULTS

##### Kinematics

Figure 2.22 shows spectra in H $\alpha$ , H<sub>2</sub>, and CO for nine selected regions that illustrate the range of spectra observed. As can be seen, especially in H $\alpha$  and H<sub>2</sub> (both of which were observed at a much lower spectral resolution than CO), the spectra can be well characterized by a single Gaussian (as in positions  $-6.4''$  and  $+4.8''$ ) or, more frequently, two sometimes overlapping Gaussian components (in the remaining panels), suggesting multiple velocity components associated with overlapping filaments along the same sightline. The spectra show gradual changes in spectral profiles along the length of the slit, with redshifted components present to the south-east of the AGN (positions  $< 0''$ ) and blueshifted components to the north-west. In cases where more than one Gaussian component can be discerned, there are also some more heavily blueshifted components ( $-400 \lesssim v \lesssim -200$ ) within the central  $\sim 1\text{kpc}$  as can be seen in positions  $-4.0''$ ,  $-3.2''$ ,  $-2.4''$ ,  $+1.6''$ ,  $+2.4''$ , and  $+3.2''$  in Figure 2.22. Some of the most heavily blueshifted components in the H<sub>2</sub> spectra overlap with an adjacent stellar absorption feature as can be seen in positions  $+1.6''$ ,  $+2.4''$ , and  $+3.2''$  in Figure 2.22. In each of these H<sub>2</sub> spectra, a second less heavily blueshifted Gaussian component can be seen, which appears to be shifted to a lower velocity by the absorption feature.



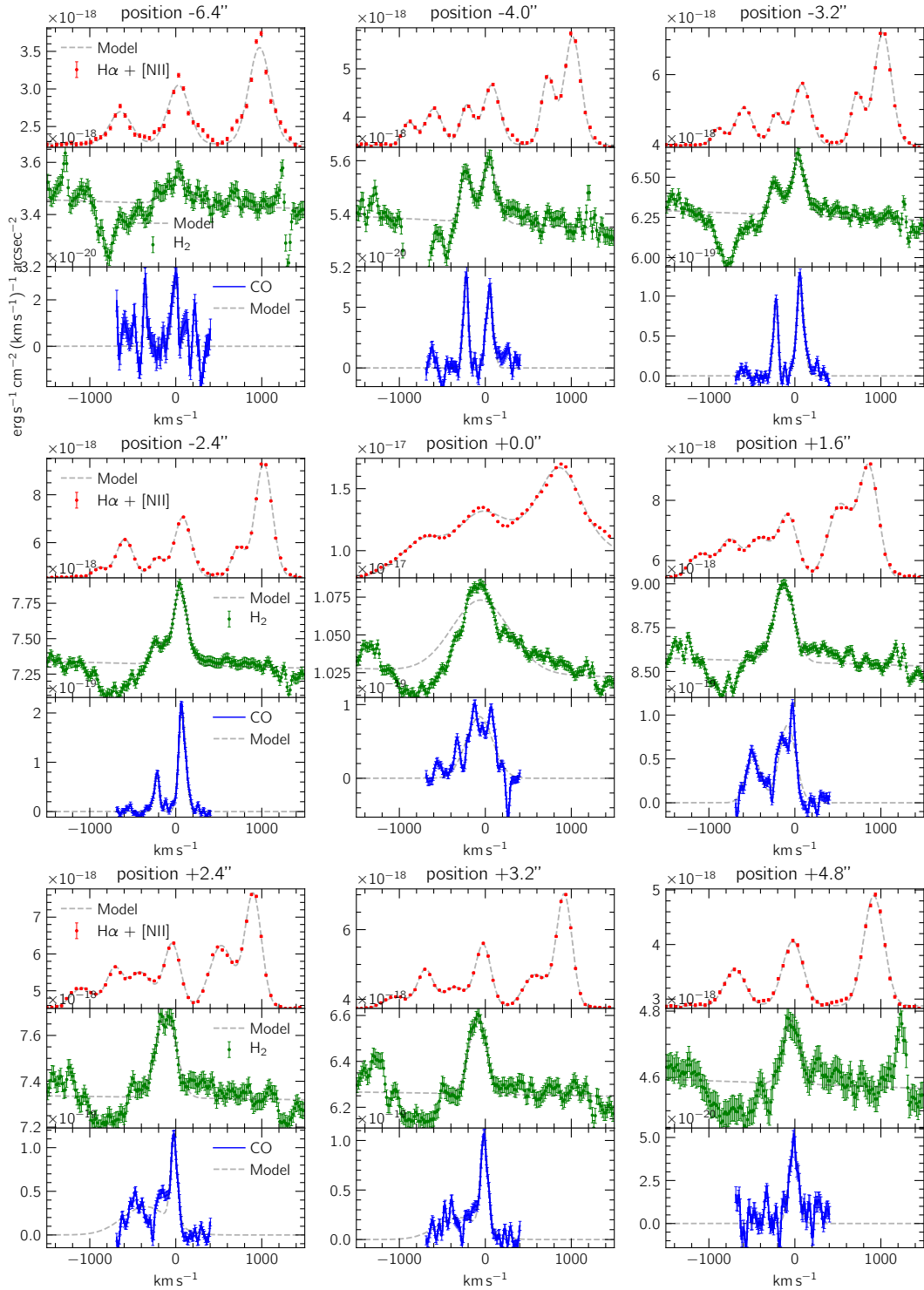


Figure 2.22 Extracted H $\alpha$ , H $_2$ , and CO spectra arranged according to position along the slit.

We therefore fitted Gaussian profiles to the spectral lines in the extracted H<sub>2</sub>, H $\alpha$  + [NII], and CO spectra (along with linear baselines for the H $\alpha$  and H<sub>2</sub> spectra). We used SciPY’s CURVE\_FIT method to perform the fitting, which employs the Levenberg-Marquardt algorithm (Virtanen et al. 2020). In positions where all three lines (H $\alpha$ , H<sub>2</sub>, and CO) were detected, two Gaussian components were fitted to the H $\alpha$  spectra in 10 out of 16 cases and to the CO in 11 out of 16 cases, since the line profiles are clearly double-peaked. On the other hand, double-peaked profiles were only fitted to about half of H<sub>2</sub> spectra (with the remainder being fitted with single peaks) due to one peak being close to if not in the adjacent absorption trough as can be seen in positions +1.6'', +2.4'', and +3.2'' in Figure 2.22. Single-peaked fitted line profiles can be seen in positions −6.4'' (H $\alpha$  and H<sub>2</sub>) and +4.8'' (all lines) in Figure 2.22, while double-peaked profiles are fitted to all three lines in positions −4.0'', −3.2'', and −2.4''. When fitting the H $\alpha$  + [NII] lines, we fit the same line center and width to all three lines (H $\alpha$  and the [NII] doublet), and the amplitude of the 6548 Å [NII] line was fixed at  $\sim 1/3$  that of the 6583 Å [NII] line (reflecting the statistical weighting of the transitions between the energy levels in the [NII] doublet). Fitting the H $\alpha$  and [NII] lines simultaneously better constrains the central velocities and velocity dispersions compared to fitting the individual lines separately. We also applied a barycentric correction to the H<sub>2</sub> line central velocities since the CO and H $\alpha$  velocities were already in the heliocentric system. 1-sigma uncertainties for the fitted parameters were generated using the diagonal elements of the covariance matrix produced by the fitter. In the case of the H<sub>2</sub> and H $\alpha$  spectra, we summed these uncertainties in quadrature with the systematic errors in the velocity coordinates to obtain the total uncertainty (this step was not necessary for the CO spectra due to the negligible velocity



uncertainties in ALMA spectra). Furthermore, we recomputed the velocity dispersions of all lines taking into account the instrumental dispersions, which were  $117\text{km s}^{-1}$  for H $\alpha$  (original resolution),  $117\text{km s}^{-1}$  H $_2$  (after convolution, originally  $109\text{km s}^{-1}$ ), and  $32\text{km s}^{-1}$  for CO (originally  $10\text{km s}^{-1}$ ).

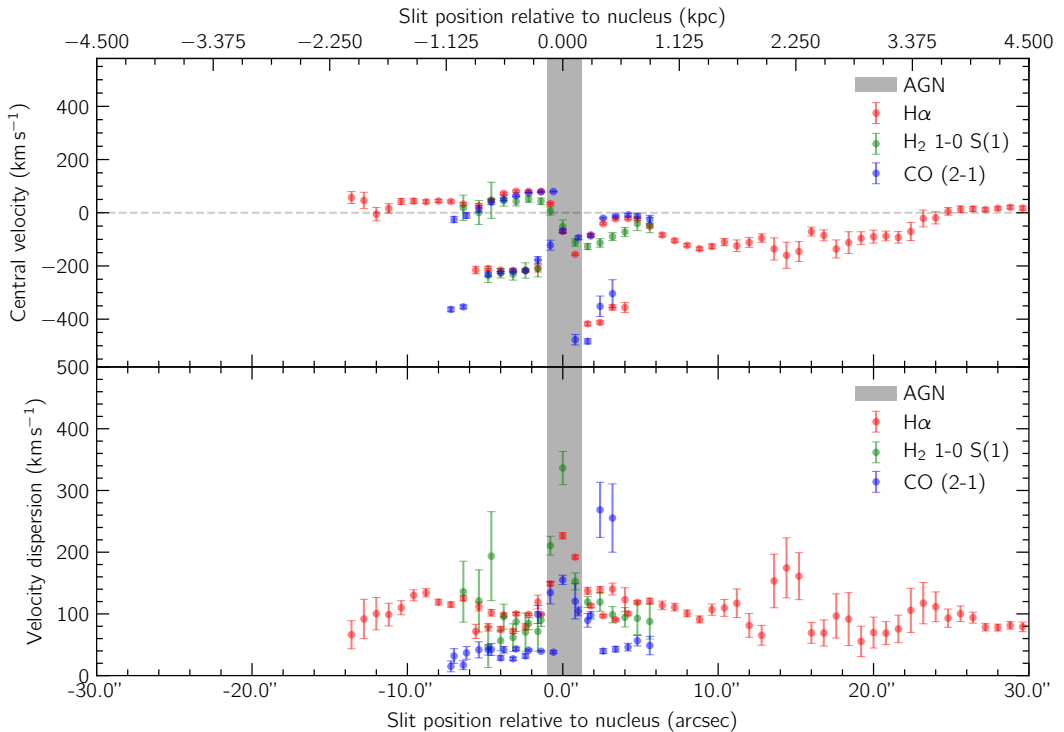


Figure 2.23 Central velocities (top panel) and velocity dispersions (bottom panel) of the line profiles fitted to the H $\alpha$ , H $_2$ , and CO spectra plotted against position along the slit. The triangular markers in the bottom panel indicate the fitted lines where the velocity dispersion was below that of the observations. In these cases, the values have not been corrected for instrumental dispersion. We attribute this issue to fluctuations in the spectral baselines distorting the lines.

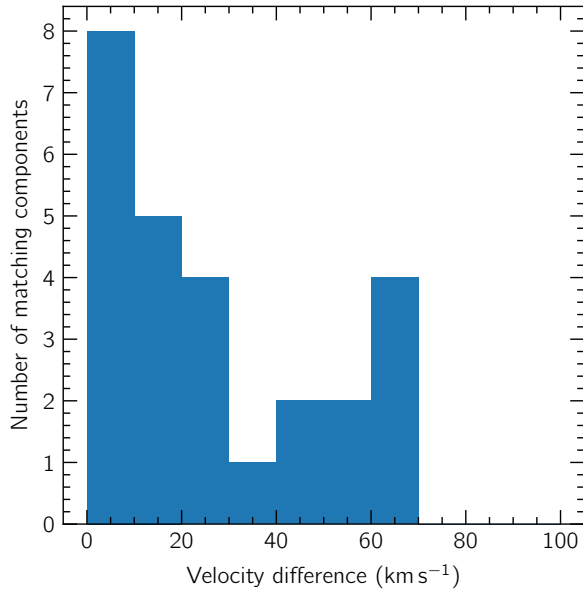


Figure 2.24 Histogram of central velocity differences between matched CO and H $\alpha$  lines

Comparisons of the central velocities of the fitted Gaussians to the H $\alpha$ , H<sub>2</sub>, and CO spectra are shown in the upper panel of Figure 2.23. These results agree with the impression given by the spectra in Figure 2.22 of a dynamically ordered inner region, with multi-component line profiles changing gradually, shifting by  $\sim 200\text{km s}^{-1}$  towards lower velocities from the south-east to the north-west side of the AGN. The central velocities of the H $\alpha$ , H<sub>2</sub> and CO profiles show remarkable coherence at the common spatial resolution of  $\sim 290\text{pc}$  imposed on our measurements (corresponding to approximately the size of the largest molecular clouds in our own Galaxy). Not only are the central velocities of the three gas components closely comparable if not identical within measurement uncertainties (see the more strict quantitative comparison below), but also their central velocities change in the same manner with radius; in addition, all three species closely follow each other in terms of the number of velocity components

at each position.

As can be seen in the spectra in Figure 2.22, the velocity dispersions of the H $\alpha$  and H<sub>2</sub> line profiles show close visual agreement. This is confirmed in the bottom panel of Figure 2.23, where the velocity dispersions of the H<sub>2</sub> and H $\alpha$  lines show a reasonably good general agreement. On the other hand, the CO velocity dispersions appear to be generally lower than that of H $\alpha$  and H<sub>2</sub>.

Here, we quantify the similarities and differences between the kinematics of the H $\alpha$ , H<sub>2</sub> and CO gas components. We quantify the significance level of the difference between two fitted line profiles with central velocities  $v_A \pm \sigma_{v_A}$  and  $v_B \pm \sigma_{v_B}$  in terms of

$$\alpha \equiv \frac{|v_A - v_B|}{\sqrt{\sigma_{v_A}^2 + \sigma_{v_B}^2}}$$

We start by comparing the CO and H<sub>2</sub> line profiles: since both trace molecular gas, it is conceivable that their kinematics would follow each other closely. Excluding the highly complex line profiles around the AGN, we find that just over half of cases (11 out of 18) agree in central velocity to within  $\alpha < 3$ . Among the cases with statistically significant differences in central velocities ( $\alpha > 3$ ), the median difference is 40 km s<sup>-1</sup> (7.9 sigma), while the range is 22 – 93 km s<sup>-1</sup> (3.6 – 15.2 sigma). The (unweighted) average ratio ( $\pm$  standard deviation) between the matched CO and H<sub>2</sub> lines' velocity dispersions is  $0.54 \pm 0.26$ . Confining our attention to matches with  $\alpha < 3$  only, this ratio is  $0.56 \pm 0.31$ .

Next, we compare the H<sub>2</sub> and CO line profiles with those of H $\alpha$ . Again excluding the AGN, we find that in approximately two thirds of cases, the H<sub>2</sub> line profiles' central velocities agree to within  $\alpha < 3$  with those of H $\alpha$  (10 out of 18 cases). By contrast, the CO velocities agree with those of H $\alpha$  to within  $\alpha < 3$  in just 7 out of 23 cases. At first glance, this seems to contradict the visual impression given by Figure 2.23, where CO (in blue) and H $\alpha$  (in red) track



one another more closely than H<sub>2</sub> (in green); however, due to the much higher signal-to-noise of the H $\alpha$  and CO spectra relative to the H<sub>2</sub>, the uncertainties in the fitted parameters are accordingly much smaller, and hence the values of  $\alpha$  tend to be larger between CO and H $\alpha$  components (we discuss this issue in more detail below). Among the cases with statistically significant differences in central velocities ( $\alpha > 3$ ), the median differences are 41km s<sup>-1</sup> (7.3 sigma) between H<sub>2</sub> and H $\alpha$ , and 22km s<sup>-1</sup> (5.2 sigma) between CO and H $\alpha$ , while the respective ranges are 28 – 72km s<sup>-1</sup> (3.8 – 11.5 sigma) and 6 – 68km s<sup>-1</sup> (3.2 – 15.5 sigma). Comparing the CO and H<sub>2</sub> velocity dispersions with those of H $\alpha$ , we find the (unweighted) average ( $\pm$  standard deviation) ratio between H<sub>2</sub> and H $\alpha$  velocity dispersions to be  $0.95 \pm 0.28$ , while the value for CO and H $\alpha$  is  $0.62 \pm 0.44$ . When we confine our attention to just those components that are strongly matched ( $\alpha < 3$ ), we obtain  $0.93 \pm 0.36$  for H<sub>2</sub> and H $\alpha$ , and  $0.67 \pm 0.50$  for CO and H $\alpha$ . Thus we find the velocity dispersions of the H<sub>2</sub> and H $\alpha$  components to be broadly consistent, while the CO lines tend to be narrower than their H<sub>2</sub> and H $\alpha$  counterparts. Olivares et al. (2019) similarly reports lower CO velocity dispersions relative to H $\alpha$  (H $\alpha$  linewidths being  $\sim 2$  times CO), attributing this to a larger number of warm ionized (H $\alpha$ -emitting) gas clouds along a sight line compared to cold (CO-emitting) ones. However, it is not clear whether this explanation can account for the extremely close match between the H<sub>2</sub> and H $\alpha$  linewidths. Furthermore, as we discuss later in 2.4.5, the idea that the H $\alpha$  and CO lines originate from distinct gas clouds at different temperatures is inconsistent with their close kinematic coupling.

First, to check why some of the spectra show small disagreements in their central velocities between different lines, we inspected the spectra from positions in which our fitting procedure reported significant ( $\alpha > 3$ ) differences in central



velocities between gas components. In most cases, we discovered a number of mitigating factors that cause high values of  $\alpha$  between line components that bear clear visual similarity to one another. Firstly, we note that the H<sub>2</sub> spectra are affected by the aforementioned stellar absorption feature adjacent to the H<sub>2</sub> line, and in several cases fully overlapping the more blueshifted velocity components as can clearly be seen in positions +1.6'', +2.4'', +3.2'', and +4.8'' in Figure 2.22. Furthermore, in positions where the highly blueshifted components overlap with the absorption feature, it appears that the second H<sub>2</sub> velocity component is shifted to lower values. This effect appears to be the cause of the large systematic negative offsets between the H<sub>2</sub> and CO/H $\alpha$  central velocities in the positions between +1.6'' and +4.0'' in Figure 2.23 (of which the spectrum in position +2.4'' is the most extreme example). These large offsets are otherwise puzzling given the close correspondence between the CO (molecular) and H $\alpha$  (atomic/ionized) gas components at these positions.

The largest proportion of statistically significant discrepancies in central velocities are between the CO and H $\alpha$  phases, with 16 out of 23 cases having  $\alpha > 3$ . As can be seen in Figure 2.23, the uncertainties in the fitted central velocities of the CO and H $\alpha$  lines are generally very small due to the high signal-to-noise of these observations compared to the H<sub>2</sub> spectra, thus leading to large values of  $\alpha$ . Indeed, visual inspection of the spectra cast doubt on whether the uncertainties can really be that small. In addition, the spectral resolution of the CO is far higher than that of the H $\alpha$ , which in some cases leads to non-Gaussian, asymmetrical line profiles in the CO spectra which make a comparison with the smoother H $\alpha$  spectra problematic. Examples of this are shown in the redder lines (around  $v = 0$ ) in positions +1.6'', +2.4'', and +3.2'' in Figure 2.22, and can also be seen in spectra in position +4.0''. Out the 4 redder lines seen in



CO in these positions, in only one case does it match its H $\alpha$  counterpart with  $\alpha < 3$ , despite all having clearly similar central velocities.

Another issue is that the uncertainties reported by CURVE\_FIT are extremely small, with values of  $< 1\text{km s}^{-1}$  in some of the high signal-to-noise CO spectra, and  $< 2\text{km s}^{-1}$  in some high signal-to-noise H $\alpha$  spectra. As a result, we are concerned that these uncertainties may be significantly underestimated. It should be noted that the uncertainties reported do not take into account noise correlation in the spectra or possible correlations between the fitted parameters. We also considered the possibility that overlapping between the H $\alpha$  and adjacent [NII] lines due to Doppler broadening may cause inaccuracy in the fitted H $\alpha$  line profiles. However, we do not consider this to be a significant factor contributing to high values of  $\alpha$ , since 1) the lines are well-separated enough that the peaks are clearly identifiable, and 2) fitted parameters have higher uncertainties in cases where the lines overlap significantly.

In addition to the above issues, there is also the inherently difficult issue of accounting for any remaining systematic uncertainties. One potential uncertainty arises from the possibility of pointing offsets between the observations: given the extremely small uncertainties in the fitted CO and H $\alpha$  central velocities, even a small pointing offset could potentially lead to a significant mismatch between the components. Adding to this, the CO spectra are extracted over a simulated slit with width  $1.2''$  while the H $\alpha$  and H $_2$  are extracted over slits of width  $1''$ , which may also have a significant, though small, impact on the fitted parameters.

Even if measurement uncertainties were negligible, differences between the spectral profiles from different gas phases are possible due to variations in the line ratio over the line profiles. The widths of the emission lines are almost



certainly dominated not by thermal motion, but rather by turbulent motion of the gas along a given sightline. We have shown that the line ratios fluctuate from one position to the next (see Figure 2.26). Therefore, it seems likely that, even within a given emission line, the line ratios may also fluctuate. This would tend to cause differences in the observed line profiles even if all the gas along the sightline is emitting in H $\alpha$ , H<sub>2</sub>, and CO.

Of all the fitted line profiles, the most compelling candidate for a genuine difference in central velocities based on a visual inspection is between the heavily blueshifted H $\alpha$  and CO components in position +1.6'', shown in Figure 2.22. In this case,  $\alpha = 15.5$ , with the central velocity of the CO line being  $66\text{km s}^{-1}$  lower than that of the H $\alpha$ . Although this is a significant difference, the spectral profiles nonetheless show fundamental visual similarity: a heavily blueshifted component and another component just below  $v = 0$ . After inspecting the full set of results, we find no compelling examples of in which the spectral profiles of any two gas components are unmistakably different. Considering the mitigating factors in matching the spectral profiles here mentioned, we therefore find excellent overall kinematical agreement between the gas components.

For the spectra extracted from apertures covering the PSF of the AGN, the more complex kinematics makes determining an analytical model of the line profile difficult. This is especially true when comparing either H<sub>2</sub> or CO with H $\alpha$ , since the H $\alpha$  line becomes heavily blended with the adjacent [NII] lines due to strong Doppler broadening around the AGN (see position 0.0'', the middle panel in Figure 2.22). Nevertheless, the three gas components share key commonalities in the line profiles around the AGN: all three lines peak at  $v < 0$  and extend well beyond  $v = 0$ .

An overlay of the ISAAC slit position with the H $\alpha$  map of David et al.



(2009), as shown in Figure 2.18, reveals a bright H $\alpha$  knot at the far north-west end of the slit. We extracted optical and NIR spectra from 0.8'' apertures along the slit covering this region and fitted them with Gaussians plus linear functions in the same manner as described above (our ALMA observations did not cover this region, so the same could not be done for the CO line). However, the signal-to-noise of all lines fitted in this way was below 3. Therefore, additional H $\alpha$  and H<sub>2</sub> spectra were extracted from the NW knot with larger aperture widths of 3.0'' (see Figure 2.25). The central velocities of the H<sub>2</sub> and H $\alpha$  lines are a close match ( $\alpha = 2.2$ ), while the ratio of the velocity dispersion of the H<sub>2</sub> line to that of H $\alpha$  is  $\sim 0.5 \pm 0.66$  (3 sigma).

### Line Ratios

Based on the fitted multi-component line profiles, we obtained H<sub>2</sub> to H $\alpha$ , H $\alpha$  to CO, and H<sub>2</sub> to CO flux ratios along the slit. We generated these ratios at a given position by taking the quotient of the integrated flux under the fitted Gaussians. For spectra where more than one Gaussian component could be resolved in any combination of H<sub>2</sub>, H $\alpha$  or CO, our procedure automatically took flux ratios of lines that were closest to each other in central velocity. For instance, if there are two H $\alpha$  lines and two H<sub>2</sub> lines at a given slit position, two ratios were produced: first, the H<sub>2</sub> and H $\alpha$  lines with the closest central velocities were matched, followed by the remaining lines. An identical procedure was followed for CO to H<sub>2</sub> and CO to H $\alpha$ . The ratios derived in this way and their associated  $\alpha$  values are shown in Figure 2.26.



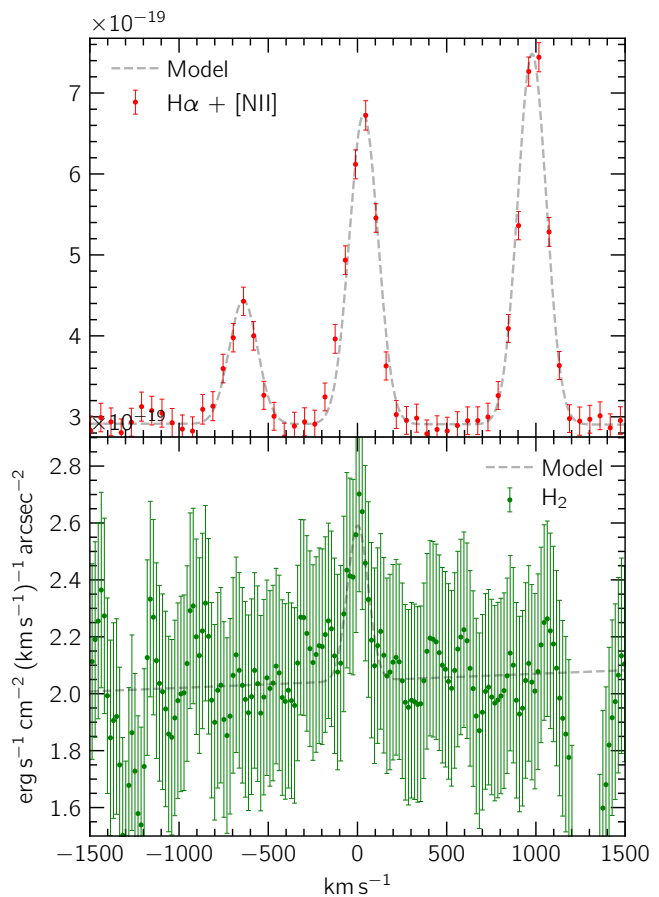


Figure 2.25  $\text{H}\alpha$  and  $\text{H}_2$  emission from the NW knot at the far end of the slit. The aperture size for these spectra was increased from  $0.8''$  to  $3.0''$  to increase signal-to-noise.



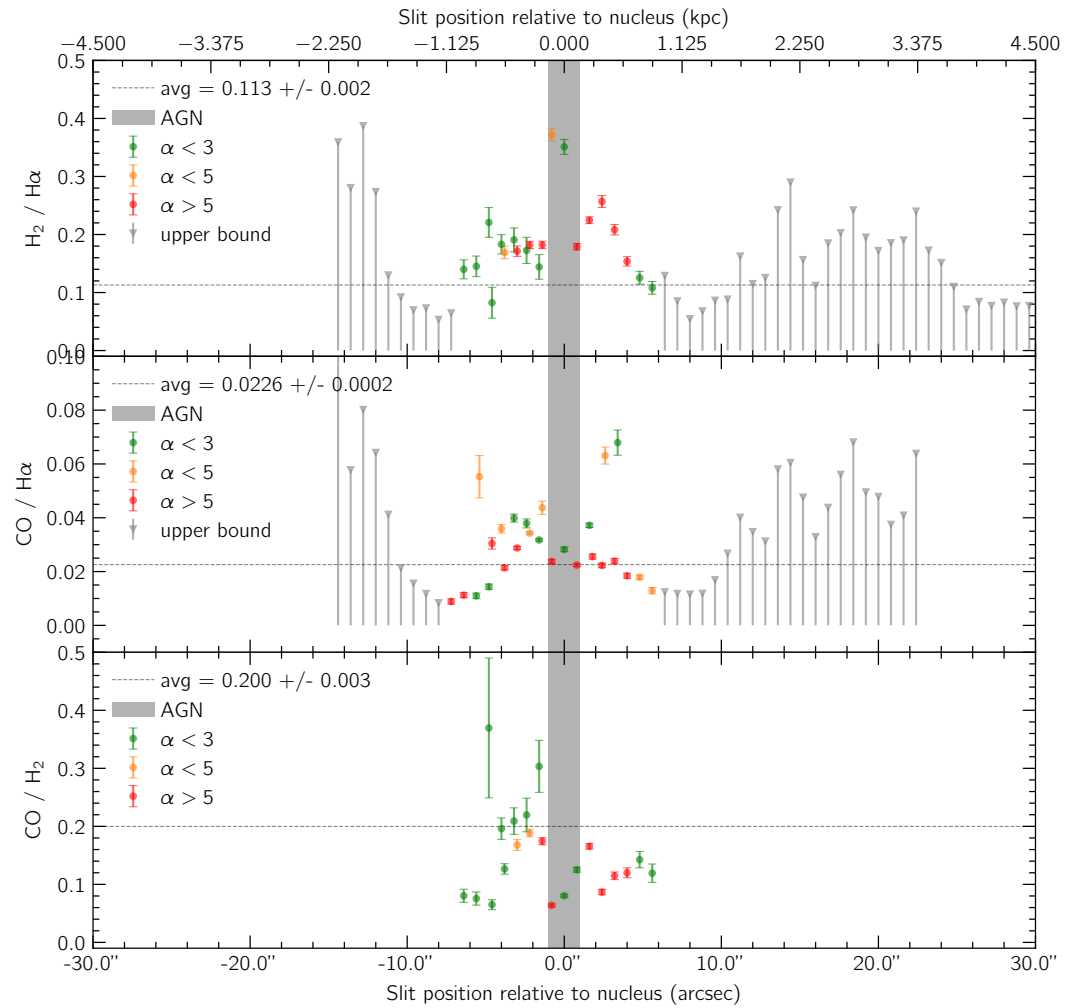


Figure 2.26 Line ratios vs slit position. Triangular grey markers indicate where the S/N of  $H_2$  or CO falls below S/N = 3 and are upper bounds only based on the 3 sigma RMS noise level in the data.

As shown in Figure 2.26, the H<sub>2</sub>-to-H $\alpha$  surface brightness ratio is fairly consistent along the slit, although the ratio appears to decrease slightly with increasing radius within the inner  $\sim 10''$  of the nebula (corresponding to a bright circum-nuclear region appearing roughly circular in projection; see Figure 2.18). That the H<sub>2</sub>-to-H $\alpha$  ratio is approximately constant throughout the nebula is supported by the similarity of the ratio in the NW knot ( $0.10 \pm 0.04$ ) to that in the inner nebula (flux-weighted average of 0.11 with standard deviation 0.04, ignoring the AGN). This agrees with the findings in NGC 1275 presented in Lim et al. (2012), in which the H<sub>2</sub>-to-H $\alpha$  ratio is also roughly constant throughout the nebular filaments. Therefore, we adopt a canonical H<sub>2</sub>-to-H $\alpha$  ratio of 0.11 throughout the nebula for the remainder of this paper. In the case of CO-to-H $\alpha$ , there is a systematic trend towards lower line ratios with increasing radius. On the other hand, the CO-to-H<sub>2</sub> ratio does not show any clear radial dependence due to substantially lower signal-to-noise. As indicated in Figure 2.26, H<sub>2</sub> and CO emission falls below 3 sigma outside of the brighter regions of the nebula, though a diffuse H $\alpha$  emission is still very clearly detected in these positions (most notably in the regions between the inner nebula and the NW knot). However, the estimated upper bounds for H<sub>2</sub> and CO surface brightness in these positions are still generally consistent with the H<sub>2</sub>-to-H $\alpha$  and CO-to-H $\alpha$  ratios found in the inner nebula (and NW knot in the case of H<sub>2</sub>).

With the exception of the NW knot, the signal-to-noise was too poor to obtain Gaussian fits to the H<sub>2</sub> line outside of the inner nebula, although H $\alpha$  + [NII] lines were fitted in the same manner as above. Therefore the ratios at these locations represent upper bounds only, with the upper bound of the H<sub>2</sub> surface brightness calculated as  $3\sqrt{2\pi}A_{rms}\Delta v_{H\alpha}$ , where  $A_{rms}$  is the local RMS deviation of the spectrum from the linear baseline around the H<sub>2</sub> line, and  $\Delta v_{H\alpha}$



is the width of the H $\alpha$  line from the same position along the slit. Similarly, no meaningful Gaussian fits were obtained for the CO spectra away from the inner nebula, and we estimated an upper bound for the CO to H $\alpha$  ratio in the same manner.

Irrespective of kinematic similarity, the flux-weighted average line ratios (excluding the apertures covering the AGN) are found to be  $\sim 0.11$  for H<sub>2</sub> to H $\alpha$ ,  $\sim 0.023$  for CO to H $\alpha$ , and  $\sim 0.20$  for CO to H<sub>2</sub>, with standard deviations along the slit of 0.04, 0.02, and 0.08 respectively.

Finally, we find the H<sub>2</sub> to H $\alpha$  line ratio in the NW knot at the far end of the ISAAC slit to be  $0.10 \pm 0.04$ . We emphasize the importance of the detection of H<sub>2</sub> emission in the NW knot as it suggests not only that H<sub>2</sub> is present even in the outermost filaments of NGC 5044, but also that the H<sub>2</sub> to H $\alpha$  ratio is approximately constant throughout the nebula.

#### 2.4.5 INTERPRETATION AND DISCUSSION

##### Imaging

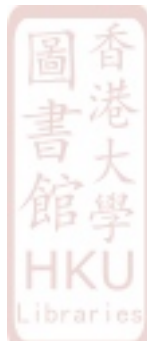
The apparent circum-nuclear color change in NGC 5044 as revealed by our continuum-subtracted H<sub>2</sub> image in Figure 2.21 presents a challenge in terms of its interpretation. We found a similar color change in the ratio of the Spitzer IRAC 4.5 $\mu\text{m}$  to 3.6 $\mu\text{m}$  images of NGC 5044, obtained from the Spitzer archive (Fazio et al. 2004). The 4.5 $\mu\text{m}$  to 3.6 $\mu\text{m}$  ratio is strongly affected by a CO absorption bandhead in the atmospheres of M giants, explaining the Spitzer results. However, we note that 1) the overlap between the CO bandhead and the Ks bandpass is small, with the central velocity of the shortest wavelength CO line ( $^{12}\text{CO}(2-0)$ ) coming in at  $< 50\%$  transmission near the upper bound of the bandpass, and 2) even if a significant amount of CO absorption is present in



the K<sub>s</sub> bandpass, this should have the opposite effect on the narrowband-to-K<sub>s</sub> ratio to what our imaging has revealed (since no CO absorption can be present in the narrowband bandpass, the narrowband-to-K<sub>s</sub> ratio should increase, leading to a positive residual rather than a negative one). Another possible origin of the circum-nuclear color change is metal line absorption in stellar atmospheres. Our NIR spectroscopic results show an absorption feature just short of the H<sub>2</sub> emission line identified as AlI in Mannucci et al. (2001). However, the depth of this absorption feature alone is not sufficient to explain the pronounced negative residual seen in our imaging: if the H<sub>2</sub> emission is below the noise level, then the AlI absorption must be as well. Therefore, the residual feature shown in Figure 2.21 defies a known explanation. We leave open the possibilities that the residual is caused by some hitherto unexplained physical process, or some mysterious artifact of the ‘I‘iwi pipeline or our own data reduction.

### Spectroscopy: Kinematics

As outlined in the introduction, the dominant excitation mechanism of the nebula determines whether or not the molecular and atomic phases can co-exist in the same volume: excitation by penetrating X-ray electrons (or other particles) allows both gas phases to coexist, while processes that purely deposit thermal energy to excite different phases do not. Therefore, if penetrating electrons are indeed the dominant power source of the nebula, the kinematics of the CO, H<sub>2</sub> and H $\alpha$  emission lines should also be strongly coupled. Conversely, in the pure heating excitation scenario, clouds of cooler and denser molecular gas should penetrate more easily through the surrounding ICM than hotter, more diffuse clouds due to differing effects of ram pressure on their trajectories, and thus kinematic decoupling should take place. To investigate how quickly



such decoupling might occur and whether or not it would be detectable, we made simple analytical calculations of gas clouds of varying temperature/density falling towards the center of NGC 5044 through the hot X-ray ICM. We varied the temperatures of the clouds to reflect distinct phases: a cold molecular (CO) phase at  $\sim 10 - 100$ K, a warm molecular ( $H_2$ ) phase at  $\sim 10^3$ K, and a hot ionized ( $H\alpha$ ) phase at  $\sim 10^4$ K. We assumed the clouds to be in pressure equilibrium with the surrounding ICM, with typical values for the ICM pressure in NGC 5044 coming from the deprojected density and temperature profiles of David et al. (2017). In our initial calculations we adopt the assumption of equal mass clouds. Since the total mass and pressure of each cloud is the same, higher temperature corresponds to a lower density and hence a greater volume, thus leading to a greater cross-sectional area by  $pV = (m/m_H)kT$ , where  $p$  is pressure,  $V$  is the volume of the (spherical) cloud,  $m$  is the mass of the cloud,  $m_H$  is the mass of a hydrogen atom, and  $T$  is the temperature of the cloud. Greater cross-sectional area, in turn, means ram pressure has a greater effect on the falling clouds, impeding – in this specific example – the acceleration of hot, diffuse clouds significantly more than cold, dense ones. We consider these clouds in free fall from a fixed initial radius  $r_0$  through the potential  $U = -GM/(r+a)$ , where  $a$  is related to the effective radius of the galaxy by  $R_e \approx 1.8153a$ , proposed by Hernquist (1990) as an analytic approximation for elliptical galaxies. Using the equation for ram pressure,  $p_{ram} = \rho_{icm}\dot{r}^2$ , where  $\rho_{icm}$  is the density of the ICM, we obtain the equation of motion of the clouds

$$\ddot{r} = -\frac{GM}{(r+a)^2} + \frac{\rho_{icm}A}{m}\dot{r}^2$$

where  $A$  is the cross-sectional area of the cloud,  $r$  is distance from the center of NGC 5044, and  $M$  is the mass of NGC 5044. For a spherical cloud, this then



Parameter	Value
Initial height, $r_0$	4.5kpc
ICM density, $n$	0.033cm $^{-3}$
ICM pressure, $p$	0.027keV cm $^{-3}$

Table 2.3 Parameters for iteration 1

Parameter	Value
Initial height, $r_0$	1.0kpc
ICM density, $n$	0.11cm $^{-3}$
ICM pressure, $p$	0.090keV cm $^{-3}$

Table 2.4 Parameters for iteration 2

becomes

$$\ddot{r} = -\frac{GM}{(r+a)^2} + \kappa r^2$$

with

$$\kappa \equiv \left(\frac{3kT}{4p}\right)^{2/3} \left(\frac{\pi m_H}{m}\right)^{1/3} n_{icm}$$

where  $n_{icm}$  is the density of the surrounding ICM.

We obtained values of  $M = 3.4 \times 10^{11} M_\odot$  and  $R_e = 10\text{kpc}$  from Mathews et al. (2005) analysis of the NGC 5044 group, and set the mass of the clouds at  $m = 100M_\odot$ . We ran the model twice, each time using a different value of the initial radius,  $r_0$ , and accordingly different values of the ICM density,  $n_{icm}$ , and pressure,  $p_{icm}$ . In the first iteration, we set  $r_0$  based on the furthest radius to which our observations extend (the NW knot at 4.5kpc); in the second iteration we used the greatest radius at which all three gas components are detected in our observations ( $\sim 1.0\text{kpc}$ , see Figure 2.23). The densities and pressures of the ICM for each iteration are shown in Tables 2.3, and 2.4, while the results of the first and second iterations are displayed in Figures 2.27 and 2.28 respectively. In each figure we also plot results with zero ram pressure for comparison.



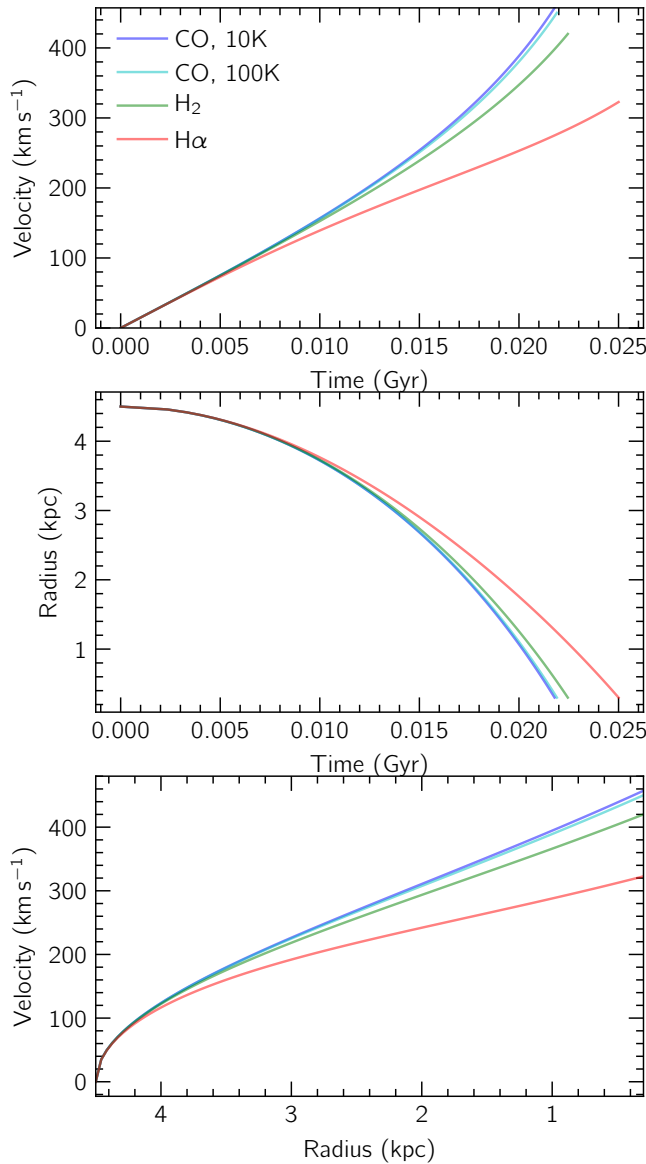


Figure 2.27 Trajectories of gas clouds of varying temperature/density falling through the ICM towards the cluster core from initial height of 5 kpc.



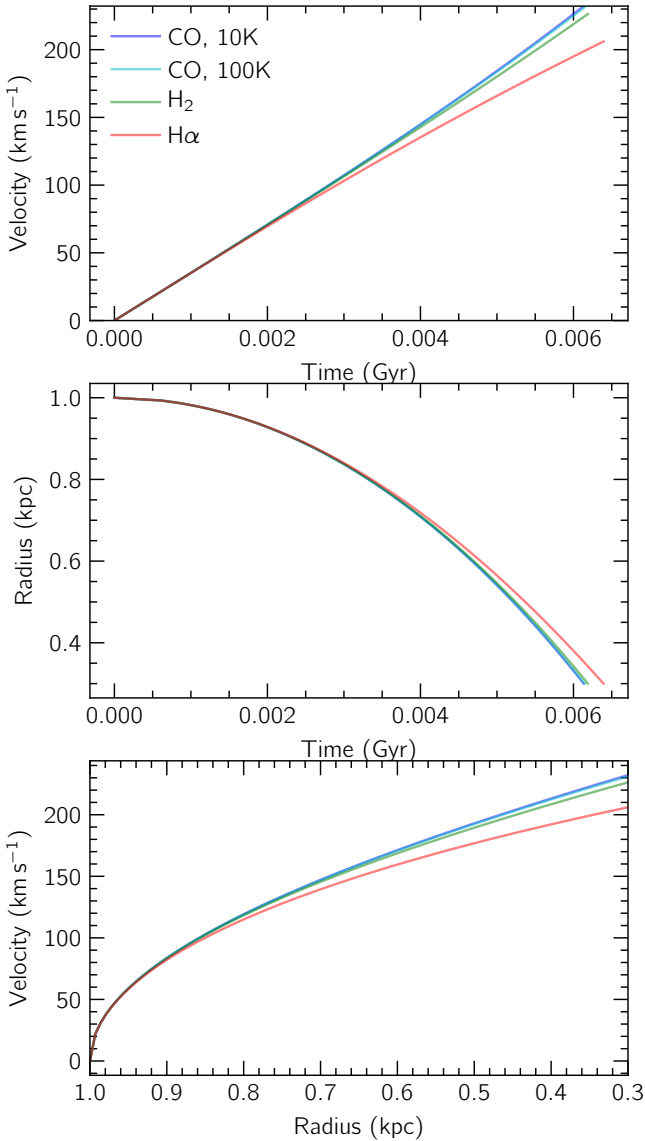


Figure 2.28 Trajectories of gas clouds of varying temperature/density falling through the ICM towards the cluster core from initial height of 1 kpc.



For an initial radius  $r_0 = 4.5\text{kpc}$ , the results in Figure 2.27 show that, under the assumptions stated above, distinct clouds in different phases should quickly kinematically decouple in just a few Myr due to ram pressure, with the effect being most pronounced for the phase associated with  $\text{H}\alpha$  emission, which has the lowest density and hence largest cross-sectional area for a fixed mass. Our

results indicate that radial velocity differences between the least dense ( $\text{H}\alpha$ ) and most dense (CO) components reaches  $> 100 \text{ km s}^{-1}$  within  $\sim 20 \text{ Myr}$  of free fall (falling from 4.5 to  $\sim 2 \text{ kpc}$  in this time). By contrast, our observations show that, along the slit, the different lines change in velocity by  $\sim 200 \text{ km s}^{-1}$ , yet track each other closely with differences (if real) no larger than several  $10 \text{ km s}^{-1}$ . Figure 2.24 shows a histogram of the velocity differences between the CO and  $\text{H}\alpha$  components along the slit.

In our second iteration, with  $r_0 = 1.0 \text{ kpc}$ , there is insufficient time for the cloud kinematics to decouple significantly before reaching the minimum radius of  $0.3 \text{ kpc}$  as shown in Figure 2.28. The maximum velocity difference is  $\sim 30 \text{ km s}^{-1}$ , which is reached within just 6Myr. Though this can account for some of the larger velocity differences of  $10 \text{ km s}^{-1}$  seen in our observations, we find that significantly lower differences ( $< 10 \text{ km s}^{-1}$  within 1 sigma) are common, being seen in 9 out of 18 matches between  $\text{H}_2$  and  $\text{H}\alpha$ , in 10 out of 23 matches between CO and  $\text{H}\alpha$ , and in 6 out of 18 matches between CO and  $\text{H}_2$  (excluding the line profiles around the AGN). By contrast, as can be seen in both Figures 2.27 and 2.28, the trajectories of the 10K and 100K clouds are extremely similar, with both experiencing minimal effects due to ram pressure.

We now relax the assumption of equal-mass clouds, and consider the relative masses gas clouds in different phases would need to have in order to remain closely coupled kinematically during free fall. In order to reproduce the strongly similar kinematics that we observe in NGC 5044 for phases in distinct gas clouds, the coefficient  $\kappa$  would have to be approximately the same for each cloud, requiring the average cloud mass of each phase to be related to its temperature by  $m^{1/3}/T^{2/3} \approx \text{const.}$ . Thus, for instance, if we fix the mass of the 10K (CO) phase at  $m_{\text{CO}} = 100 \text{ M}_{\odot}$ , then in order to obtain the same value of  $\kappa$  (and thus



the same trajectory) for the  $10^4$ K H $\alpha$  and  $10^3$ K H $_2$  phases, we require cloud masses  $10^6$  and  $10^4$  times greater than the 10K CO phase, respectively.

In our observations, all CO and H $\alpha$  central velocities agree to within  $100\text{km s}^{-1}$ , and the median difference among central velocities with  $\alpha > 5$  is just  $44\text{km s}^{-1}$ . With this in mind, we calculated what the minimum difference between the masses of each phase would have to be in order for the difference in velocity not to exceed  $100\text{km s}^{-1}$  when the clouds drop from an initial radius of 4.5kpc. We find that velocity differences  $\gtrsim 100\text{km s}^{-1}$  arise between the H $\alpha$  and CO clouds for  $m_{H\alpha} \gtrsim 10m_{CO}$ . Therefore, under the assumption that separate gas clouds at distinct temperatures give rise to each emission line, the close kinematic coupling seen in our observations requires the hot H $\alpha$  clouds to be an order of magnitude more massive than the cold CO clouds (i.e.  $m_{H\alpha}/m_{CO} \approx 10$ ). In order for kinematics to agree to within  $50\text{km s}^{-1}$ , which we find to be a more typical value in our data set, the difference becomes more extreme still, with  $m_{H\alpha}/m_{CO} \approx 100$ . These mass ratios stand in stark contrast with mass estimates of the different gas phases, in which the gas phase traced by CO dominates by a wide margin (see, for instance Edge 2001). In light of these calculations, we argue that the *prima facie* interpretation of the strong kinematic coupling between the H $\alpha$ , H $_2$ , and CO phases as shown in 2.23 is emission from common gas clouds excited by penetrating particles from the surrounding ICM.

### Spectroscopy: Line Ratios

We now consider the implications of the line ratios for the excitation of the nebular gas in light of prior studies of another cool-core BCG: NGC 1275 in the Perseus cluster. In NCG 1275, an H $_2$  to H $\alpha$  + [NII] ratio of 0.05 was found (Lim et al. 2012). Spectroscopic observations of NGC 1275 (Hatch et al. 2006)



show an H $\alpha$  to [NII] ratio of  $\sim 0.8$ , giving an H<sub>2</sub> to H $\alpha$  ratio of  $\sim 0.1$ , compared with 0.11 in NGC 5044 found in this study. At first glance, the similarity of these line ratios is surprising considering the vastly greater X-ray gas pressure in the far richer Perseus cluster. Under the excitation model presented by Ferland et al. (2009) and Fabian et al. (2011), the H<sub>2</sub>-to-H $\alpha$  line ratio at a given pressure depends on the density (or, equivalently, temperature) of the gas in the filaments; furthermore, the fractional abundance of molecular, atomic, and ionized hydrogen depends on the energy flux of the impinging particles from the surrounding X-ray ICM. Indeed, we estimate the pressure in the filaments of NGC 1275 to be  $\sim 5$  times greater than in those of NGC 5044 based on de-projected models of the X-ray gas in Churazov et al. (2003) for NGC 1275 and David et al. (2017) for NGC 5044, and assuming pressure equilibrium between the X-ray gas and the filaments. Therefore, assuming the same temperature in the filaments of NGC 1275 as those of NGC 5044, the density of the filamentary gas is  $5\times$  higher in NGC 1275. However, as we have noted, the H<sub>2</sub>-to-H $\alpha$  line ratio also depends on the fractional abundance of molecular, atomic, and ionized hydrogen, which in turn is sensitive to the energy flux of the penetrating particles.

An estimate of the flux of penetrating particles into the filaments can be made by following the argument of Fabian et al. (2011), in which the penetrating flux is taken to be  $\sim 5\phi p_{icm}c_s$ , where  $\phi \sim 1$  accounts for uncertain physics,  $p_{icm}$  is the gas pressure and  $c_s = \sqrt{p_{icm}/\rho_{icm}}$  is the sound speed of the gas. Using values for temperature and density of the X-ray gas surrounding the filaments as given in Table 2.5 (based on models provided in David et al. (2017)) we find the energy flux from the electrons penetrating into the outer filaments (at a radius of 30") to be  $\sim 0.08\text{erg cm}^{-2}\text{s}^{-1}$ , compared to  $\sim 0.4\text{erg cm}^{-2}\text{s}^{-1}$  in NGC 1275.



Parameter	NGC 5044	NGC 1275
Radius/kpc	3	30
$T_{icm}$ /keV	0.84	3.1
$n_{icm}$ /cm $^{-3}$	0.028	0.035
$p_{icm}$ /keV cm $^{-3}$	0.024	0.11

Table 2.5 Typical ICM parameters for NGC 5044 and NGC 1275

Thus we find the energy flux due to penetrating particles in NGC 1275 to be 5 times higher than in NGC 5044. It is thus at least feasible that the increased pressure and density in the filaments of NGC 1275 is offset by the greater flux of penetrating particles to give a similar line ratio as in NGC 5044; however, more rigorous modeling is needed to establish whether this may actually be the case.

As a further check on the feasibility of the penetrating particle excitation model, we compare the flux of penetrating particles with the surface brightness of the filaments in NGC 5044 and NGC 1275. In NGC 5044, the surface brightness of the filaments is  $\sim 5 \times 10^{-16}$  erg s $^{-1}$  cm $^{-2}$  arcsec $^{-2}$  in H $\alpha$ , which gives an outward flux of  $\sim 1 \times 10^{-4}$  erg s $^{-1}$  cm $^{-2}$ . Scaling this up by a factor of  $\sim 20$  to account for outward flux contributed by other emission lines gives  $\sim 0.003$  erg s $^{-1}$  cm $^{-2}$ . Thus the energy provided by the penetrating electrons ( $\sim 0.08$  erg cm $^{-2}$  s $^{-1}$ , see above) can power the line emission from the nebula if the excitation efficiency is  $\sim 0.04$ . Following the equivalent calculation for NGC 1275, with H $\alpha$  surface brightness of  $\sim 5 \times 10^{-15}$  erg s $^{-1}$  cm $^{-2}$  arcsec $^{-2}$ , total outward line emission flux of 0.03 erg s $^{-1}$  cm $^{-2}$ , penetrating particle flux of  $\sim 0.4$  erg cm $^{-2}$  s $^{-1}$ , we find an excitation efficiency of  $\sim 0.08$ . Thus, although the flux of penetrating electrons is about 5 times higher in NGC 1275 than NGC 5044, the excitation efficiency is comparable to within a factor of 2. This constitutes a remarkable coincidence if different physical processes dominate excitation of the two nebula.



As discussed in chapter 1, an obvious excitation source is photoionization by the X-rays produced by the surrounding ICM. In NGC 1275, this was argued to be an insufficient power source, as the surface brightness of the X-ray gas falls short of that of the nebular gas by at least two orders of magnitude (Lim et al. 2012). In NGC 5044, on the other hand, we find that the X-ray surface brightness ( $\sim 1 \times 10^{-15} \text{ erg s}^{-1} \text{ cm}^{-2} \text{ asec}^{-2}$ ) is comparable to the surface brightness of the filaments ( $\sim 1 \times 10^{-15} \text{ erg s}^{-1} \text{ cm}^{-2} \text{ asec}^{-2}$ ), though the X-ray brightness falls short of the nebular brightness by up to a factor of two in the outer filaments. Therefore, it is possible that photoionization X-rays may play a more significant role in the excitation of the nebula in NGC 5044 compared with NGC 1275. However, while the X-ray surface brightness decreases with radius from the group center, we do not find any corresponding change in the H<sub>2</sub>-to-H $\alpha$  ratio that would be expected due to the changing ionization fraction. Furthermore, X-ray surface brightness maps (e.g. David et al. (2011)) do not show any drop in X-ray surface brightness associated with the filaments. Therefore, we do not find any evidence for X-ray photoionization as the dominant excitation mechanism.

#### 2.4.6 SUMMARY AND CONCLUSIONS

We presented results of NIR imaging observations of the 2.12 $\mu\text{m}$  H<sub>2</sub> line from NGC 5044 as well as spectroscopy covering the H $\alpha$ +[NII], H<sub>2</sub>, and 1.3mm CO lines. Our imaging observations did not achieve the sensitivity required to detect H<sub>2</sub> emission, thus placing an upper limit on the H<sub>2</sub>/H $\alpha$ +[NII] ratio in the filaments of  $\sim 1$ , which is much higher than the ratio found in NGC 1275 (0.05). Interestingly, we found a radial color gradient in the stellar continuum of NGC 5044 around 2.12 $\mu\text{m}$ , the nature of which we explored but could not



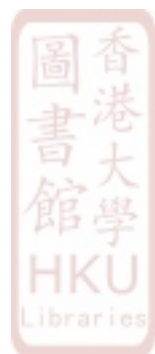
satisfactorily explain.

We analyzed archival spectroscopy of the H<sub>2</sub> and H $\alpha$  lines from NGC 5044 as well as our own spectroscopy of the 1.3mm CO(2-1) line. The H<sub>2</sub> observations comprised long slit spectra, while H $\alpha$  and CO spectra were initially in data cubes from which we extracted simulated long slit spectra to match the H<sub>2</sub> observations. We then fitted Gaussian line profiles to the emission lines along the length of the slit. We showed that the spectral profiles of the H $\alpha$ , H<sub>2</sub>, and CO lines along the slit are remarkably similar, indicating very close kinematic coupling between the three gas phases throughout the nebula. Such close kinematic coupling indicates that the different emission lines – at vastly different excitation levels – all originate from the same volume of gas. If, on the other hand, the molecular lines originate from dense gas and the atomic/ionized lines from gas at much lower densities, the dense molecular (CO) phase would rapidly decouple from the hot atomic/ionized (H $\alpha$ ) phase due to the effects of ram pressure as the gas in the filaments moves through the surrounding ICM. Emission of these three spectral lines from the same volume of gas, in turn, supports the idea that the dominant excitation mechanism of the gas is energetic particles penetrating into the filaments. A possible source of these is electrons from the surrounding X-ray ICM, as proposed by Fabian et al. (2011).

To gain further insight into the excitation mechanism, we measured the H<sub>2</sub>/H $\alpha$  ratio along the spectroscopic slit. We find a value of  $\sim 0.1$  that is relatively constant throughout the nebula, strongly suggesting that the entire nebula in NGC 5044 has a 2.12 $\mu$ m H<sub>2</sub> counterpart as is true for NGC 1275, the central elliptical galaxy in the Perseus cluster (Lim et al. 2012). The ratio itself is also very close to that in NGC 1275, at  $\sim 0.1$ , suggesting similar physical conditions in the two nebulae. We worked out whether this can indeed be



the case, and found that the density of the filaments in NGC 1275 are  $\sim 5$  times greater than that of the filaments in NGC 5044; however, the flux of penetrating particles in NGC 1275 is also  $\sim 5$  times greater. We concluded that more detailed modeling is needed to understand whether these two differences can offset each other.



# Chapter 3

## Excitation of the Cool-Core Nebula in NGC 5044



empty

In Chapter 2, I used integral field unit (IFU) optical data from the Multi-Unit Spectroscopic Explorer (MUSE) at the VLT to compare the H $\alpha$ +[NII] spectral profiles with those of H<sub>2</sub> and CO lines from NGC 5044. The relative strengths can be compared with model predictions to rule out/favor excitation mechanisms proposed for powering the line emission from cool-core nebulae. In Chapter 2, I showed that the H<sub>2</sub>/H $\alpha$  appears to be relatively uniform as a function of radius from the center, and that this line ratio is incompatible with model for pure heating (in which only one phase can exist in a given gas volume). Here, I make a more stringent test of the predictions by (Ferland et al. 2008; Ferland et al. 2009) that cool-core nebulae are energized by energetic particles, a test that also definitely rules out pure thermal excitation.

Quantitative tests can be made by comparing the strength of certain optical emission lines, e.g. the [OIII], [OI], H $\alpha$ , and HeI. Figure 3.1 shows a plot reproduced from Ferland et al. (2009) that shows the relative emissivities of various optical emission lines for a range of temperatures under excitation by energetic particles (upper panels) and pure heating (lower panels). These plots assume a fixed pressure in the gas (equal to that found in NGC 1275 assuming pressure equilibrium between the gas and surrounding hot X-ray gas). The gray region along the upper x axis indicates the thermally unstable regime. The plots demonstrate how observed line ratios in cool-core nebulae can be used to test the energetic particle and pure heating excitation models. For instance, under the pure heating case, HeI emission (lower right panel) must be accompanied by [OIII] emission  $\gtrsim$  2 orders of magnitude brighter (lower right panel). This is simply due to the much higher energy required to excite HeI compared to what is needed to ionize and excite [OIII]. By contrast, in the energetic particle case



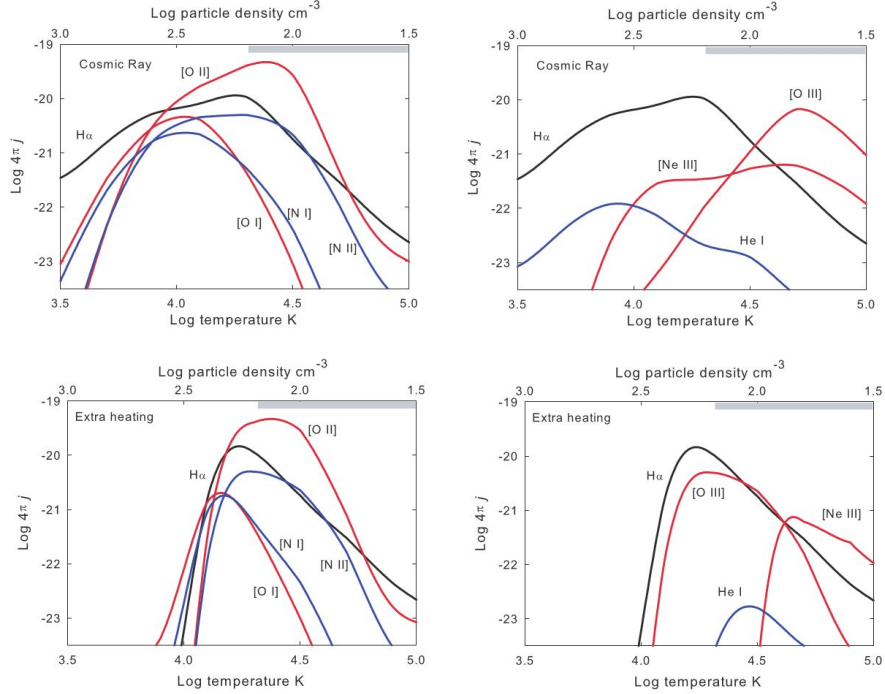


Figure 3.1 Plot from Ferland et al. (2009) illustrating how [OI] and [OIII] emissivity can be used to constrain excitation and gas properties.

(upper panels labeled “cosmic ray”), at sufficiently low temperatures HeI can be produced while [OIII] remains undetectable undetectable.

In this Chapter, I use the MUSE IFU data to map [OIII], [OI], and H $\alpha$  emission throughout the entire nebula in NGC 5044, with the aim of using the line ratios to constrain the excitation mechanism powering the line emission as well as the physical properties (temperature, density) of the gas itself. Inspecting the MUSE data cube, I saw that, in places, [OIII] $\lambda 5007$  and [OI] $\lambda 6300$  emission lines were visible in the spectrum of NGC 5044, as indicated in the example spectrum in Figure 3.2. I therefore set out to map and find ratios between the [OIII] $\lambda 5007$  and [OI] $\lambda 6300$  (hereafter, simply [OIII] and [OI]) as well as the H $\alpha$  emission throughout NGC 5044. Other lines that can be seen in the data cube are the [SII] $\lambda 6717/\lambda 6731$  doublet (high signal-to-noise) and a hint of HeI

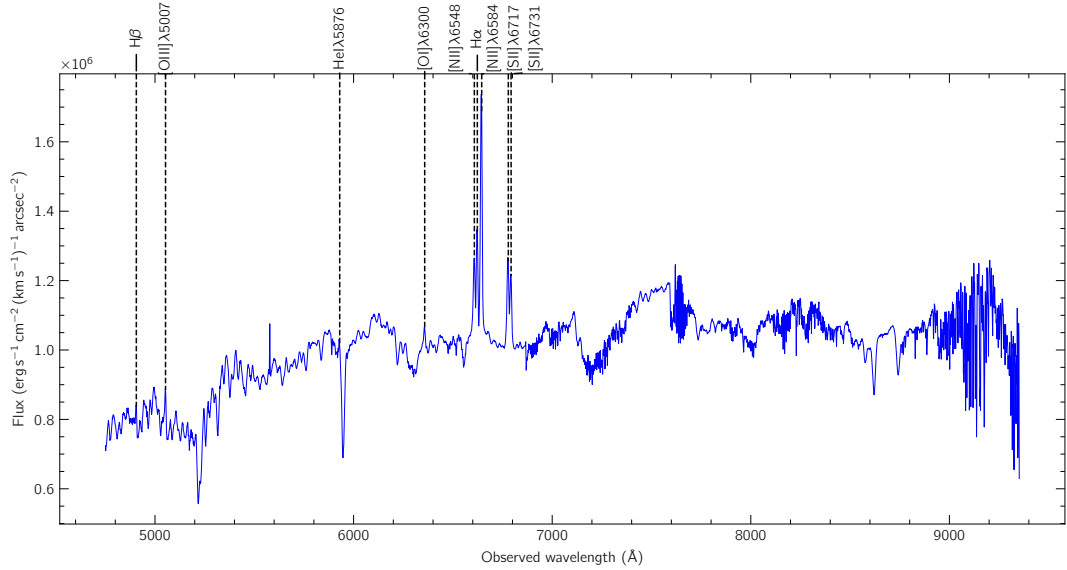


Figure 3.2 Typical spectrum from the bright central part of the nebula in NGC 5044, with selected nebular emission lines indicated.

$\lambda 5876$ . I do not consider the [SII] lines in this study since they do not represent such useful constraints on the excitation mechanism, while the HeI line unfortunately partially overlaps with a stellar absorption line identified as NaI (and is also very low signal-to-noise). The fact that the HeI line cannot be mapped is unfortunate since it represents such a powerful way to distinguish between energetic particle excitation and pure heating. Nonetheless, close inspection of the spectrum in Figure 3.2 gives some idea of the brightness of the HeI line, suggesting a HeI/H $\alpha$  value of  $\lesssim 0.05$ , which is similar to the value of 0.04 found in NGC 1275 (the central elliptical galaxy in the Perseus cluster). In future work, I intend to see if it is possible to accurately remove the NaI absorption to try and map the HeI emission from NGC 5044.

### 3.1 Observations and Data Reduction

I now recount the key details of the MUSE observations (more complete details can be found in 2.1). The observation spanned wavelengths from 4750 Å to 9350 Å with a spectral resolution of  $\sim 2.6\text{Å}$  ( $117\text{km s}^{-1}$ ) at the central wavelength. The instrumental scale was  $0.2''/\text{spaxel}$  and the seeing on the night of observation was approximately  $0.6''$ , with a field size of  $60\times 60''$ . Pre-processing, calibration, and correction for telluric features were carried out automatically at ESO. In addition to the data cube, the MUSE FITS file also contains a variance cube from which I obtain 1-sigma measurement uncertainties by taking the square root. Since the [OIII] and [OI] lines were at low signal-to-noise, I increased the signal-to-noise by smoothing the data cube to an angular resolution of  $\text{FWHM} = 2''$  (originally  $0.6''$ ), and resampling to a grid of size  $0.6''$  per spaxel (originally  $0.2''$ ).

I mapped the [OIII], [OI], and H $\alpha$  emission by fitting Gaussian line profiles to each of the lines in each spaxel of the IFU (recall that in Chapter 2 I made a simulated long slit spectrum from the data cube to match the H $_2$  observations, rather than directly fitting line profiles to individual spaxels). I started by constructing spectral baselines to subtract from each spaxel. The most straightforward way of doing this is to take the median of as many off-nebula spaxels as possible, thus obtaining a baseline containing only stellar features and free from nebular emission, while also minimizing noise in the baseline. The only complication to using this method of obtaining the spectral baseline is that one does not initially know which spaxels should be considered “on-nebula” or “off-nebula” before having done any fitting of line profiles. One possibility would be to use an existing H $\alpha$  image, convolving, resampling and aligning it to match



the MUSE resolution and grid. However, I chose the more straightforward solution of performing a quick and simple initial fitting of the H $\alpha$ +[NII] lines in which I fitted a single Gaussian component to each of the three adjacent lines ([NII] $\lambda$ 6548, H $\alpha$ , and [NII] $\lambda$ 6584) plus a linear baseline in each spaxel (corrected for stellar H $\alpha$  absorption using the same absorption profile calculated in Paper I, see 2.1). The resulting map of H $\alpha$  surface brightness is shown in Figure 3.3 along with an example of a spaxel with fitted H $\alpha$ +[NII] lines. Next, I generated a baseline by taking the median of all the spaxels in which the amplitude of the fitted H $\alpha$  line fell below 3 sigma (I also masked out regions within 10 spaxels of the edges of the images, as these showed obvious artifacts). The resulting baselines around the [OIII], [OI], and H $\alpha$ +[NII] spectral regions are shown in Figure 3.4. The H $\alpha$ +[NII] baseline (top panel) shows some contamination from [NII] emission, visible at  $\sim 6640\text{\AA}$ ; consequently, I may need to impose more strict criteria on the spaxels used to construct the baseline when refining the data reduction process in future.

There was one complication that arose during this process: the redshifted [OI] line from NGC 5044 lies at  $\lambda = 6358\text{\AA}$ , very close to the rest frame wavelength of the [OI] $\lambda$ 6363 in our own atmosphere. This telluric feature can be seen as a gray dashed line in the baseline shown in Figure 3.4 (middle panel) and in some spaxels slightly overlaps with the [OI] line from NGC 5044. However, since this is a telluric feature, it does not increase in depth with increasing continuum surface brightness, which means that it becomes relatively weaker compared to the stellar features towards the center of the galaxy, eventually falling below the noise level. This means that a) the feature is extremely weak throughout most of the on-nebula spaxels and b) it cannot be removed using my baseline subtraction method. Therefore, I simply masked the affected wavelengths in



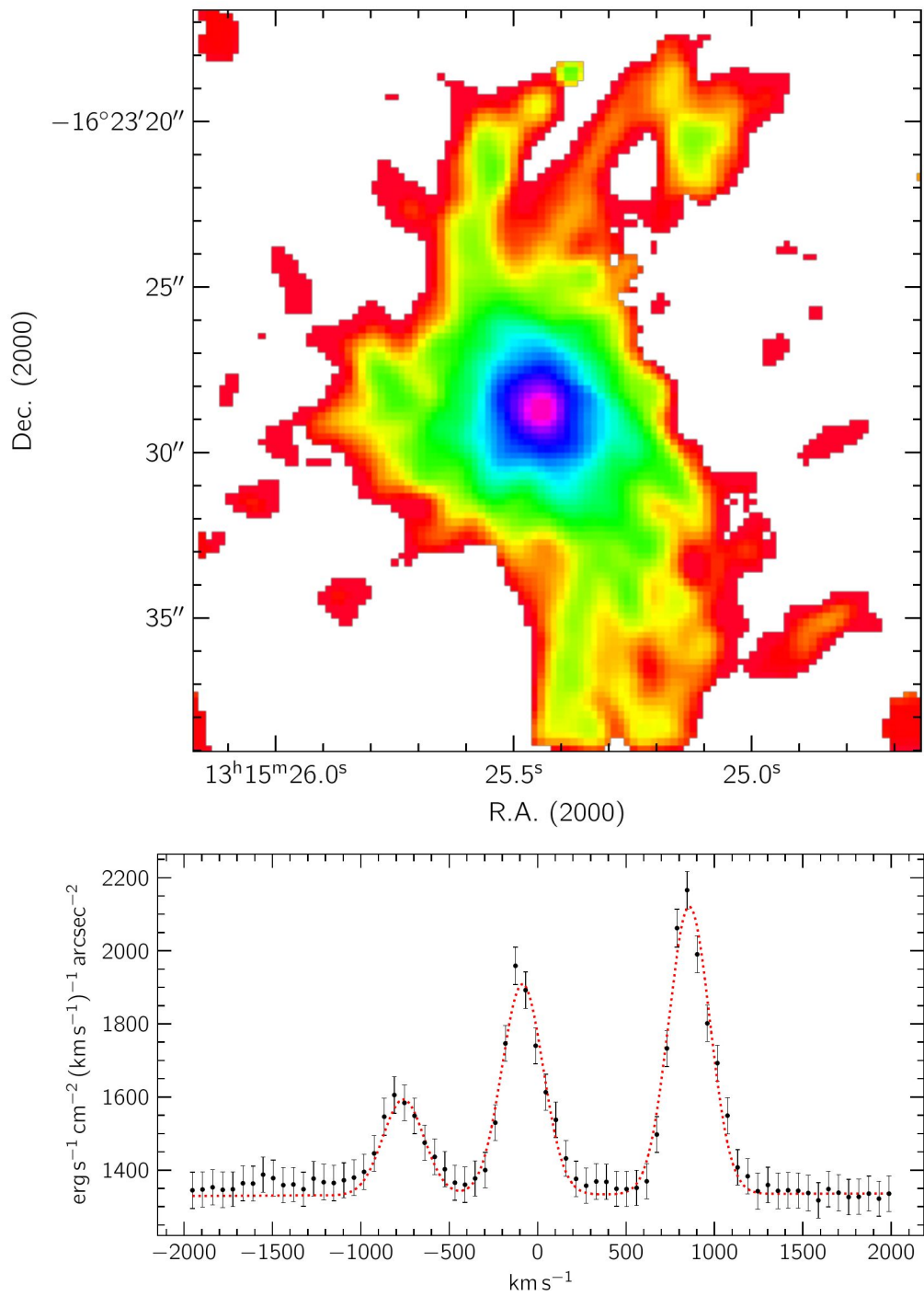


Figure 3.3 Top: H $\alpha$  surface brightness map used to determine on- vs off-nebula spaxels. Pixels with H $\alpha$  emission below 3 sigma are blank. Bottom: H $\alpha$ +[NII] lines with fitted model before baseline subtraction.

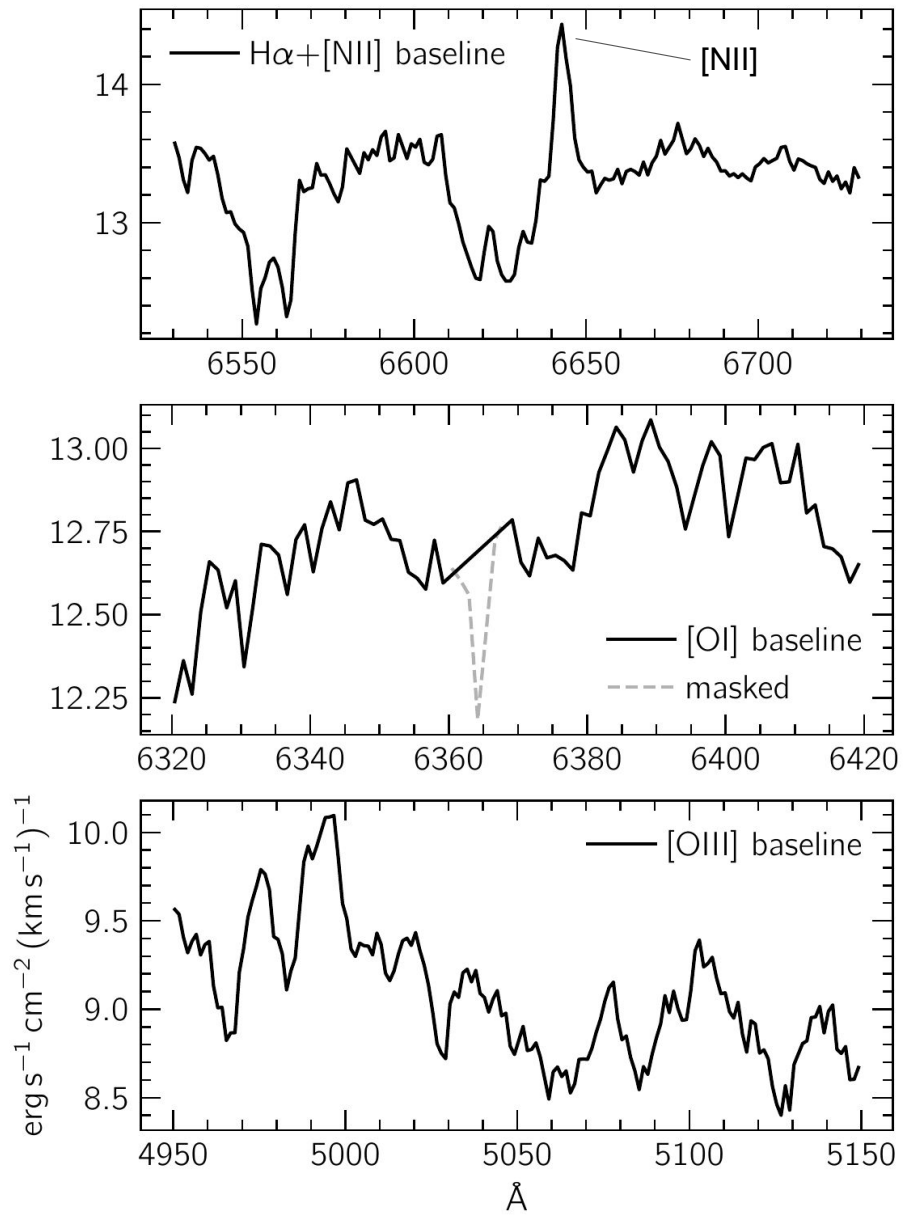


Figure 3.4 Spectral baselines for the  $\text{H}\alpha + [\text{NII}]$  (top),  $[\text{OI}]$  (middle), and  $[\text{OIII}]$  (bottom) lines. Some (limited)  $[\text{NII}]$  emission can be seen in the top panel which will have to be corrected in refinements to the data reduction procedure.

the baseline and interpolated over them.

After having generated the baselines in this way, I then cut three slices (i.e. sub-cubes with limited wavelength ranges) out of the MUSE data cube: one for each of the [OIII], [OI], and H $\alpha$  lines. The [OIII] slice covered 4950Å to 5150Å, the [OI] slice covered 6320Å to 6420Å, and the H $\alpha$  slice covered 6530Å to 6730Å. Example spaxels from each of the three slices are shown in the left column of Figure 3.5. Next, I subtracted the baselines from each spaxel in each slice. In order to do this properly, it is first necessary to apply a scaling factor to the baseline before subtracting it, since the continuum level varies from spaxel to spaxel. I calculated the scaling factor for each spaxel by masking out the emission lines and then taking the ratio  $\mu_{on}/\mu_{off}$ , where  $\mu_{on}$  and  $\mu_{off}$  are the medians of the masked on-nebula and baselines respectively. I then subtracted the scaled baselines from each spaxel. The same example spaxels are shown after baseline subtraction in the right column of Figure 3.5.

## 3.2 Results

Once the baselines had been subtracted from each spaxel in each of the three cube slices, I began the line profile fitting process. I performed two rounds of fitting: first I fitted exclusively single-Gaussian profiles to each emission line in each spaxel, and then later I modified the fitting script to include the possibility of double-Gaussian profiles where appropriate. Here, I describe the method and results of the latter fitting process.

A cursory glance at the MUSE data cube reveals that there are a considerable number of spaxels in which the H $\alpha$ +[NII] line profiles are clearly double-peaked, as shown in the example in Figure 3.6. In the higher signal-to-noise spectra,



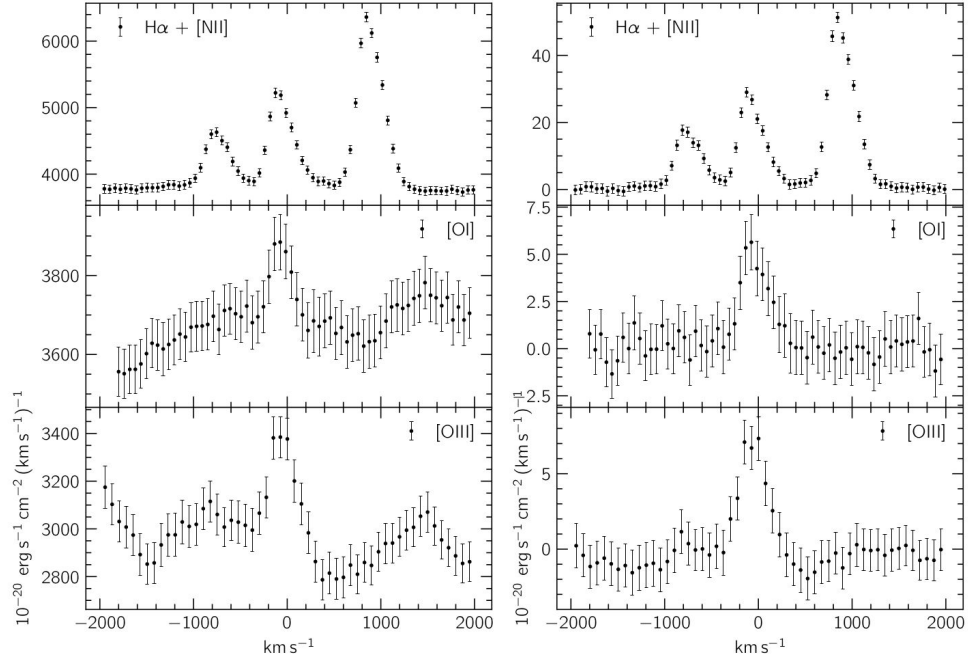


Figure 3.5 Example spaxels from each of the three slices:  $\text{H}\alpha$  (top),  $[\text{OI}]$  (middle), and  $[\text{OIII}]$  (bottom) showing the emission lines before (left column) and after (right column) baseline subtraction.

double peaks can also be discerned in  $[\text{OIII}]$  and  $[\text{OI}]$ . Such double-peaked profiles are commonplace in the bright inner region of the nebula, presumably due to multiple filaments along the same sight line. Knowing that this was the case, I developed a procedure to fit either a single- or a double-Gaussian to each spaxel depending on the line profile. This procedure starts by fitting a single-Gaussian profile to each of the  $\text{H}\alpha + [\text{NII}]$  lines, with a common central velocity and velocity dispersion for the  $[\text{NII}]\lambda 6548$ ,  $\text{H}\alpha$ , and  $[\text{NII}]\lambda 6584$  lines. If the reduced  $\chi^2$  of the single-Gaussian profile is less than or equal to 1.0, then a single-Gaussian profile is considered acceptable and the script moves to the next spaxel. If the reduced  $\chi^2 > 1.0$  for the single-Gaussian fit, then a double-Gaussian profile is also fitted. Next, the integrated flux,  $f$ , under each Gaussian in the double-Gaussian profile is compared to its uncertainty,

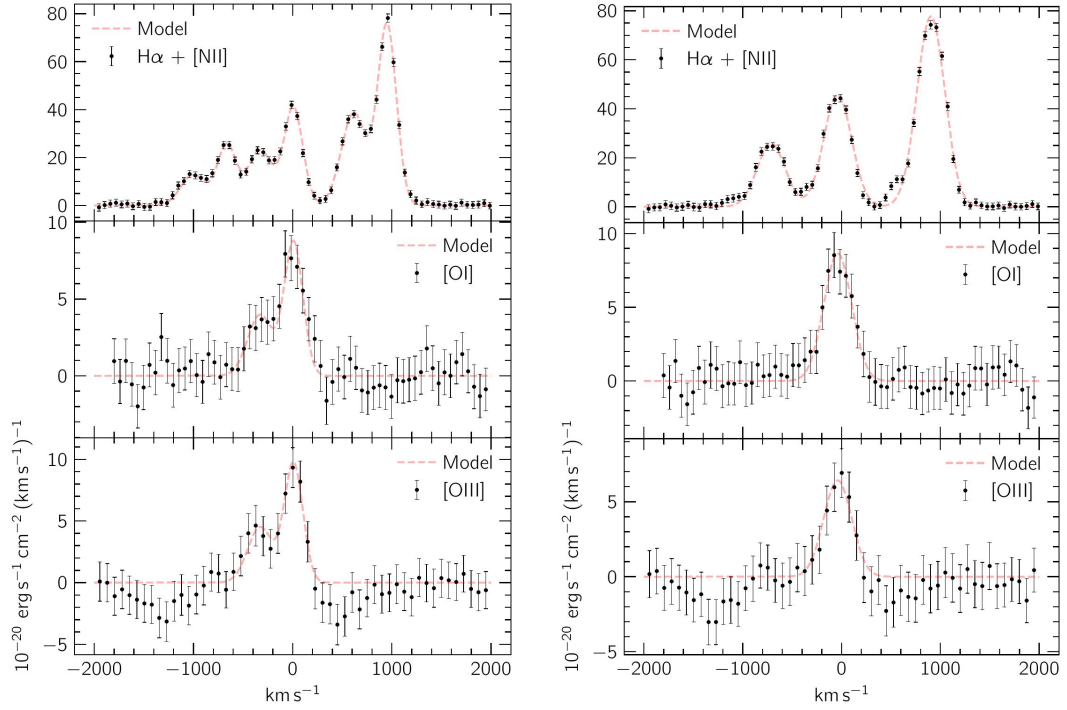


Figure 3.6 Left: Example of a spaxel from the bright inner region of the nebula where line profiles are frequently double-peaked, with fitted double-Gaussian profile shown. Right: Example of a spaxel where a single-Gaussian profile has been fitted.

$\Delta f$ , as reported by the covariance matrix produced by the fitting package. If  $f/\Delta f < 3.0$  for *either* of the Gaussians, then the double-Gaussian fit is discarded and the single-Gaussian profile is considered acceptable. On the other hand, if  $f/\Delta f > 3.0$  for both Gaussians, then the double-Gaussian profile is accepted and the script moves on to the next spaxel. Figure 3.6 shows examples of double- and single-Gaussian line profiles.

After fitting the H $\alpha$ +[NII] profiles, I fitted single- or double-Gaussian profiles to the [OI] and [OIII] lines. In each spaxel, I fixed the central velocity and velocity dispersions of the fitted [OI] and [OIII] lines to be the same as those of the (already fitted) H $\alpha$ +[NII] lines owing to their low signal-to-noise (this

means that I fit only one parameter for the [OI] and [OIII] lines: the flux density). Assuming the same kinematics for the [OI] and [OIII] as H $\alpha$  is physically justified if the emission is from the same gas volume, and empirically justified by visual inspection of the line profiles and fitting results in multiple spaxels throughout the nebula; moreover, I found the kinematics of different lines to be the same in chapter 2 even when comparing lines from different gas phases (molecular vs atomic). I fitted the same number of Gaussians to the [OI] and [OIII] as had been fitted to the H $\alpha$  line (i.e. single or double as determined by the process described above). In Figure 3.7 I show surface brightness for the H $\alpha$ , [OI], and [OIII] cube slices for spaxels where emission is detected at the 3 sigma level; in cases where double peaks have been fitted, I show the line with lower central velocity in the left column of the figure. In Figure 3.8 I show the central velocities and velocity dispersions of the fitted H $\alpha$ +[NII] lines; again, in cases where the line is double-peaked the line with lower central velocity is shown in the left column. Also note that the velocity dispersions reported are the FWHM of the fitted Gaussians, and have been reduced to account for the instrumental dispersion of 117km s $^{-1}$ .



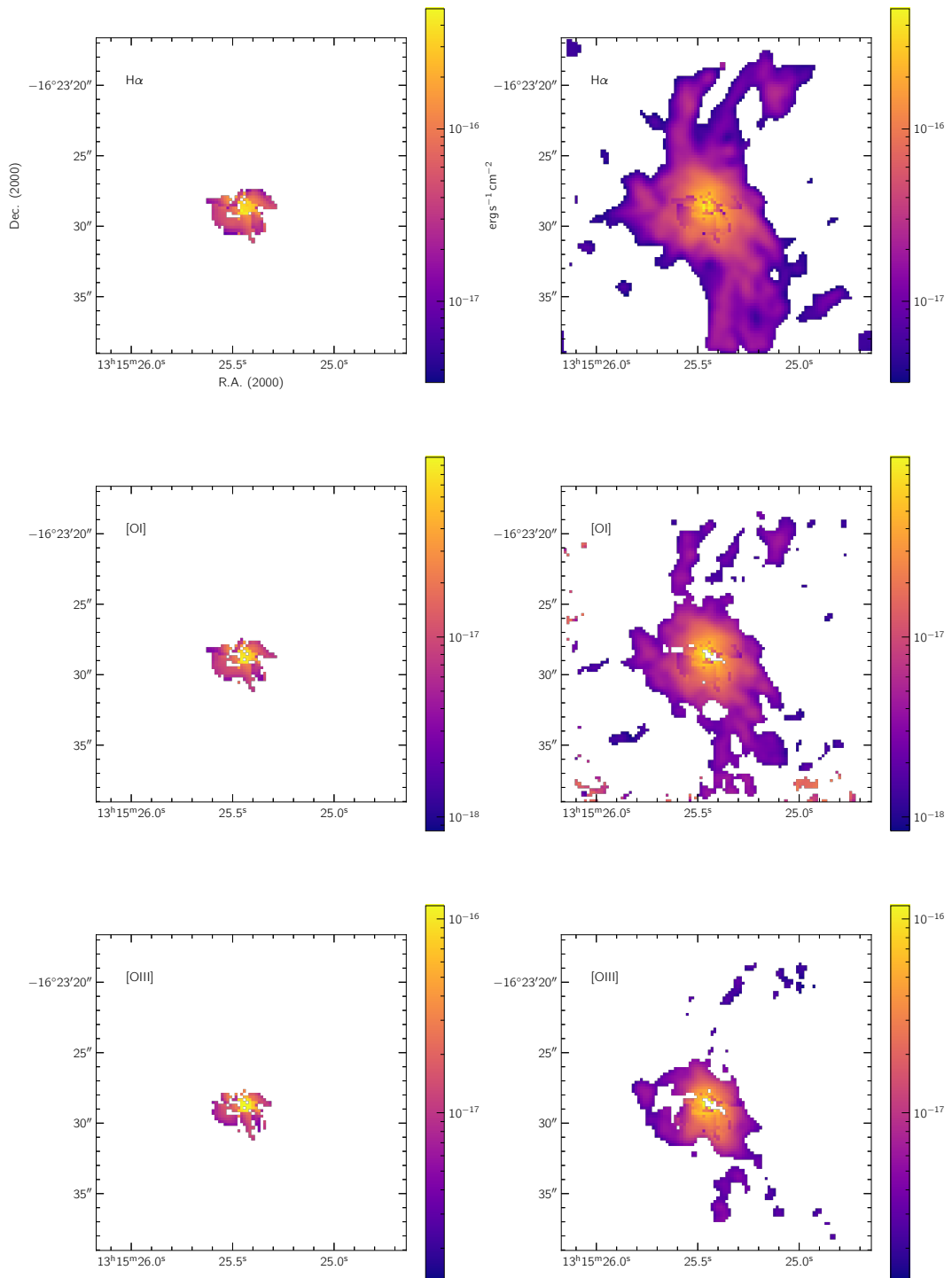


Figure 3.7 Maps of H $\alpha$ , [OI], and [OIII] flux density based on the results of fitting single- or double-peaked line profiles. In cases where double peaks were fitted, the left column shows the lower-velocity component. Spaxels where emission is below 3 sigma are left blank.

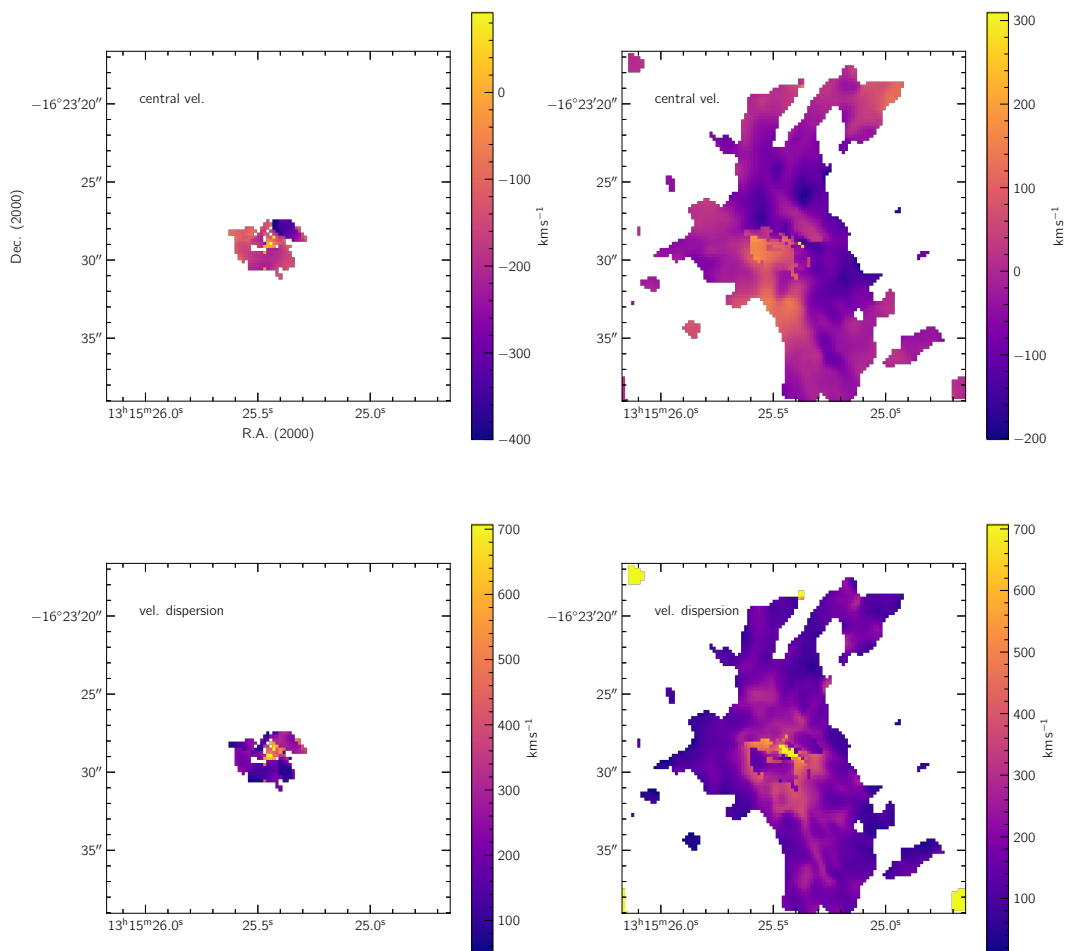


Figure 3.8 Maps of H $\alpha$  central velocity and velocity dispersion (FWHM) for single- or double-peaked line profiles. In cases where double peaks were fitted, the left column shows the lower-velocity component.

From maps of the surface brightness in each emission line, I then generated line ratio maps of the nebula as shown in Figure 3.9. In each figure, pixels below 3-sigma in either of the two emission lines being compared are blanked out. As can be seen in the upper panel of Figure 3.9, the [OI]/H $\alpha$  ratio is approximately constant throughout the nebula at  $\sim 0.1$ . The average [OIII]/H $\alpha$  ratio is also  $\sim 0.1$ , making the average [OI]/[OIII] ratio approximately unity. However, the [OIII]/H $\alpha$  and [OI]/[OIII] ratios are not as uniform as [OI]/H $\alpha$ , changing abruptly moving away from the center of the nebula. The inner region, colored violet/black in the lower panel of Figure 3.9 has an [OI]/[OIII] ratio of  $\sim 0.8$ , but this rises to  $\sim 1.5$  in the surrounding regions, colored orange/yellow. The [OIII]/H $\alpha$  ratio map shown in the middle panel of Figure 3.9 shows a similar pattern, with the relative strength of [OIII] dropping from  $\sim 0.3$  in the interior to  $\sim 0.1$  at the edges. A typical example of a spaxel in which the [OI]/[OIII] ratio is low (and [OIII]/H $\alpha$  is high) is shown on the left side of Figure 3.10, while an example of a spaxel with high [OI]/[OIII] ratio (and low [OIII]/H $\alpha$  ratio) is shown on the right side. These examples show no fundamental difference between the low-[OIII] and high-[OIII] spectra, nor any artifacts of the data reduction process that may be causing these abrupt changes in [OIII]/H $\alpha$  and [OI]/[OIII] ratios.

The (unweighted) mean  $\pm$  standard deviation of the ratios across all spaxels are  $1.1 \pm 0.3$  for [OI]/[OIII] and  $0.19 \pm 0.06$  for [OIII]/H $\alpha$ . Furthermore, I find the global flux-weighted average [OI]/[OIII] and [OIII]/H $\alpha$  ratios to be  $0.926 \pm 0.008$  and  $0.210 \pm 0.001$  respectively. I find the (unweighted) mean  $\pm$  standard deviation of the [OI]/H $\alpha$  ratio across the un-blanked spaxels to be  $0.18 \pm 0.04$ , while the *flux-weighted* global average [OI]/H $\alpha$  ratio is  $0.195 \pm 0.002$ .



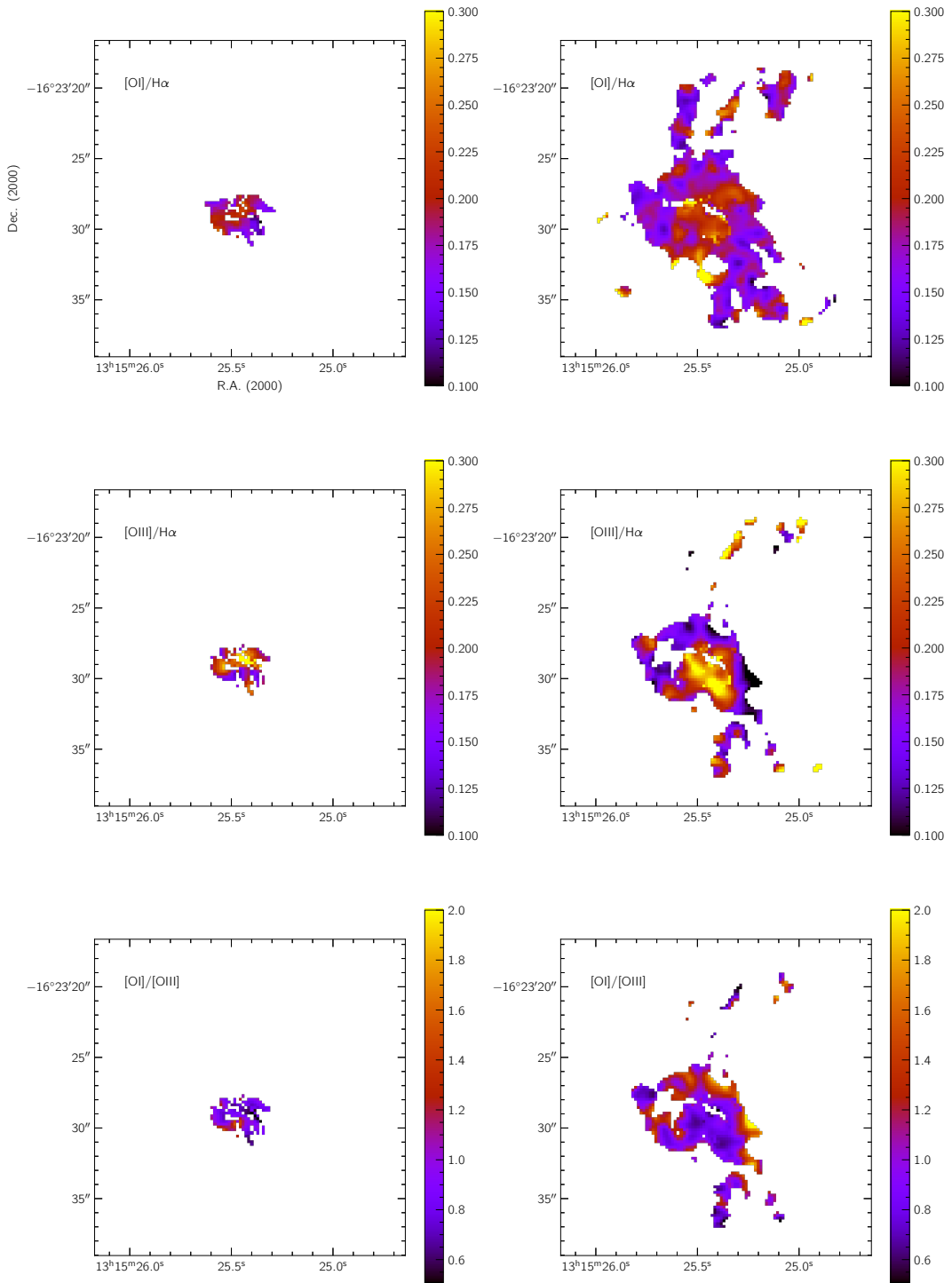


Figure 3.9 From top to bottom:  $[\text{OI}]/\text{H}\alpha$ ,  $[\text{OIII}]/\text{H}\alpha$ , and  $[\text{OI}]/[\text{OIII}]$  line ratio maps for single-Gaussian fitted line profiles.

### 3.3 Interpretation and Discussion

Having mapped the [OI]/H $\alpha$ , [OIII]/H $\alpha$ , and [OI]/[OIII] ratio throughout NGC 5044 as reported in 3.2, I now consider how these results may be used to shed light on the excitation mechanism powering the line emission from the nebula.

As discussed in the introduction to this chapter, comparison of the [OI], [OIII], and H $\alpha$  flux density from cool-core BCG nebulae can serve as a powerful way to distinguish between excitation models, as well as to constrain gas properties. As can be seen in Figure 3.11 (the same plot I showed in the introduction to this chapter, printed here again for the reader's convenience), the range of possible [OI]/H $\alpha$  and [OIII]/H $\alpha$  ratios depends on the excitation mechanism, and a precise measurement of the ratios can even be used to estimate the density and temperature of the gas, which, in conjunction with models of the gas filaments, can help us understand the evolution of these nebulae.

The plots in Figure 3.11 assume a pressure equal to that found in the X-ray ICM surrounding the filaments of NGC 1275. Since the Perseus cluster, which NGC 1275 lies at the center of, is far more massive than the NGC 5044 group, the pressure is accordingly higher in the filaments of NGC 1275 compared to NGC 5044. As I discuss in 2.3, the pressure in NGC 1275 is about an order of magnitude higher than in NGC 5044, meaning that the plots in Figure 3.11 cannot be used with the results I have presented to constrain the gas excitation or properties. We planned a collaboration with Gary Ferland to generate plots suitable for NGC 5044, but due to time pressures he was unable to accommodate us.

Having said this, it is instructive to consider what *could* be learned from Figure 3.11 if it were applicable to NGC 5044. Looking at the lower two panels



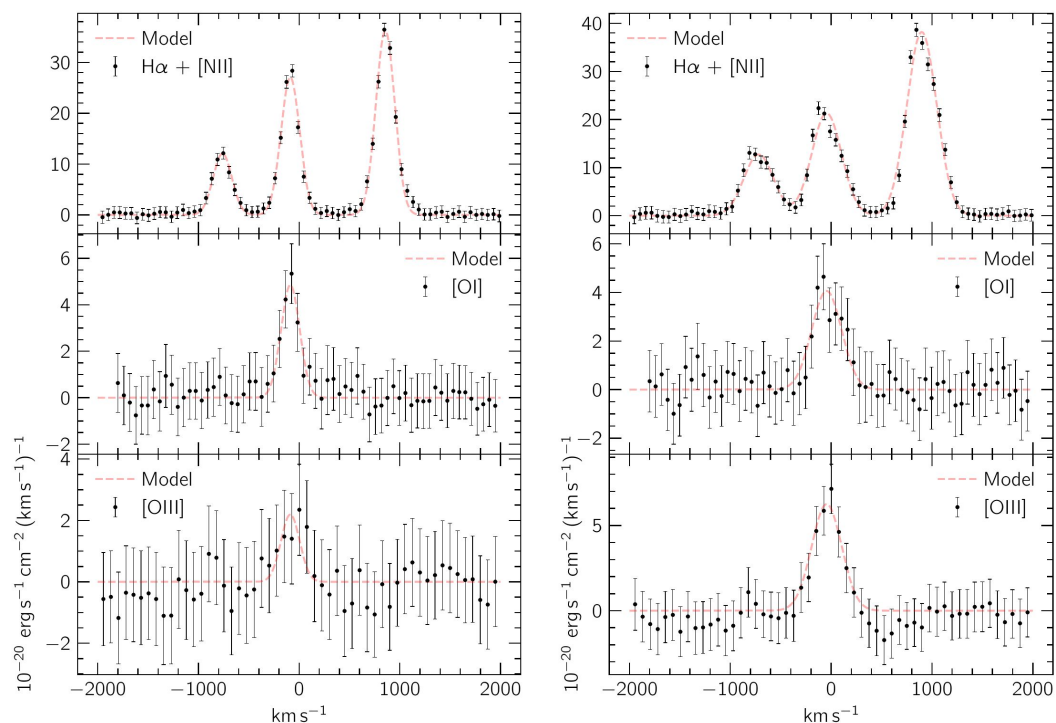


Figure 3.10 The left shows an example spaxel covering the  $\text{H}\alpha$ ,  $[\text{OI}]$ , and  $[\text{OIII}]$  lines from the regions of the nebula where the  $[\text{OIII}]/\text{H}\alpha$  ratio is relatively low and  $[\text{OI}]/[\text{OIII}]$  is relatively high; the right shows an example from where the  $[\text{OIII}]/\text{H}\alpha$  ratio is relatively high and  $[\text{OI}]/[\text{OIII}]$  is relatively low.

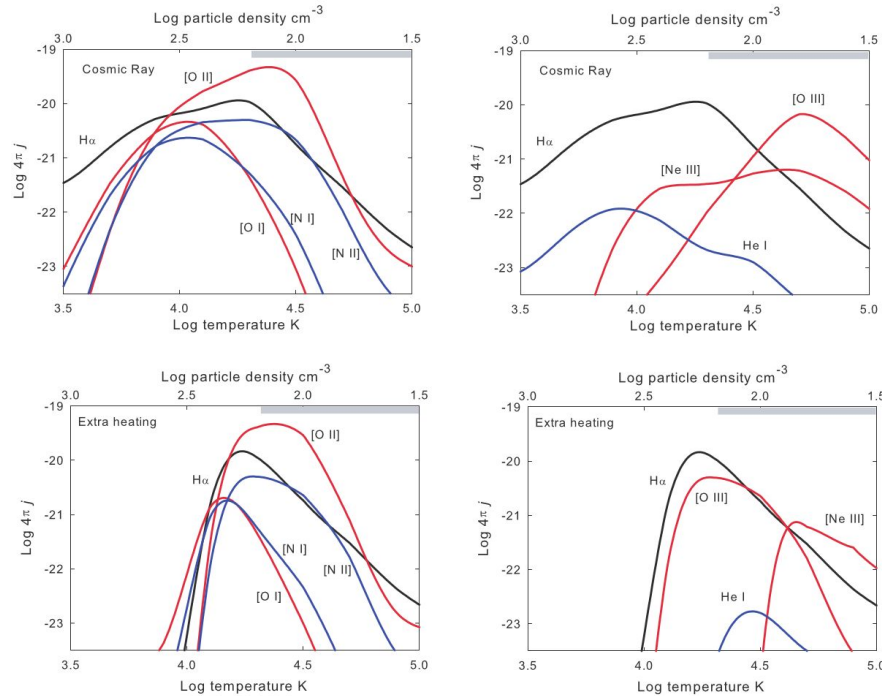


Figure 3.11 Plot from Ferland et al. (2009) illustrating how [OI] and [OIII] emissivity can be used to constrain excitation and gas properties.

shows that for purely thermal excitation of the gas, in the regime where [OI] and [OIII] are approximately equal (for  $4.0 \lesssim \log T \lesssim 4.3$ ), there should be no HeI detectable at all, since the temperature of the gas is far too low to excite the HeI line. On the other hand, the top panels show the possibility of HeI emission when [OI] and [OIII] are comparable, and moreover that the HeI should have lower emissivity than the [OI] and [OIII] lines. Furthermore, the H $\alpha$  should be one to two orders of magnitude greater than [OI] and [OIII] when the latter two are equal. This situation describes quite well what I have found in NGC 5044. However, in this plot the [OI] and [OIII] emissivities become comparable in the thermally unstable region (indicated by the gray bar at the top of each figure). This shows the need to run the CLOUDY model with conditions in the gas more appropriate to NGC 5044 (recall that these plots are applicable to the conditions

in NGC 1275, the central galaxy of the much richer Perseus cluster), and the potential that such modeling has to constrain the temperature/density of the gas.



## Chapter 4

# Sites of Star Formation in the Central Galaxy of the Perseus Cluster



empty

The most famous example of a cool-core BCG hosting a filamentary emission nebula is NGC 1275, the central elliptical galaxy of the Perseus cluster, the X-ray-brightest cluster in the sky. Perseus is the archetypal cool-core cluster, and both the X-ray gas permeating the cluster core as well as the filamentary nebula in NGC 1275 have been extensively studied. NGC 1275 has also long been known to harbor star formation (see, e.g., Richer et al. (1993)). Recently, catalog of the compact star clusters in NGC 1275 has been produced by Lim et al. (2020). Figure 4.1 shows a map of the population of young clusters from this catalog overlaid on H $\alpha$ +[NII] image of NGC 1275 taken with HST/ACS. This figure shows that the spatial distribution of star clusters is, in places, similar to the H $\alpha$  filaments, yet are not exactly aligned with them; a fact that has been reported previously by Canning et al. (2010). This oftentimes close spatial relationship indicates that star formation within the cool gas filaments. Isolated regions with [OIII] emission have been identified in NGC 1275 before: Shields & Filippenko (1990) identify a giant HII region at the inner end of a nebular filament bright in [OIII], and Hatch et al. (2006) identify three regions bright in [OIII]. Until now, however, the nebula has never been imaged in [OIII] in its entirety.

In this Chapter, I present narrowband imaging of the [OIII] $\lambda 5007$  line from NGC 1275. Our first objective is to search for sites of star formation within the filaments of NGC 1275 as evidenced by giant HII regions (identified as regions bright in both H $\alpha$  and [OIII], and having a [OIII]/H $\alpha$  line ratio characteristic of HII regions). Although we know of at least one giant HII region at the end of a filament in the inner part of the nebula (that identified by Shields & Filippenko (1990)), most of the young star clusters lie in the outer regions



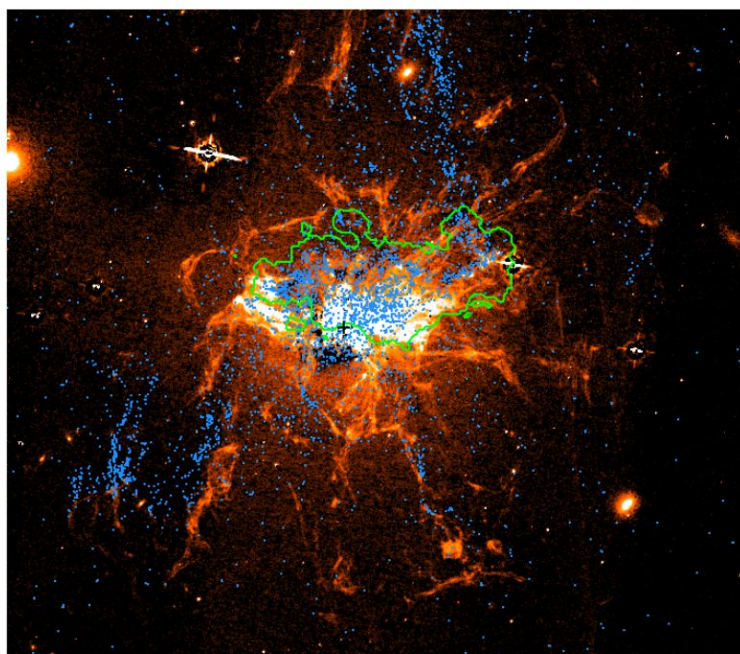


Figure 4.1 Map of the young star clusters cataloged by Lim et al. (2020) overlaid on a H $\alpha$ +[NII] image of NGC 1275. The green contour highlights the extent of the HVS.

of the nebula, raising the question of exactly where star formation is occurring throughout the nebula. Our second objective is to search for [OIII] emission from the young star clusters themselves, helping us to understand how long the clusters are able to hold on to the gas from which they initially formed before it is ejected by radiation pressure and shocks. Indeed, theoretical models suggest that the natal gas for star formation should be quickly cleared, thus providing a feedback mechanism for limiting their total stellar masses (Howard et al. 2018). Our results also unexpectedly revealed weak [OIII] counterparts to some of the H $\alpha$  filaments, even in regions where young star clusters are entirely absent. A third objective, therefore, is to measure the [OIII]/H $\alpha$  ratio in the filaments.

The northern region of NGC 1275 is partially obscured by an in-falling spiral galaxy known as the High Velocity System (HVS), shown in the green contour

in Figure 4.1<sup>1</sup>. The HVS hosts numerous HII regions that are bright in both H $\alpha$  and [OIII], which means that care is needed to exclude the HVS when searching for HII regions from NGC 1275. Nevertheless, the HVS is an interesting object of study in and of itself, as it presents an opportunity to study how ram pressure stripping (known to be taking place in the HVS due to the in-fall of the galaxy through the ICM; see Yu et al. 2015) affects star formation.

In the following study, I assume a distance to NGC 1275 of 74Mpc, so that  $1'' = 360\text{pc}$  and  $cz = 5264\text{km s}^{-1}$ . On the other hand, the HVS has  $cz \approx 8200\text{km s}^{-1}$

## 4.1 Observations and Data Reduction

We obtained narrow-band imaging of the [OIII] $\lambda 5007$  line from NGC 1275 using the 3.6 m Canada-France-Hawaii Telescope (CFHT) with the MegaPrime wide-field camera on 2018-03-19 and 2019-05-02. The total integration time was 1.88h across 8 exposures. At the redshift of NGC 1275, the [OIII] $\lambda 4959$  line is still in MegaCam’s [OIII]-on filter, while the [OIII] $\lambda 5007$  line is shifted into the adjacent [OIII]-off filter (see Figure 4.2). We therefore used the [OIII]-off filter to image the [OIII] $\lambda 5007$  line from NGC 1275 (hereafter [OIII] unless otherwise specified). Unfortunately, this filter also covers the [OIII] $\lambda 5007$  and [OIII] $\lambda 4959$  lines from the HVS; however, as mentioned above the HVS only covers a limited region of the nebula.

In order to image the line emission from the nebula, the underlying stellar continuum must be subtracted from the narrowband image. As can be seen in

---

<sup>1</sup>The green contour H $\alpha$  contour from the HVS is based on IFU observations with the Potsdam Multi-Aperture Spectrophotometer (PMAS). See Yu et al. (2015) for more details about the PMAS observations.



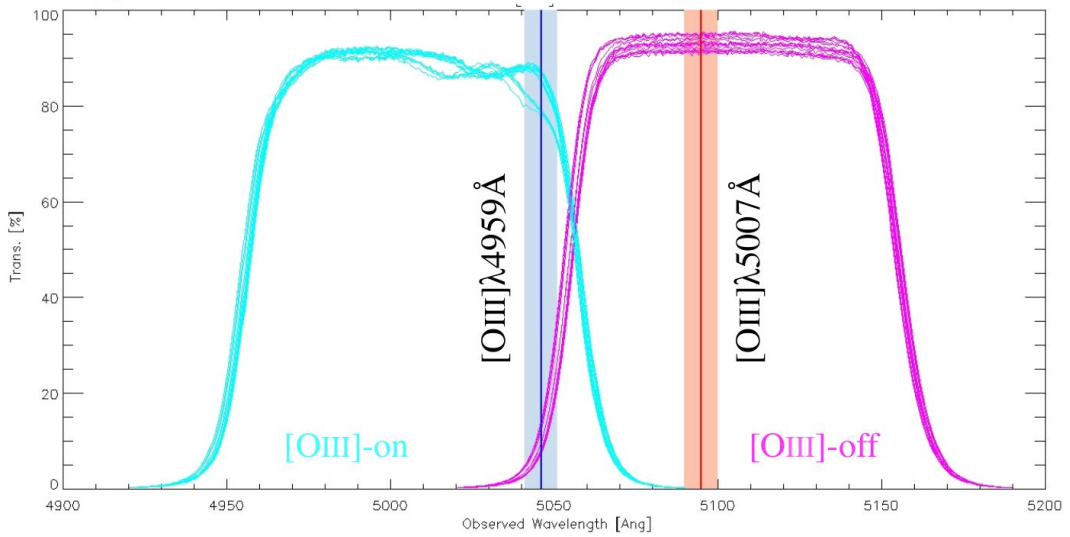


Figure 4.2 MegaPrime [OIII]-on and [OIII]-off filters showing the wavelengths of the redshifted [OIII] $\lambda$ 4959 and  $\lambda$ 5007 lines from NGC 1275.

Figure 4.2, the [OIII]-on filter adjacent to the [OIII]-off cannot be used as it covers the [OIII] $\lambda$ 4959 line from NGC 1275. In the original proposal, we proposed using archival HST data for subtracting the stellar continuum, specifically the F550M filter image from the Advanced Camera for Surveys (ACS) from the Hubble Legacy Archive (HLA) DR10. We chose this filter because of its lack of any prominent spectral lines from the nebula as well as its proximity to the [OIII] line, as shown in Figure 4.3.

We targeted a sensitivity of  $\sim 4 \times 10^{-20}$  erg s $^{-1}$  cm $^{-2}$  Å $^{-1}$  across the bandpass of the [OIII]-off filter. Using the MegaCam Direct Imaging Exposure Time Calculator (*Diet*), we computed an exposure time of 70 minutes to obtain adequate signal-to-noise (in the end we were given 113 minutes). We targeted this sensitivity in order to be able to detect [OIII] emission from massive young star clusters as reported in Lim et al. (2020). They estimated a maximal H $\alpha$  flux density from the young star clusters and, assuming an H $\alpha$ /[OIII] ratio of

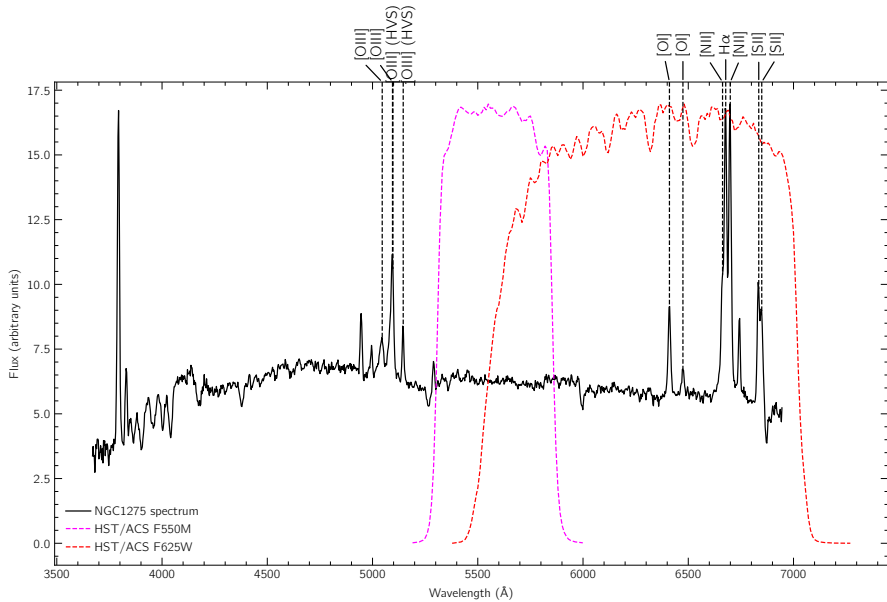


Figure 4.3 HST/ACS F550M filter bandpass in pink overlaid on an example spectrum from NGC 1275. The filter bandpass in red is the F625W R band filter used to image the H $\alpha$ +[NII]+[SII]+[OI] lines.

$\sim 6$ , a corresponding [OIII] flux density averaged over the [OIII]-off bandpass of  $\sim 2 \times 10^{-19}$  erg s $^{-1}$  cm $^{-2}$  Å $^{-1}$ . The targeted sensitivity is a factor of 5 to include young star clusters having lower H $\alpha$  flux densities as well as to account for possible dust extinction in the youngest star-forming regions.

I used AstrOmatic software packages to perform the initial stacking of the 8 frames obtained with the CFHT. I first generated masks of the bad pixels in each frame using generic MegaPrime bad pixel files in conjunction with WEIGHT-WATCHER (Marmo & Bertin (2008)). Next, I performed source extraction and cataloging using SExtractor. I then used these catalogs to compute astrometric and photometric distortion corrections using SCAMP. Finally, I applied the derived corrections, resampled each frame to a common grid, and stacked the images using SWARP. The final angular resolution (FWHM) of the stacked image is 0.90''.

With the [OIII]-off narrowband image in hand, I am ready to subtract the stellar continuum using the V band (F550M) image of NGC 1275 from the HST. Before the subtraction can be made, I first have to match the spatial resolutions of the HST (continuum) and CFHT (narrowband) images. This involved using SExtractor to detect sources and generate a catalog including vignetted images of each source. I then filtered the resulting catalog to include only relatively bright, unsaturated point sources from each image, and stacked the vignettes in each filtered catalog to obtain a PSF for each image. I then cross-convolved the images to bring them to a common spatial resolution (cross-convolution produces a better match between the images compared to convolving the HST image alone; furthermore convolving the narrowband image with the HST PSF does not significantly affect its angular resolution). Having matched the spatial resolutions of the narrowband and continuum images, I then ran SExtractor again to detect sources in each image and generate catalogs that were then used by SCAMP to derive alignment and distortion corrections. The corrections were then applied by SWARP, which also resampled the images onto a common grid so that they could be subtracted.

I subtracted the continuum image from the OIII narrowband image to reveal the [OIII] emission from the nebula. I found the appropriate scaling factor by which the HST continuum image had to be multiplied before subtraction from the [OIII] narrowband image by first finding the maximum counts at the center of NGC 1275 in each image, then setting the scaling factor to be equal to the quotient of the narrowband maximum over the continuum maximum. Then I performed a manual fine adjustment of the scaling factor to ensure that the background was as flat as possible (i.e. free of any residual continuum) by summing the residual image along the vertical and horizontal axes and inspecting



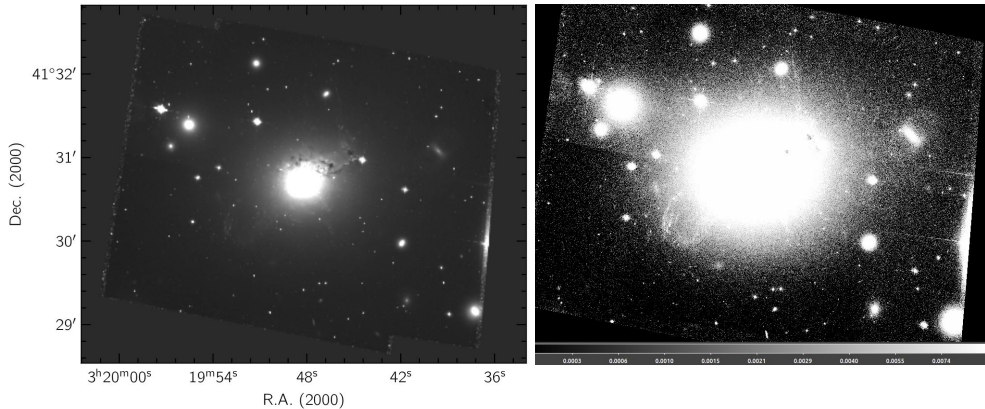


Figure 4.4 Left: HST/ACS F550M continuum image. Right: the same image with exaggerated scaling revealing the background structure which became imprinted onto the continuum-subtracted [OIII] image.

the resulting 1D profiles.

Unfortunately, the first continuum-subtracted image that I made via the procedure outlined above had a highly uneven background level. I therefore checked the background level in the continuum and narrowband images to see which image was causing the problem, and found that the HST/ACS F550M image I used for the continuum showed a highly non-uniform background as can be seen in the right panel of Figure 4.4. Since much of the structure seen in [OIII] is at a relatively low signal-to-noise, even small offsets in the background may obscure features. The HST continuum image I had been using up to this point was generated automatically by HLA (including a background subtraction step). Therefore, I obtained the raw HST F550M frames of NGC 1275 from Mikulski Archive for Space Telescopes (MAST), and performed my own background subtraction and stacking. Rather than using the usual HST data reduction facilities (i.e. DRIZZLEPAC), which are designed to maximize the spatial resolution of the resulting image, I used the AstrOmatic packages SExtractor, SCAMP, and SWARP as used before to align, perform background

subtraction, and stack the frames. The resulting stacked image showed some improvement in the background, yet substantial issues still clearly remain (see 4.2).

I configured SCAMP to provide an automatic photometric calibration during the initial stacking procedure of the [OIII]-off frames by scaling each frame to correct for varying atmospheric extinction and bring them all to a common instrumental zeropoint AB magnitude of 30.0. This then allowed me to convert the [OIII]-off stacked image into units of  $\text{erg s}^{-1} \text{cm}^{-2} \text{\AA}^{-1}$ . I performed a simple check on the photometry by comparing some of the bright stars in the field against calibrated HST B and V band images from HLA, finding the flux densities to be consistent.

An image of the  $\text{H}\alpha$  filaments in NGC 1275 is also needed for comparison with my [OIII] map and to derive [OIII]/ $\text{H}\alpha$  ratios. I obtained a map that was generated using HST/ACS data by subtracting the F550M (V band) filter from the F625W (R band) filter, which covers the  $\text{H}\alpha + [\text{NII}]$  lines from NGC 1275 and the HVS as well as the  $[\text{SII}]\lambda 6717/6731$  and the  $[\text{OI}]\lambda 6300/6363$  doublets from NGC 1275 as shown in Figure 4.3. We initially decided to use this image due to the depth and high angular resolution of HST/ACS data. However, the inclusion of these other emission lines makes it difficult to infer precise [OIII]/ $\text{H}\alpha$  ratios since the relative strength of the  $\text{H}\alpha$  line compared with the others ([NII], [OI], and [SII]) varies considerably throughout the nebula. For instance, Hatch et al. (2006) report typical line intensity ratios of 0.3 - 1.5 for  $[\text{NII}]\lambda 6584/\text{H}\alpha$ , 0.14 - 0.54 for  $[\text{SII}]\lambda$ , and 0.1 - 0.3 for  $[\text{OI}]\lambda 6300/\text{H}\alpha$ . In future work on this project, my intention is to replace the  $\text{H}\alpha$  map in this thesis with a true narrowband image covering only the  $\text{H}\alpha + [\text{NII}]$  lines from NGC 1275, such as that used in Conselice et al. (2001). For the purposes of this MPhil Thesis, however, this



HST/ACS image is sufficient for an initial investigation of my stated scientific objectives. For sake of clarity, I refer to this map as the H $\alpha$ + map hereafter. I matched the spatial resolution of the H $\alpha$ + map to that of the [OIII] map by convolving the former image with the same CFHT PSF I used to convolve the F550M continuum image. I then resampled the H $\alpha$ + image to match the courser grid of the [OIII] image.

## 4.2 Results and Discussion

The full stacked MegaPrime [OIII]-off narrowband image is shown in Figure 4.5, with a zoom in on the cluster core including NGC 1275 shown next to it. Simple visual inspection reveals filamentary structures, even before subtraction of the stellar continuum. Whereas some of these filamentary structures are produced by discrete sources corresponding to relatively young star clusters arranged in filament-like structures (constituting their relatively blue continuum along with any [OIII] emission), others genuinely comprise diffuse [OIII] emission from the nebular filaments. The latter result is a new discovery, demonstrating that, rather than just a few isolated giant HII regions, the entire nebula also glows in [OIII].

The continuum-subtracted [OIII] image is shown in the upper right panel of Figure 4.6 next to the HST H $\alpha$ + map (upper left), and an overlay of the young star clusters cataloged by Lim et al. (2020) (lower left). The [OIII] image shows some features that coincide with the H $\alpha$ + filaments and others that coincide with the dense, filament-like distribution of young star clusters (and some that coincide with both H $\alpha$ + emission and star clusters). We urge caution in interpreting all the features seen in the continuum-subtracted [OIII] image as



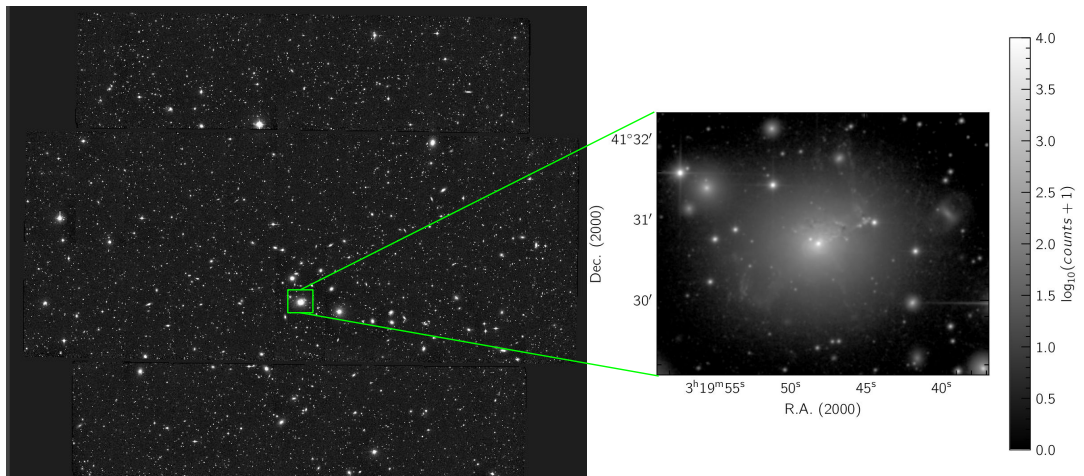


Figure 4.5 Entire field imaged by MegaPrime in the [OIII]-off filter showing many members of the Perseus cluster, with zoom-in on NGC 1275 at the core of the Perseus cluster showing gaseous filaments and/or young star clusters (log scaling).

genuine [OIII] emission, as only the old stellar population comprising the main body of NGC 1275 has been subtracted. Because the young star clusters are bluer compared with the underlying old stellar population, emission associated with the young stellar population in the continuum-subtracted [OIII] image could correspond to their only partially-subtracted continuum emission along with any genuine [OIII] emission.

As can clearly be seen in Figure 4.6, the backgrounds of the continuum-subtracted [OIII] and H $\alpha$ + images are highly non-uniform due to issues with the stacking of the HST/ACS V band images as described in Section 4.1. This issue will require further work to resolve, either by improving the background subtraction of the HST/ACS images, or by finding different data sets entirely for the continuum subtraction. For now, to better demonstrate the scientific potential of the [OIII] image obtained with the CFHT, I mitigate the effect of background variation by selecting a few regions in the [OIII] image where the background is reasonably flat and make cutouts. These regions are shown as

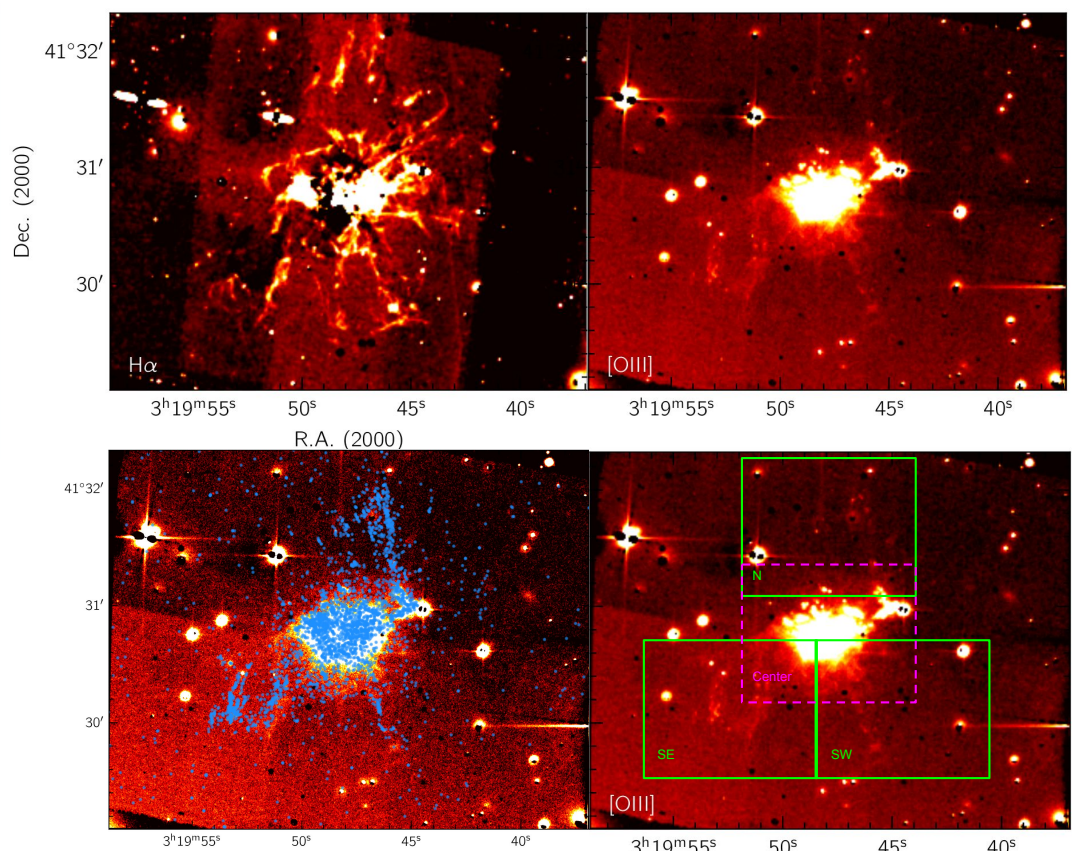


Figure 4.6 HST H $\alpha$ + image (upper left), CFHT [OIII] image (upper right), overlay of young clusters from Lim et al. (2020) (lower left), and cutout regions used to mitigate the uneven background (lower right).

green rectangles labeled SE, SW, and N in the lower right panel of Figure 4.6. In addition, I made a cutout of the central region, shown as a dashed magenta rectangle labeled “center” in the lower right panel of Figure 4.6 to investigate two previously identified giant HII regions in this area (owing to the bluer color of the stellar continuum in the inner region of NGC 1275 compared to the outer regions, I used slightly different scaling factors when subtracting the continuum from the  $\text{H}\alpha+$  and [OIII] images in this cutout). I then performed separate background subtractions using the median value of a patch of blank sky in each cutout.

At this stage, it is important to mention that young star clusters (whether they contain HII regions or not) are bluer than the background old stellar population of NGC 1275, so their continuum cannot be properly subtracted in either the [OIII] or  $\text{H}\alpha+$  images. This raises a problem: how do we identify genuine HII regions when we cannot be sure of their true [OIII] (and  $\text{H}\alpha+$ ) brightness? I get around this problem by using the HII region identified by Shields & Filippenko (1990) (which has been spectroscopically confirmed to be bright in [OIII]) to set a fiducial [OIII]/ $\text{H}\alpha+$  ratio that can be used to identify other giant HII regions.

Figure 4.7 shows the central cutout in  $\text{H}\alpha+$  and [OIII]. This region is of interest because it contains one giant HII region (labeled HIIa) first studied by Shields & Filippenko (1990), as well as another candidate giant HII region (labeled HIIb) identified by Lim et al. (2012). In the lower left of Figure 4.7 is a map of the  $2.12\mu\text{m}$   $\text{H}_2$  to  $\text{H}\alpha+[\text{NII}]$  ratio in the central region (reproduced from Lim et al. (2012)), in which both HIIa and HIIb can clearly be made out in blue. In the lower right of the figure, I include an overlay of the youngest star clusters from Lim et al. (2020), with ages  $\lesssim 100\text{Myr}$  as determined by



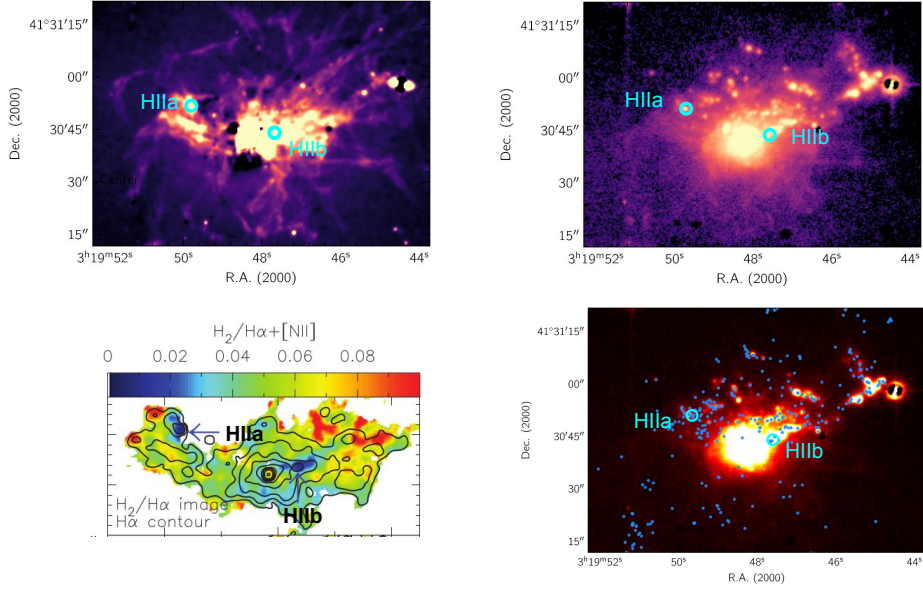


Figure 4.7 Cutout of the central region of NGC 1275 in H $\alpha$ + (upper left) and [OIII] (upper right). Shown below is the H<sub>2</sub>/H $\alpha$  ratio from Lim et al. (2012), indicating the HII region first described in Shields & Filippenko (1990) as well as another candidate HII region to the west of the AGN. The regions are labeled HIIa and HIIb on the [OIII] map.

restricting  $B - V < 0$  and  $V - R > 0$ . This shows that HIIa and HIIb are both coincident with young star clusters.

I extracted the total flux from HIIa and HIIb in H $\alpha$ + and [OIII] within a circular aperture of diameter  $1'' \approx \text{FWHM}$ . I found the [OIII]/H $\alpha$ + ratios to be 0.035 for HIIa and 0.043 for HIIb, i.e. roughly consistent with each other. Spectroscopy of HIIa reported in Shields & Filippenko (1990) shows the ratio of [OIII] to H $\alpha$ +[NII]+[SII]+[OI] to be close to this value, at  $\sim 0.037$ , and the HII regions identified by Hatch et al. (2006) also have [OIII]/H $\alpha$ + ratios at or above this value. This [OIII]/H $\alpha$ + ratio of  $\sim 0.04$  provides a simple criterion by which to search for candidate giant HII regions throughout the filaments.

Figure 4.8 shows the south-eastern cutout, labeled SE in Figure 4.6, in H $\alpha$ + (upper left panel) and [OIII] (upper right panel). Indicated in the Figure is

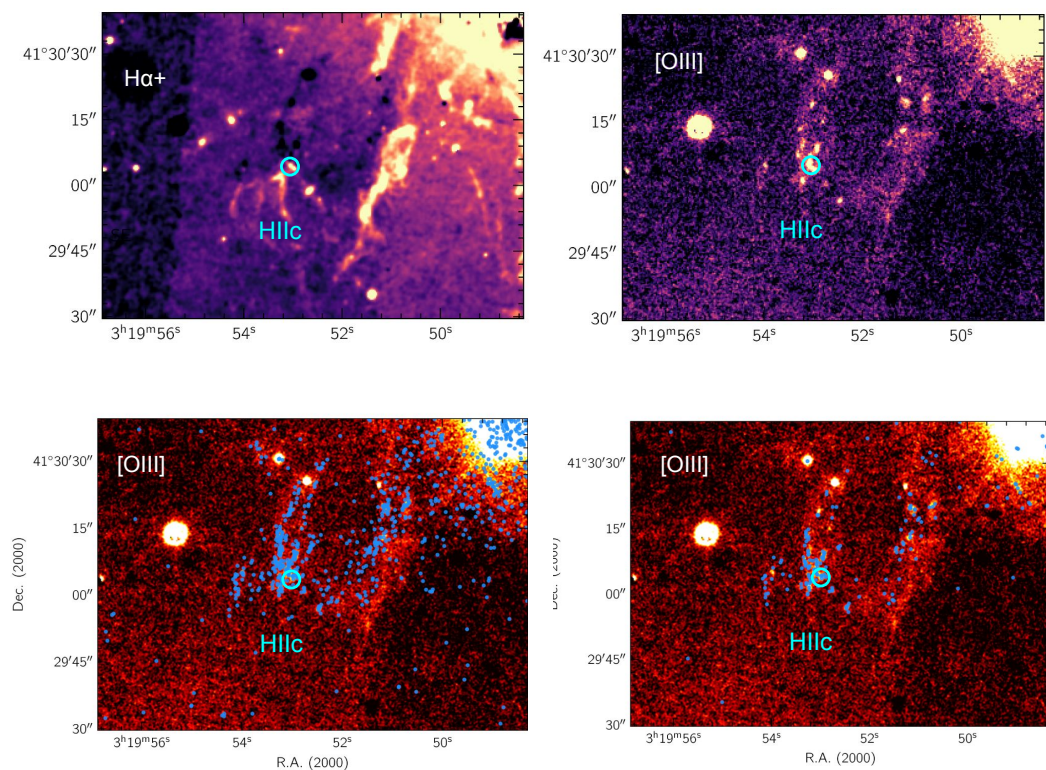


Figure 4.8 Cutout of the south-eastern region of NGC 1275 in H $\alpha$ + (upper left) and [OIII] (upper right). Shown below are overlays of the young star clusters cataloged by Lim et al. (2020), with only the youngest clusters (of ages  $\lesssim 100$  Myr) being shown in the lower right panel.



an example of a candidate giant HII region, labeled HIIc. The [OIII]/H $\alpha$ + ratio here to be 0.045, in line with the other giant HII regions described above and shown in Figure 4.7. The lower left panel shows an overlay of the blue star clusters cataloged by Lim et al. (2020) on the [OIII] map, while the lower right panel shows only the youngest clusters with ages  $\lesssim 100$  Myr. These panels show that, like HIIa and HIIb, HIIc is cospatial with a number of young blue clusters. Follow-up spectroscopy of HIIc – along with any other candidate HII regions found based on the [OIII]/H $\alpha$ + ratio – will firstly allow us to accurately determine the [OIII]/H $\alpha$  ratio and thus confirm if they are genuine HII regions, and secondly help determine whether these HII regions are truly part of the filaments (by looking at the kinematics).

Another notable feature of Figure 4.8 is the so-called “blue loop”, which is clearly visible in [OIII], but shows up as an over-subtracted region in the H $\alpha$ + image. This is due to the bluer color of the loop compared to the isotropically-distributed old stellar population, which means that when the V band continuum is subtracted from the H $\alpha$ + and [OIII] images, the blue loop becomes over-subtracted in the H $\alpha$ + image and under-subtracted in the [OIII] image. The overlay of the young star clusters in the bottom right panel shows that the brightest [OIII] knots in the blue loop are cospatial with the youngest star clusters. This suggests that the young star clusters do not immediately eject the gas from which they form, and though more detailed analysis may enable us to put upper limits on the age of the clusters still emitting [OIII].

Figure 4.9 shows the cutout of the northern filaments (labeled ‘N’ in Figure 4.6). The H $\alpha$ + image (upper left) clearly shows three bright filaments, which can also be faintly made out in the [OIII] panel in the upper right. A comparison with the distribution of young star clusters (lower left) reveals that, while the



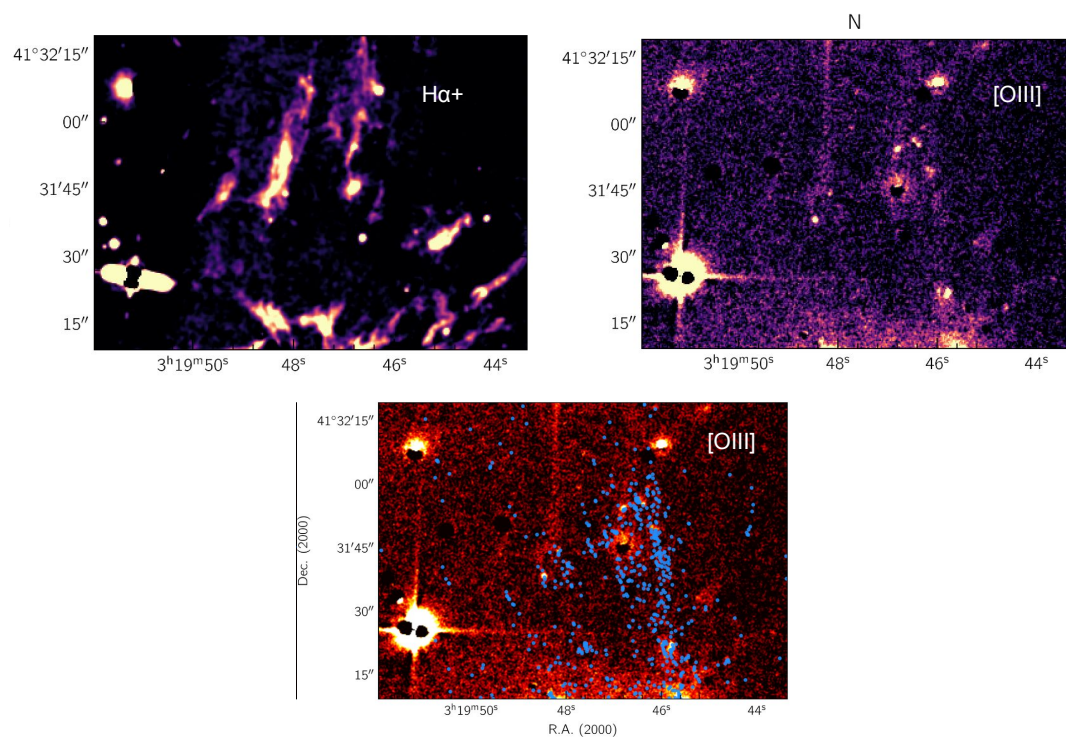


Figure 4.9 Cutout of the northern region of NGC 1275 in H $\alpha$ + (upper left) and [OIII] (upper right). Shown below is an overlay of the young star clusters cataloged by Lim et al. (2020).

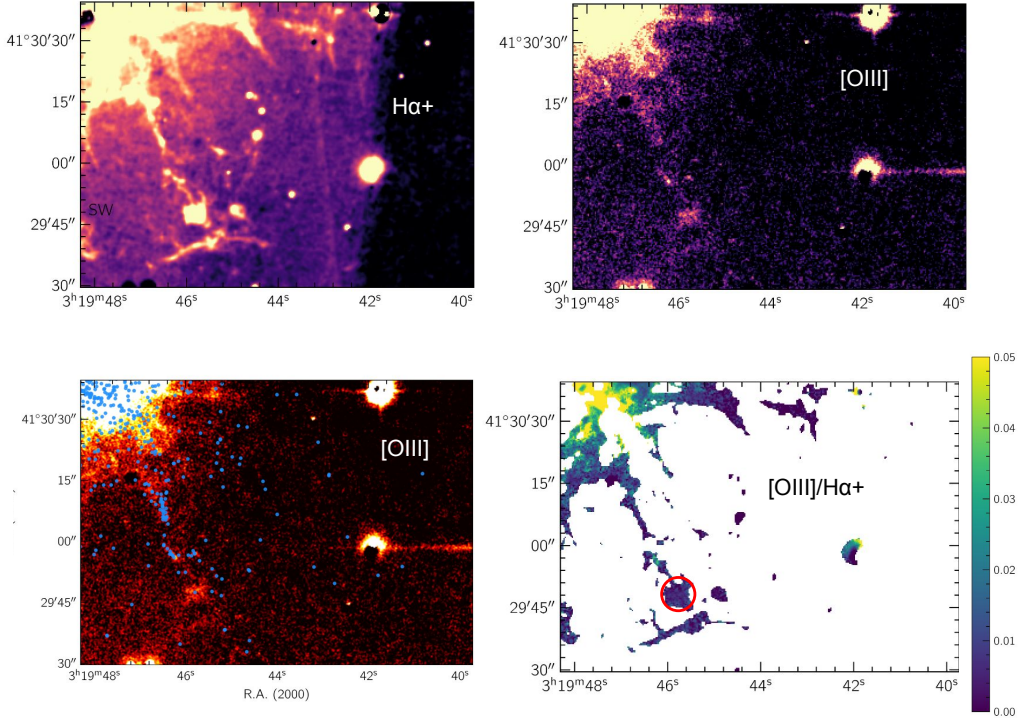


Figure 4.10 Cutout of the south-western region of NGC 1275 in H $\alpha$ + (upper left) and [OIII] (upper right). Shown in the lower left is an overlay of the young star clusters cataloged by Lim et al. (2020) and in the lower right is the [OIII]/H $\alpha$ + ratio, showing the circular aperture from which the [OIII]/H $\alpha$ + ratio was extracted.

westernmost of these three filaments coincides with a region rich in clusters, the other two filaments are almost entirely free of them. Moreover, I find the [OIII]/H $\alpha$ + ratio in this filament to be  $< 10^{-3}$ , far below the  $\sim 0.04$  found in the giant HII regions. This constitutes strong evidence for the emission of (weak) [OIII] from the filaments themselves, as well as from young star clusters and giant HII regions.

Perhaps the best example of a nebular filament emitting [OIII] but devoid of young star clusters is seen in H $\alpha$ + and [OIII] in Figure 4.10. The lower right panel of the figure shows the [OIII]/H $\alpha$ + ratio over the H $\alpha$ + filaments (pixels

below 3 sigma in H $\alpha$ + have been left blank). Taking the average [OIII]/H $\alpha$ + ratio in the circular aperture shown in red in the lower right panel of the figure gives a value of  $\sim 0.006$ . The presence of [OIII] emission from the filaments of NGC 1275 echoes the results found in NGC 5044 reported in 3.2. However, there is a significant disparity in the [OIII]/H $\alpha$  ratio between the two galaxies: in NGC 5044 the ratio was found to be  $\sim 0.1$ , roughly an order of magnitude greater than that in NGC 1275 (after correcting for the additional lines in the H $\alpha$ + image). It remains to be determined whether the ratio in this filament is representative of the rest of the nebula; however, since this filament appears to be among the brightest in [OIII], it suggests that the [OIII]/H $\alpha$  ratio in NGC 1275 is significantly lower than in NGC 5044.



# Chapter 5

## Summary and Conclusions



empty

In this MPhil thesis, I have presented observations/archival data of two cool-core central elliptical galaxies hosting filamentary emission nebulae: NGC 5044 and NGC 1275.

In the first part of this thesis (chapter 2), I present an analysis of spectroscopic data covering the H $\alpha$ , 2.12 $\mu$ m H<sub>2</sub>, and 1.3mm lines from NGC 5044. This project has already been written up as a draft paper (in Section 2.4). The results lead me to the following conclusions regarding the multi-phase gas in the filaments of NGC 5044:

- All three lines share strikingly similar spectral profiles, suggesting extremely strong kinematic coupling between the H $\alpha$ -, H<sub>2</sub>-, and CO-emitting phases.
- If the H $\alpha$ , H<sub>2</sub>, and CO lines are emitted by distinct clouds of hot ionized, warm, and cold gas, respectively, then ram pressure from the surrounding ICM should cause them to rapidly decouple.
- Such kinematic close coupling is consistent with emission from common volumes of gas. This supports the excitation mechanism of the gas in the filaments proposed by Ferland et al. (2009) in which high energy particles penetrate into the nebula, since this mechanisms permits molecular, atomic and ionized phases to exist simultaneously (unlike processes that deposit purely thermal energy into the gas). This represents the first time that this model of excitation has been tested in any cool-core nebula other than NGC 1275.
- The H<sub>2</sub>/H $\alpha$  ratio in the filaments of NGC 5044 is  $\sim 0.1$ , and this value is approximately constant throughout the nebula – including the outermost



filaments – though it falls slightly with radius in the inner region.

- This puts the  $H_2/H\alpha$  ratio in NGC 5044 surprisingly close to that in NGC 1275 ( $\sim 0.1$ ). This is surprising given that the pressure in NGC 1275 is  $\sim 5$  times higher than in NGC 5044, and the flux of energetic particles penetrating into the nebula is also  $\sim 5$  times greater. Further insight into this issue requires theoretical modeling of the gas in NGC 5044.

In the second part of this thesis (chapter 3), I extract optical line emission strengths from the filamentary nebula in NGC 5044 using IFU data from MUSE. The data reduction of this project is essentially complete, and further work (hopefully with collaborators) will focus on interpreting the results. The key takeaways at this stage are:

- There is significant [OIII] and [OI] emission throughout the filaments of NGC 5044.
- The [OIII]/ $H\alpha$  and [OI]/ $H\alpha$  ratios are both  $\sim 0.1$ . The [OI]/ $H\alpha$  ratio is constant throughout the filaments, while the [OIII]/ $H\alpha$  ratio seems to drop abruptly moving away from the central region.
- The [OI]/ $H\alpha$ , [OIII]/ $H\alpha$ , and [OI]/[OIII] ratios can act as powerful constraints on the excitation mechanism, and also help to constrain the thermal state of the gas.
- The only thing remaining in this project is to perform theoretical calculations of [OIII], [OI], and  $H\alpha$  emission from the gas in the filaments of NGC 5044 (similarly to what has already been done for NGC 1275). This will allow us to compare our findings with theoretical predictions of the energetic particle and pure heating excitation models.



In the final part of this thesis (chapter 4), I present imaging of the [OIII] line from NGC 1275. Although this study is still in relatively early stages, with improvements to the data reduction and analysis to follow, the work I have completed so far shows promising results:

- For the first time, diffuse [OIII] emission extending throughout the filaments of NGC 1275 has been detected. The [OIII]/H $\alpha$  line ratio is of the order of  $\sim 0.01$ , an order of magnitude below that found in NGC 5044 in Chapter 3.
- The [OIII] map shows a number of regions with elevated [OIII]/H $\alpha$  ratios comprising giant HII regions within the filaments. Identifying these regions and following up with spectroscopy will allow us to (i) determine whether these are genuine giant HII regions in the filaments and (ii) investigate the conditions necessary for initiating star formation in the filaments.
- There is [OIII] emission from the youngest star clusters in NGC 1275. Moving forward, we hope to identify an upper limit on the age of [OIII]-emitting clusters to gain insights into their evolution.



# Bibliography

Astropy Collaboration, Robitaille, T. P., Tollerud, E. J., et al. 2013, A&A, 558, A33

Astropy Collaboration, Price-Whelan, A. M., Sipőcz, B. M., et al. 2018, AJ, 156, 123

Bertin, E. 2006, in Astronomical Society of the Pacific Conference Series, Vol. 351, Astronomical Data Analysis Software and Systems XV, ed. C. Gabriel, C. Arviset, D. Ponz, & S. Enrique, 112

Bertin, E., & Arnouts, S. 1996, A&AS, 117, 393

Bertin, E., Mellier, Y., Radovich, M., et al. 2002, in Astronomical Society of the Pacific Conference Series, Vol. 281, Astronomical Data Analysis Software and Systems XI, ed. D. A. Bohlender, D. Durand, & T. H. Handley, 228

Canning, R. E. A., Fabian, A. C., Johnstone, R. M., et al. 2010, MNRAS, 405, 115

Cavagnolo, K. W., Donahue, M., Voit, G. M., & Sun, M. 2008, The Astrophysical Journal, 683, L107

Churazov, E., Forman, W., Jones, C., & Bohringer, H. 2003, The Astrophysical Journal, 590, 225237



- Collins, K. A., Kielkopf, J. F., Stassun, K. G., & Hessman, F. V. 2017, The Astronomical Journal, 153, 77
- Conselice, C. J., Gallagher, John S., I., & Wyse, R. F. G. 2001, AJ, 122, 2281
- Cowie, L. L., & Binney, J. 1977, ApJ, 215, 723
- David, L. P., Jones, C., Forman, W., et al. 2009, ApJ, 705, 624
- David, L. P., Nulsen, P. E. J., McNamara, B. R., et al. 2001, The Astrophysical Journal, 557, 546
- David, L. P., Vrtilek, J., OSullivan, E., et al. 2017, The Astrophysical Journal, 842, 84
- David, L. P., OSullivan, E., Jones, C., et al. 2011, The Astrophysical Journal, 728, 162
- David, L. P., Lim, J., Forman, W., et al. 2014, The Astrophysical Journal, 792, 94
- Edge, A. 2001, Monthly Notices of the Royal Astronomical Society, 328, 762
- Fabian, A. 2012, Annual Review of Astronomy and Astrophysics, 50, 455489
- Fabian, A. C., & Nulsen, P. E. J. 1977, MNRAS, 180, 479
- Fabian, A. C., Sanders, J. S., Williams, R. J. R., et al. 2011, Monthly Notices of the Royal Astronomical Society, 417, 172177
- Fabian, A. C., Walker, S. A., Russell, H. R., et al. 2016, Monthly Notices of the Royal Astronomical Society, 461, 922928
- Fazio, G. G., Hora, J. L., Allen, L. E., et al. 2004, ApJS, 154, 10



- Ferland, G. J., Fabian, A. C., Hatch, N. A., et al. 2008, MNRAS, 386, L72
- Ferland, G. J., Fabian, A. C., Hatch, N. A., et al. 2009, Monthly Notices of the Royal Astronomical Society, 392, 1475
- Ferland, G. J., Chatzikos, M., Guzmán, F., et al. 2017, RMxAA, 53, 385
- Hatch, N. A., Crawford, C. S., Johnstone, R. M., & Fabian, A. C. 2006, Monthly Notices of the Royal Astronomical Society, 367, 433448
- Hernquist, L. 1990, ApJ, 356, 359
- Howard, C. S., Pudritz, R. E., & Harris, W. E. 2018, Nature Astronomy, 2, 725730
- Lim, J., Dinh-V-Trung, Vrtilek, J., David, L. P., & Forman, W. 2017, The Astrophysical Journal, 850, 31
- Lim, J., Ohyama, Y., Yan, C.-H., Dinh-V-Trung, & Wang, S.-Y. 2012, ApJ, 744, 112
- Lim, J., Wong, E., Ohyama, Y., Broadhurst, T., & Medezinski, E. 2020, Nature Astronomy, 4, 153
- Lynds, R. 1970, ApJL, 159, L151
- Mannucci, F., Basile, F., Poggianti, B. M., et al. 2001, Monthly Notices of the Royal Astronomical Society, 326, 745
- Marmo, C., & Bertin, E. 2008, in Astronomical Society of the Pacific Conference Series, Vol. 394, Astronomical Data Analysis Software and Systems XVII, ed. R. W. Argyle, P. S. Bunclark, & J. R. Lewis, 619



- Mathews, W. G., Faltenbacher, A., Brighenti, F., & Buote, D. A. 2005, ApJL, 634, L137
- Molendi, S., & Pizzolato, F. 2001, The Astrophysical Journal, 560, 194
- Moorwood, A., Cuby, J. G., Biereichel, P., et al. 1998, The Messenger, 94, 7
- Olivares, V., Salome, P., Combes, F., et al. 2019, Astronomy Astrophysics, 631, A22
- Ott, T. 2012, QFitsView: FITS file viewer, ascl:1210.019
- Peterson, J. R., Kahn, S. M., Paerels, F. B. S., et al. 2003, The Astrophysical Journal, 590, 207
- Qiu, Y., Bogdanovi, T., Li, Y., McDonald, M., & McNamara, B. R. 2020, Nature Astronomy, 4, 900906
- Richer, H. B., Crabtree, D. R., Fabian, A. C., & Lin, D. N. C. 1993, AJ, 105, 877
- Salomé, P., & Combes, F. 2003, A&A, 412, 657
- Schellenberger, G., David, L. P., Vrtilek, J., et al. 2020, The Astrophysical Journal, 894, 72
- Shields, J. C., & Filippenko, A. V. 1990, ApJL, 353, L7
- Skrutskie, M. F., Cutri, R. M., Stiening, R., et al. 2006, The Astronomical Journal, 131, 1163
- Temi, P., Brighenti, F., & Mathews, W. G. 2007, The Astrophysical Journal, 666, 222230



- Tonry, J. L., Dressler, A., Blakeslee, J. P., et al. 2001, The Astrophysical Journal, 546, 681
- Virtanen, P., Gommers, R., Oliphant, T. E., et al. 2020, Nature Methods, 17, 261
- Voit, G. M., Cavagnolo, K. W., Donahue, M., et al. 2008, The Astrophysical Journal, 681, L5
- Weilbacher, P. M., Palsa, R., Streicher, O., et al. 2020, Astronomy Astrophysics, 641, A28
- Yu, A. P. Y., Lim, J., Ohyama, Y., Chan, J. C. C., & Broadhurst, T. 2015, ApJ, 814, 101

